UNIVERSITÀ DEGLI STUDI DI ROMA "TOR VERGATA"

FACOLTÀ SCIENZE MATEMATICHE FISICHE E NATURALI

DOTTORATO DI RICERCA IN SCIENZE CHIMICHE - XXII CICLO

Different mechanisms of action of antimicrobial peptides: insights from fluorescence spectroscopy

BARBARA ORIONI

Supervisor: Prof. Lorenzo Stella

Ph. D. School Coordinator: Prof. Bruno Crociani

A. A. 2009/2010

ABSTRACT

Antimicrobial peptides (AMPs) are natural oligopeptides endowed with a strong bactericidal activity. Most of them kill bacteria by interacting with their membranes and perturbing their permeability. Due to this mechanism of action, which apparently does not induce bacterial resistance, they are investigated as promising candidates for the development of new antibiotic drugs to face the insurgence of multidrug resistant bacteria. Several different models have been proposed for their mechanism of membrane perturbation, but the molecular details of this process are still debated. Therefore, structural data on their interaction with lipid bilayers are essential for a detailed understanding of their mechanism of membrane destabilization, and for the rational design of new, potent and selective peptidomimetic analogues.

In this work, fluorescence spectroscopy was employed, together with other physico-chemical techniques, such as neutron reflectivity, Langmuir-Blodgett film balance and molecular dynamics simulations, to characterize the mechanism of action of PMAP-23, chosen as a typical example of cationic, helical AMPs. In order to discuss the different mechanisms of action of AMPs, and to evidence the potential of spectroscopic methods to discriminate between the different models, the results obtained with PMAP-23 were systematically compared with those previously reported for the peptaibol trichogin GA IV.

Both experimental and theoretical data indicate a PMAP-23 location just below the polar headgroups of the membrane, with an orientation essentially parallel to the bilayer plane. These findings, together with experimental results on peptide-induced leakage from large and giant vesicles, lipid flip-flop and peptide exchange between vesicles, support a mechanism of action consistent with the "carpet" model. According to this model, peptide accumulation in the outer leaflet of the bilayer causes a difference in surface tension between the two layers of the membrane, which is then released though the formation of defects, thus inducing membrane leakage. Further experiments excluded the specific role of some PMAP-23 residues in its membrane-perturbing activity .

Finally, a kinetic model describing the kinetics of vesicle leakage induced by antimicrobial peptides was proposed and discussed. The leakage kinetics are usually very slow, requiring minutes to hours for complete release of vesicle contents, and exhibit a biphasic behavior. In this thesis, all the possible options for the rate-limiting step of the slow leakage process were systematically studied. Fluorescence experiments demonstrated that all processes involved in peptide-membrane interaction (peptide-membrane association, peptide aggregation and peptide translocation) take place in a time-scale much shorter than the leakage kinetics. However, peptides are continually exchanging among vesicles, and this necessarily causes fluctuations over time in the number of peptide molecules bound to each liposome, and in the formation of pores. Due to the relatively small size of the vesicles, the number of bound peptides can be rather small, and its fluctuations

significant. Therefore, according to our model, the fast initial leakage is caused by those vesicles which, after the initial random distribution of peptides among liposomes, already contain at least one pore, while the slower release is associated to the time needed to occasionally reach the critical number of bound peptides necessary for pore formation in an intact vesicle. Fluctuations due to peptide exchange among vesicles are therefore the rate-limiting step of such a slow mechanism, that ultimately leads to the leakage of all the loaded vesicles.

Chapter 1

INTRODUCTION

1.1. Bacterial resistance

Antibiotic drugs, discovered during the 20th century, have substantially reduced the problems caused by infectious diseases. The use of these "wonder drugs", combined with improvements in sanitation, housing, and nutrition, and the advent of widespread immunization programs, has led to a dramatic drop in deaths from diseases that were previously widespread, untreatable, and frequently fatal. Over the years, antimicrobials have saved the lives and eased the suffering of millions of people. By helping to bring many serious infectious diseases under control, these drugs have also contributed to the major gains in life expectancy experienced during the latter part of the last century.

These gains are now seriously jeopardized by the emergence and spread of microbes that are resistant to these drugs. Figure 1.1 shows, as an example, the incidence of drug resistant *Staphylococcus aureus* in different countries. The bacterial infections which contribute most to human disease are also those in which emerging and microbial resistance is most evident.

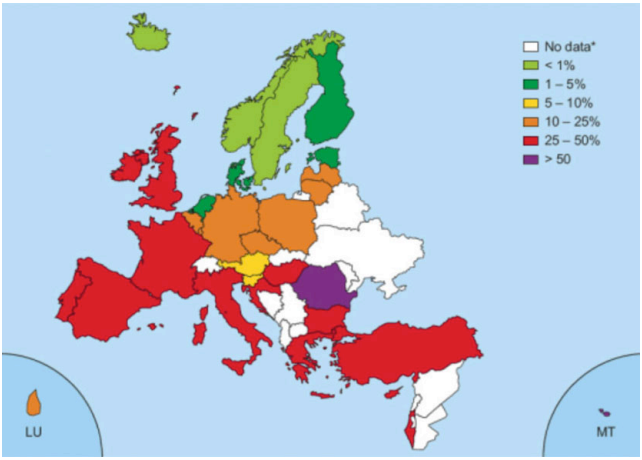

Figure 1.1. Proportion of invasive *S. aureus* isolates resistant to oxacillin (MRSA) in 2006. Countries shown in white didn't report any data or reported less than 10 isolates. [EARSS Annual Report 2006]

The consequences are severe. Infections caused by resistant microbes fail to respond to treatment, resulting in prolonged illness and greater risk of death. Treatment failures also lead to longer periods of infectivity, which increase the numbers of infected people moving in the community and thus expose the general population to the risk of contracting a resistant strain of infection.

Resistance to antimicrobials is a natural biological phenomenon that can be amplified or accelerated by a variety of factors, including human practices. Self-medication, the use of an antimicrobial for any infection, real or feared, in any dose and over any time period, forces microbes to either adapt or die in a phenomenon known as "selective pressure". The microbes which adapt and survive carry genes for resistance, which can be passed on. Antibiotic drugs normally act by penetrating into the microorganisms and by interacting with specific

targets, leading to inhibition to cell wall, DNA or protein biosynthesis in growing cells. Therefore, mechanisms of bacterial resistance include modification of the molecule targeted by the drug, development of alternative metabolic pathways which do not involve the enzyme targeted by the antibiotic, reduction of porin expression or development of active pumps to reduce the intracellular concentration of the drug, and enzymatic degradation of the antibiotic (Figure 1.2).

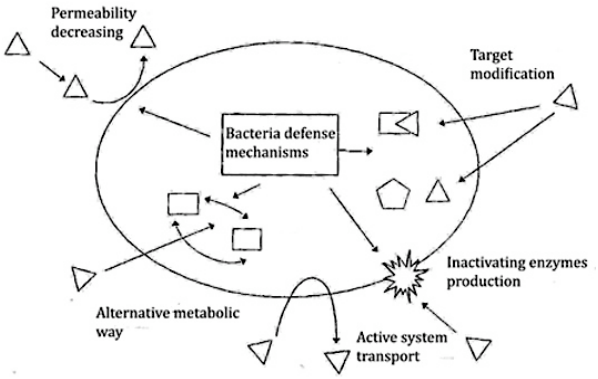

Figure 1.2. Mechanisms of bacterial resistance [http://www.microbiologia.unige.it].

Bacteria are particularly efficient at enhancing the effects of resistance, not only because of their ability to multiply very rapidly but also because they can transfer their resistance genes, which are passed on when the bacteria replicate. When antimicrobials are used incorrectly - for too short a time, at too low a dose, at inadequate potency; or for the wrong disease - the likelihood that bacteria and other microbes will adapt and replicate rather than be killed is greatly

enhanced. Veterinary prescription of antimicrobials also contributes to the problem of resistance.

For all these reasons, development of alternative drugs and/or the recovery of natural molecules that would allow the consistent and proper control of pathogen-caused diseases is extremely urgent.

1.2. Antimicrobial Peptides

Antimicrobial peptides (AMPs) are small molecular weight proteins, which are a component of the innate immune system, They have been isolated from a wide range of living organisms, such as bacteria, plants, insects, mammals and amphibians, and they are active against a large spectrum of microorganisms, including bacteria and filamentous fungi. They exhibit a remarkable diversity of structures and conformations, including α-helices, β-sheets, cyclic structures, or even extended conformations, with an amphiphilic character as the only general feature.

The mechanism of action of AMPs differs from those of conventional antibiotics: they simply bind aspecifically to the bacterial membrane and alter its permeability, leading to cell death [Sitaram and Nagaraj, 1999]. The lack of a protein target is confirmed by studies showing that enantiomers of lytic peptides, composed solely of D-amino acids, possess a biological activity which is indistinguishable from that of the parent molecules [Blondelle *et al*., 1999; Juvvadi *et al*., 1996 and Papo and Shai, 2003]. For this reason most bacterial resistance

mechanisms are ineffective against AMPs, that therefore constitute a very promising target for the development of new antimicrobial agents to fight the problem of drug-resistance.

Notwithstanding the absence of specific binding, many AMPs can selectively target the membranes of microbes instead of those of mammals. This selectivity is probably due to the different lipid composition of the membranes involved (Figure 1.3): the outer layer of mammalian cells is mainly constituted of neutral and zwitterionic phospholipids and cholesterol, while the bacterial membrane contains phosphatidylglycerol or in general anionic lipids [Zasloff, 2002; Epand and Vogel, 1999 and Matsuzaki, 1998].

The spectrum of activity of antimicrobial peptides varies significantly: some of them are toxic only against Gram-positive bacteria (e. g. cecropins), others against both Gram-positive and Gram-negative bacteria (e.g. magainins and dermaseptins); some peptides can be active solely on fungi or toward both bacteria and fungi (e. g. cathelicidins).

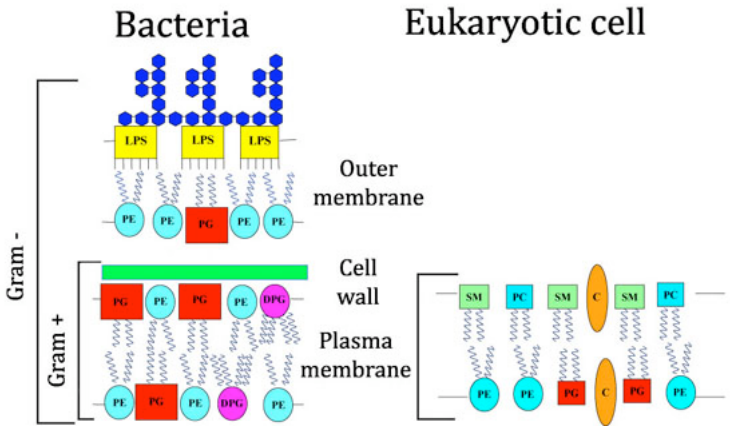

Figure 1.3. Bacterial and eukaryotic cell membrane composition. PC, phosphatidylcholine, PE, phosphatidylethanolamine and SM, sphyngomyelin are zwitterionic phospholipids, PG, phosphatidylglycerol is an anionic molecule, C is cholesterol, LPS and DPG are lipopolysaccaride and diphosphatidylglycerol or cardiolipin, respectively.

1.2.1. Mechanism of action and models

The study of peptide-membrane interactions is a fundamental step to understand the biological activity of AMPs, but the molecular details of their mechanism of membrane perturbation are still debated, and several models, summarized in Figure 1.4, have been proposed [Shai, 2002; Matsuzaki, 2001; Yang *et al*., 2001; Huang, 2000 and Pouny and Shai, 1992].

In the “barrel stave” model, peptides form a transmembrane pore, with the peptide chains aggregated laterally to form a cylindrical, barrel-like superstructure around a water-filled pore, so that their

hydrophobic surfaces interact with the lipid core of the membrane and their hydrophilic surfaces point towards the aqueous interior of the pore [Chugh and Wallace, 2001; Ludtke and Huang, 1996; Spach *et al*., 1989 and Schwarz *et al*., 1987]. The barrel-stave mechanism involves three major steps: binding of the monomers to the membrane in a helical structure, insertion into the membrane and the progressive recruitment of additional monomers to form the pore [Oren and Shai, 1998].

In the "carpet" or SMH mechanism, proposed by Shai, Matsuzaki and Huang [Ludtke *et al*., 1997; Matsuzaki *et al*., 1994 and Gazit *et al*. 1996], peptides bind onto the surface of the membrane and cover it in a carpet-like manner, laying parallel to the bilayer surface (with the hydrophobic face pointing towards the lipid core, and the hydrophilic face to water). Their accumulation on the membrane surface causes a tension between the two leaflets of the bilayer, which above a threshold concentration is released by forming local defects which cause leakage. In contrast to the barrel-stave mechanism, the peptide doesn't insert into the hydrophobic core of the membrane, but it remains always associated to the phospholipid headgroups. According to some authors, the membrane defects formed according to the carpet mechanism, might be toroidal (or worm-hole) pores [Oren and Shai, 1998; Matsuzaki, 2001; Gazit *et al.,* 1995; Ludtke *et al*., 1997], characterized by the lipid bilayer bending back onto itself in a toroidal shape.

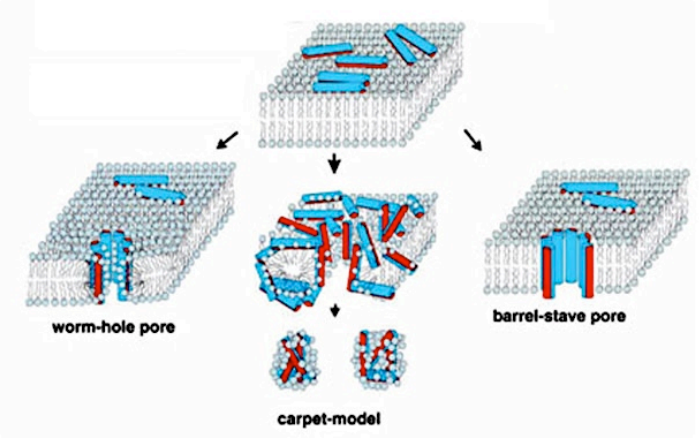

Figure 1.4. Possible mechanisms of action of antimicrobial peptides. Cylinders represent peptides; the hydrophilic and hydrophobic parts are reported in blue and in red, respectively.

In the ‘‘leaky slit’’ model [Zhao *et al*., 2006], peptides are oriented perpendicularly to the membrane, but, rather than forming a circular pore, they aggregate side to side to form an amphipathic ribbon. The hydrophobic face of the ribbon is oriented towards the hydrocarbon chains of the bilayer, while toxicity is caused by the hydrophilic face, as this side of the ribbon cannot seal with the opposing contacting bilayer by hydrophobic interactions. As a consequence, lipids are forced to adopt a highly positive curvature, causing the membrane to bend onto itself.

According to another model, peptides could act as “ion-carriers”, binding a ion or a molecule to be transferred across the membrane, and exposing their hydrophobic residues towards the outside, thus facilitating the translocation of hydrophilic species across the membrane [Roeske and Kennedy, 1983; Boheim *et al*., 1980 and Fattal

et al., 1994]. The “sinking-raft” model is another hypothesis [Pokorny *et al.,* 2002] in which several peptides form an aggregate, which can diffuse through the membrane, allowing the concomitant leakage of cell contents.

1.3. Two classes of AMPs

Even though, AMPs exhibit a wide variety of sequences and of secondary structures, helical peptides are one of the most common and best characterized groups of AMPs. However, even among helical, amphiphilic AMPs, profound differences can be observed. For instance, two of the most studied classes of helical AMPs are cathelicidins and peptaibols.

Cathelicidins are the major AMPs in mammals, and most of them are linear peptides of 20-40 amino acid residues, and it is now well established that these peptides exhibit a structural transition from an extended coil to a well-defined helical structure upon binding to membrane surfaces [Shai, 1999 and Epand and Vogel, 1999]. They have a strong cationic character, and this likely explains the fact that these peptides exhibit a strong affinity for bacterial membranes but little or no binding to zwitterionic phospholipids, which are the major component of the outer leaflet of eukaryotic cells [Oren and Shai, 1998; Matsuzaki, 1999 and Lohner and Prenner 1999].

Peptaibols, on the other hand, are linear peptides isolated from soil fungi, mainly of the genus *Trichoderma*, and are 11-20 aminoacids

in length. They contain a C-terminal alcohol group, an N-terminal acetyl group, and, most importantly, the $C^{\alpha,\alpha}$-disubstituted aminoacid Aib (aminoisobutiryc acid), [Chugh and Wallace 2001; Benedetti *et al*., 1982 and Auvin-Guette *et al.,* 1992]. The presence of geminal dialkyl substituents at the tetrahedral C(α)-atom in Aib imposes major steric restrictions on the energetically accessible conformational space [Karle and Balaram, 1990; Pispisa *et al*., 2000a and Pispisa *et al*., 2000b], and therefore all peptaibols are mostly helical even in solution. By contrast to cathelicidins, peptaibols are usually neutral, strongly hydrophobic and do not exhibit selectivity in their membrane-perturbing activity.

Two representative examples of AMPs belonging to the class of cathelicidins and peptaibols, respectively, are illustrated below.

1.3.1. PMAP-23

PMAP-23 is a member of the cathelicidin family, it was isolated in pigs [Zanetti *et al*., 1994], and it shows a broad spectrum of antimicrobial activity against both Gram-positive and Gram-negative bacteria, as well as fungi, while it has no hemolytic activity, even at a concentration of 100 μM [Zanetti *et al*., 1994 and Kang *et al*., 1999]. Indeed, its potency and selectivity make PMAP-23 a highly attractive candidate for the development of new antibiotic drugs.

Its sequence is 23 residues long and is reported below, with charged residues shown in red and hydrophobic residues in blue. It

contains two Trp residues which endow the peptide with intrinsic fluorescence.

Arg-Ile-Ile-Asp-Leu-Leu-Trp-Arg-Val-Arg-Arg-Pro-Gln-Lys-Pro-Lys-Phe-Val-Thr-Val-Trp-Val-Arg

Recent NMR and CD spectroscopic studies showed that PMAP-23 is disordered in solution, but in membrane-mimetic environments it adopts a helix-hinge-helix structure, consisting of N-terminal (residues 1-10) and C-terminal (residues 17-23) α-helical regions connected by a flexible hinge segment containing the two Pro residues [Park *et al.*, 2002] (Figure 1.5).

The mechanism of membrane-destabilization by PMAP-23 is still undetermined, and it is the object of the present work.

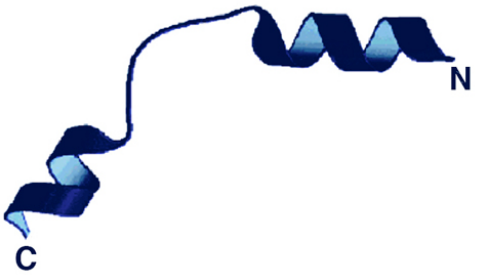

Figure 1.5. Ribbon-model representation of the backbone structure of PMAP-23 in membrane mimicking micelles, as determined by NMR. The peptide has a helix-hinge-helix structure with an overall amphipathic arrangement of the side-chains.

1.3.2. Trichogin GA IV

Trichogin GA IV is the main component of the lipopeptaibol family and was first isolated in 1992, by Bodo and coworkers [Auvin-Guette *et al*., 1992] from the soil fungus *Trichoderma longibrachiatum*. It exhibits significant activity against *S. aureus*, but it is also hemolytic [Toniolo *et al*., 1994].

It is only 11 residues long and its sequence is

Oct-Aib-Gly-Leu-Aib-Gly-Gly-Leu-Aib-Gly-Ile-Lol

where Oct is *n*-octanoyl, and Lol is leucinol.

The structure of trichogin GA IV was widely studied in methanol solution using CD, EPR and NMR data, while the crystal structure of the peptide was determined using a centro-symmetric space group obtained by co-crystallization of racemic crystals [Toniolo *et al*., 2001; Auvin-Guette *et al*., 1992; Locardi *et al*., 1998; Monaco *et al*., 1998; Toniolo *et al*., 1994 and Toniolo *et al.,* 1996]. All of these studies suggest that the peptide adopts a flexible, right-handed, mixed $3_{10}/\alpha$ helical structure, even in solution. More importantly, they suggest the structure of trichogin to be amphiphilic, with all of the hydrophobic groups (*n*-octanoyl and Leu, Ile and Lol aliphatic side chains) on one helix face and the four glycine residues form the hydrophilic face [Epand *et al.,* 1999]. This conformation is shown in Figure 1.6.

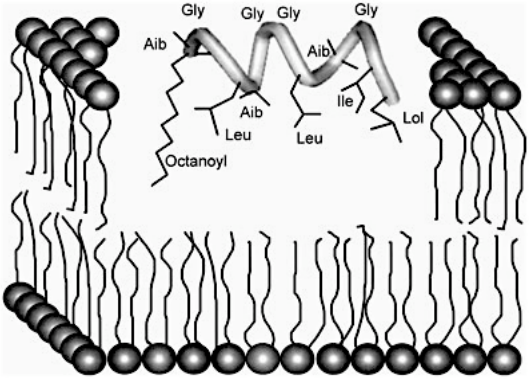

Figure 1.6. Model of a membrane-bound conformation of trichogin GA IV [Epand *et al.,* 1999].

The mode of action of this peptide has been characterized in detail by spectroscopic studies, supporting the idea that trichogin induces membrane permeability by forming channels, rather than acting as an ion-carrier or perturbing the bilayer [Mazzuca *et al*., 2005]. More in detail, these studied indicated that in the membrane trichogin undergoes a cooperative transition, driven by the concentration of bilayer-bound peptide, from a monomeric state, which is inactive and is associated at the surface of the membrane, parallel to its plane, to an aggregated state, which is inserted into the bilayer and causes membrane permeability.

1.4. Aim of the present work

As evidenced by the variety of models put forward, and described in Section 1.2, the actual mechanism of membrane perturbation by AMPs

in general is still strongly debated. This is mainly due to the difficulty in obtaining atomic-resolution structural data on peptide-membrane systems by the most powerful structural techniques (X-ray crystallography and NMR) [Lacapère *et al.,* 2007]. Hence, alternative approaches for gaining structural information in membranes would be desirable.

Optical spectroscopies, and particularly fluorescence techniques, can be easily applied to model membrane systems, and even to live cells. They can provide a wealth of information on peptide–membrane interactions, peptide location and orientation in the bilayer, and its effects on membrane structure and integrity [Stella *et al.,* 2004; Mazzuca *et al.,* 2005; Gatto *et al.,* 2006; Stella *et al*., 2007; Loura *et al.,* 2003; Stella *et al.,* 2008 and Johnson, 2005]. In this thesis, these methods were applied, together with molecular dynamics simulations, Langmuir-Blodgett and neutron reflectivity experiments, to characterize the mechanism of action of PMAP-23, chosen as a typical example of cationic, helical peptides belonging to the cathelicidin family.

In order to discuss the different mechanisms of action of AMPs, and to evidence the potential of spectroscopic methods to discriminate between the different models, the results obtained with PMAP-23 were systematically compared with those previously reported for the peptaibol trichogin GA IV.

Furthermore, a kinetic model describing the kinetics of peptide-induced vesicle leakage was proposed and discussed.

1.4.1. Peptide analogues

In the present work two single tryptophan analogues of PMAP-23 have been employed, in addition to the natural peptide. They are indicated as PMAP-W7 and PMAP-W21, to specify the position of the remaining fluorophore. Moreover, other analogues were synthesized by substituting Arg 10 or Lys14 with alanine. The amino acid sequences of the PMAP-23 analogues are reported below.

PMAP-W7

Arg-Ile-Ile-Asp-Leu-Leu-Trp-Arg-Val-Arg-Arg-Pro-Gln-Lys-Pro-Lys-Phe-Val-Thr-Val-Phe-Val-Arg

PMAP-W21

Arg-Ile-Ile-Asp-Leu-Leu-Phe-Arg-Val-Arg-Arg-Pro-Gln-Lys-Pro-Lys-Phe-Val-Thr-Val-Trp-Val-Arg

Arg10Ala

Arg-Ile-Ile-Asp-Leu-Leu-Trp-Arg-Val-Arg-Arg-Pro-Gln-Lys-Pro-Lys-Phe-Val-Thr-Val-Trp-Val-Arg

Lys14Ala

Arg-Ile-Ile-Asp-Leu-Leu-Trp-Arg-Val-Arg-Arg-Pro-Gln-Arg-Pro-Lys-Phe-Val-Thr-Val-Trp-Val-Arg

All PMAP-23 analogues were synthesized at the Research Center for Proteineous Materials (Chosun, Republic of Korea), which is involved in a joint project with our group, devoted to the determination of the mechanism of action of AMPs.

In order to perform fluorescence experiments on trichogin GA IV, which is not intrinsically fluorescent, the fluorescent analogue F10 was designed and synthesized in the laboratory of Prof. Toniolo at the

University of Padua. The fluorescent label fluorene was introduced at position 10:

Oct-Aib-Gly-Leu-Aib-Gly-Gly-Leu-Aib-Gly-Dab(Fmc)-Leu-OMe

Fmc is fluorenyl-9-methylcarbonyl, linked to the side chain of 2,4-diaminobutyric acid (Dab) (Figure 1.7).

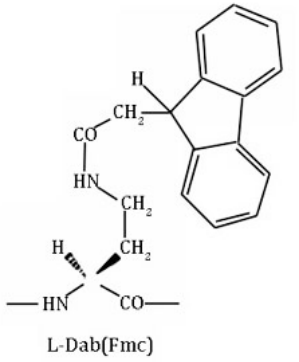

Figure 1.7. Structure of the fluorescent amino acid L-Dab(Fmc).

Chapter 2

MATERIALS, METHODS AND TECHNIQUES

2.1. Peptides synthesis

2.1.1. PMAP-23

PMAP-23 and its analogues were synthesized at the Research Center for Proteinous Materials (RCPM, Korea), by standard solid-phase synthesis [Merrifield, 1986].

The synthetic peptides were purified by RP-HPLC on Shimadzu LC-6AD and Shimadzu LC-10Avp systems using an ODS column (4.6 x 250 mm). The purified peptides were shown to be homogeneous (>98%) by analytical HPLC. The molecular weight of all synthetic peptides was confirmed using Kratos Kompact matrix assisted laser desorption/ionization time-of-flight mass spectrometry (MALDI-TOF MS, Shimadzu, Japan). In Figures 2.1 and 2.2 HPLC and mass spectra, performed at RCPM , are shown.

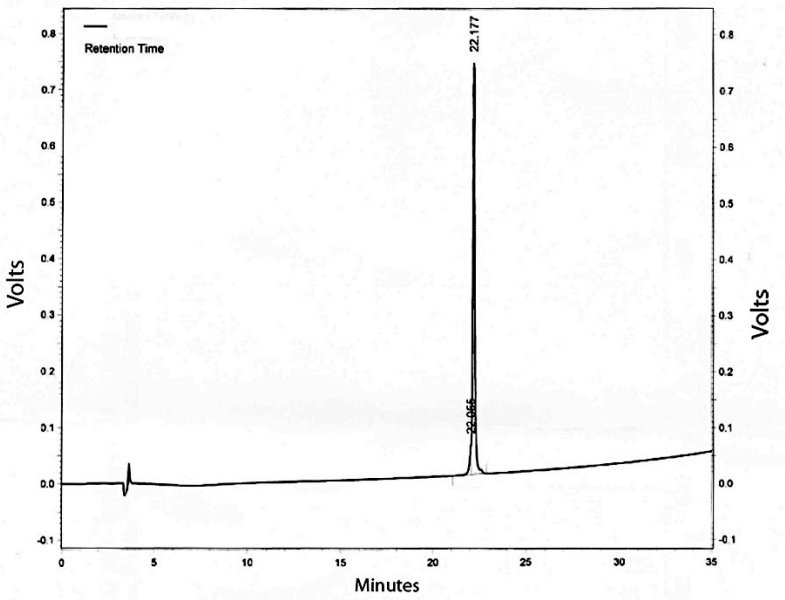

Detector A (230nm)

Pk #	Retention Time	Area	Area %
1	22.055	277828	4.711
2	22.177	5619473	95.289
Totals		5897301	100.000

Figure 2.1. HPLC elution profile of peptide PMAP-23

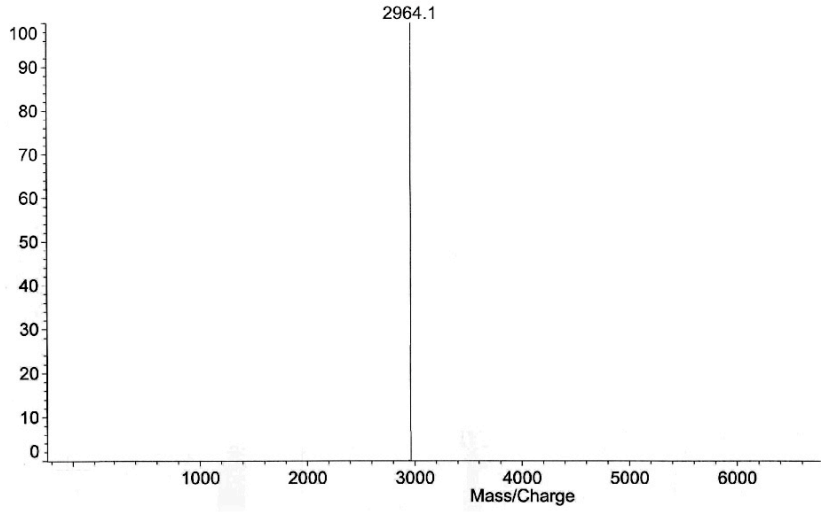

Figure 2.2. Mass spectrum of peptide PMAP-23.

2.1.2. Trichogin GA IV

Synthesis of trichogin analogues Tric-OMe and F10, used for fluorescence experiments, was performed in the laboratory of Professor C. Toniolo at the University of Padua.

Synthesis was carried out in solution using the fragment condensation approach. Peptide coupling reactions were performed by either the 1-(3-dimethylaminopropyl)-3-ethylcarbodiimide (EDC)/ HOBt (1-hydroxy-1,2,3-benzotriazole) or by the EDC/HOAt (7-aza-1-hydroxy-1,2,3-benzotriazole) method. The Fmc group was introduced into the Dab side chain using EDC/HOAt. Details of the synthesis and

characterization of peptide F10 were reported elsewhere [Didoné, 2001].

2.2. Reagents

All phospholipids were purchased from Avanti Polar Lipids (Alabaster, AL, USA). 5,6-Carboxyfluorescein, N-acetyl-tryptophan-amide (NATA), poly-L-lysine, Triton X-100, Sephadex G-50, polyethylenimine (PEI), polystyrene sulphonate (PSS), poly(allylamine hydrochloride) (PAH), tetramethyl methoxysilane, Sigmacote® and trypsin were purchased from Sigma (St. Louis, MO). Inorganic salts and spectroscopic grade solvents (Carlo Erba, Milano, Italy) were used. Polyvinyl alcohol (PVA), average M.W. 22000, 88% hydrolyzed was purchased from Acros (Geel, Belgium). 6-Dodecanoyl-N,N-dimethyl-2-naphthylamine (Laurdan) and diphenyl hexatriene (DPH) from Fluka (Buchs, Switzerland).

In Figure 2.3 the chemical structures of some fluorophores employed in the present study are shown.

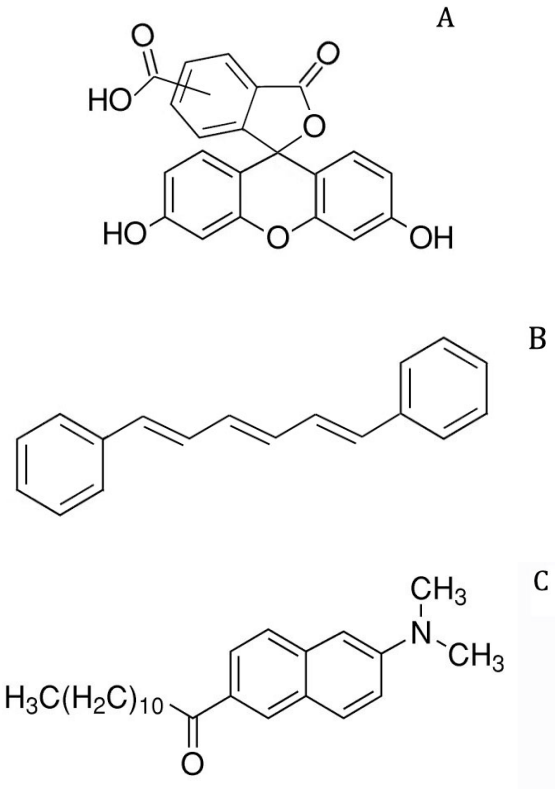

Figure 2.3. Chemical structures of 5,6 carboxyfluorescein (A), DPH (B) and laurdan (C).

2.3. Methods

2.3.1. Liposomes as membrane models

Liposomes are closed phospholipid membranes of spherical shape, separating a water compartment from the bulk water.

They are considered a good model of biological membranes, since phospholipids are the main constituents of cellular membranes. The most common phospholipids are phosphatidylcholine molecules (PC), amphipathic molecules in which a glycerol bridge links two hydrophobic acyl hydrocarbon chains to an hydrophilic polar headgroup, phosphocholine [New, 1990]. PC, also known as "lecithin", can be derived from natural sources such as egg yolk (ePC) or synthesized. The phosphatidylcholine extracted from natural sources is, actually, a mixture of phosphatidylcholines, with chains of different lengths and varying degrees of saturation.

Another important phospholipid found in nature (which has also been employed in this work) is phosphatidylethanolamine (PE), characterized by having a primary, instead of quaternary, ammonium headgroup and, consequently, a pH-dependent charge state. In order to mimic bacterial membranes, the anionic phosphatidylglycerol (PG) was mixed with the zwitterionic lipids. Figure 2.4 shows the structures of all phospholipids employed.

Moreover, sterols, and in particular cholesterol (henceforth abbreviated as Chol), are other important components of most natural membranes. Due to the rigidity of their structure, their incorporation in

the lipid bilayer can bring about major changes in the properties of the membranes, such as a reduction in the freedom of motion of the fatty acyl chain carbon atoms. Being an amphipathic molecule, cholesterol inserts into the membranes with its hydroxyl groups oriented towards the aqueous surface and the aliphatic chain aligned parallel to the acyl chains in the center of the bilayer [New, 1990].

In this thesis work, only unilamellar vesicles have been used, i.e. liposomes constituted by a single phospholipid bilayer.

Liposomes can be classified on the basis of their dimension: they are called small unilamellar vesicles (SUVs), large unilamellar vesicles (LUVs) and giant unilamellar vesicles (GUVs) if their diameters are approximately in the range 15-50 nm, 100-400 nm and 1-200 μm, respectively. LUVs and GUVs were employed in our experiments.

In order to perform some fluorescence experiments, labeled liposomes are necessary: labeled phospholipids used in the present work are shown in Figure 2.4B.

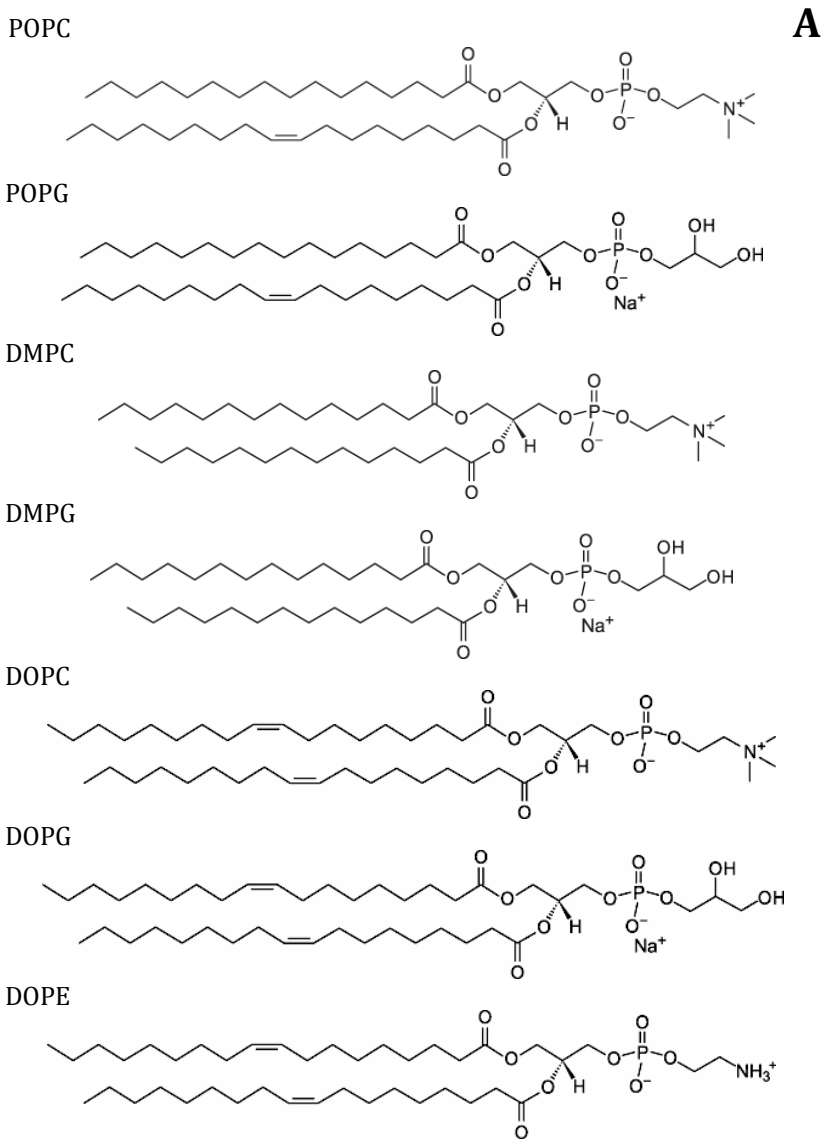

Figure 2.4A. Chemical structures of phospholipids.

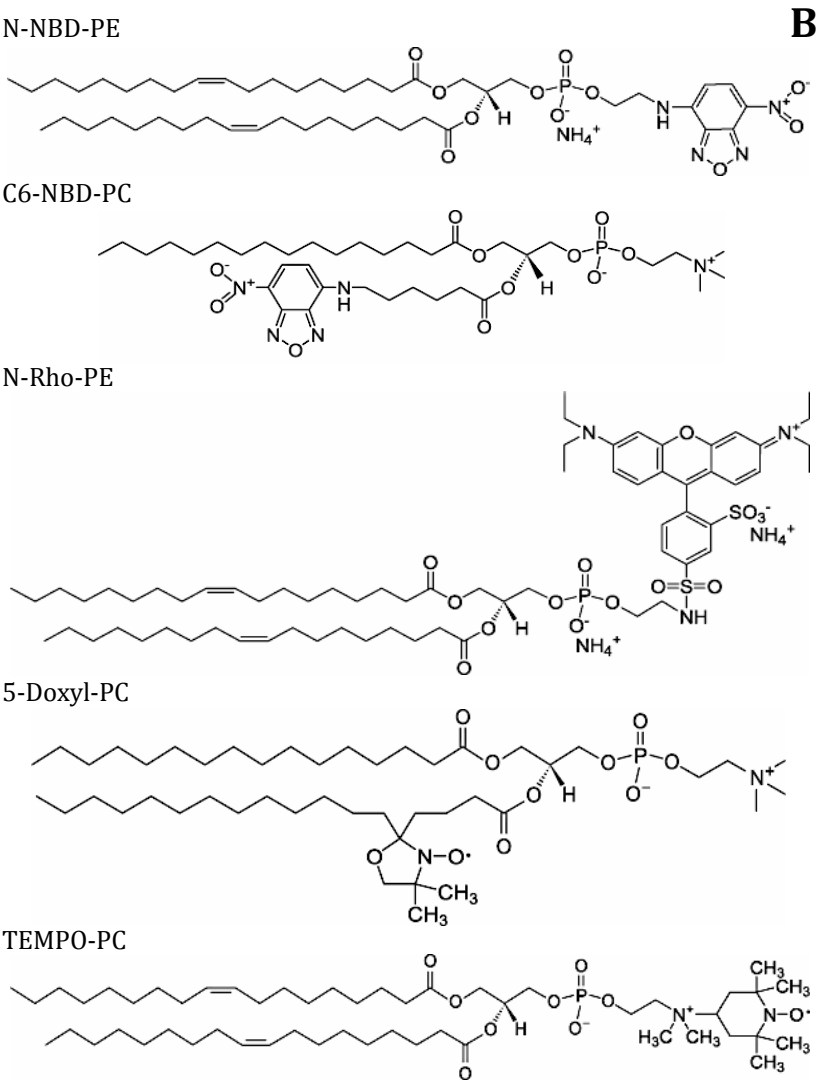

Figure 2.4B. Chemical structures of labeled phospholipids.

2.3.2. Preparation of large unilamellar vesicles

LUVs were prepared by dissolving ePC and ePG (2:1 molar ratio) in a chloroform/methanol solution (2:1 v/v). This lipid mixture has been widely used to mimic bacterial membranes; even though PC is not a bacterial lipid, this composition reproduces the content of zwitterionic and anionic lipids in the cytoplasmic membrane of bacteria. LUVs containing ePC/Cholesterol (1:1 molar ratio) were employed in the experiments with trichogin GA IV.

Methanol was added to the solvent mixture to slow down evaporation, favoring the formation of a thin and homogeneous lipid film on the flask walls. Organic solvents were evaporated under reduced argon atmosphere until the film formed. Complete evaporation was ensured by applying a rotary vacuum pump for 2 hours.

Lipids were hydrated in a 10 mM phosphate buffer (pH=7.40) containing 140 mM NaCl and 0.1 mM EDTA. For release experiments a 30 mM carboxyfluorescein solution (pH 7.0) was used to hydrate lipid film. The solution, containing large multilamellar vesicles (LMVs), was vigorously stirred and subjected to 10 freeze and thaw cycles, to achieve a better separation between lipid bilayers in LMVs.

The liposomes suspension was extruded for 31 times through two stacked polycarbonate membranes with 100 or 200 nm pores. The extruder (Avestin, Inc., Ottawa, ON, Canada) is shown in Figure 2.5. All these processes must be performed at a temperature above the melting temperature of the lipid used.

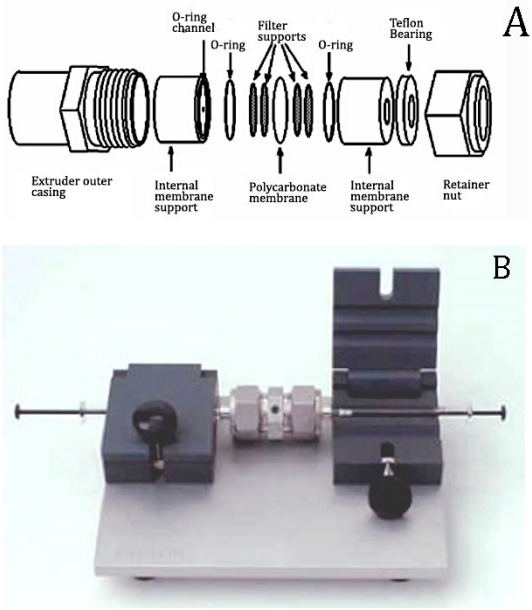

Figure 2.5. LiposoFast extruder by Avanti Polar Lipids, scheme (A) and image (B).

In the case of carboxyfluorescein loaded vesicles, the unencapsulated fluorescent molecules was separated from the liposomes by gel filtration on a Sephadex G-50 medium column.

NBD-LABELED LIPOSOMES

Liposomes containing the fluorescent lipid 1-palmitoyl-2-[6-((7-nitrobenz-2-oxa-1,3-diazol-4-yl)amino)caproyl]-L-α-phosphatidylcholine phosphatidylcholine (C6-NBD-PC) were prepared as follows [Mazzuca *et al.*, 2005]: symmetrically labeled vesicles were obtained by adding 5% (mol/mol) C6-NBD-PC to the starting chloroform solution. Liposomes containing the fluorescent label only in the internal layer were obtained by chemically quenching with

dithionite the external NBD of symmetrically labeled vesicles [McIntyre and Sleight, 1991]. The quenching reaction was performed by adding an aliquot of a 1 M dithionite solution in a Tris buffer (pH 10.0) to a 4 mM liposome solution (with a 1500:1 dithionite:NBD molar ratio). The kinetics of NBD quenching was followed by measuring fluorescence intensity. After a plateau value was reached (in 1 min), excess dithionite was removed by gel filtration. The dithionite concentration used was chosen to have a rapid reaction time, to minimize dithionite diffusion across the lipid bilayer. Complete quenching of external NBD was confirmed by the absence of a further fluorescence reduction after a second addition of dithionite to the final liposome solution. The fluorescence emission of the final internally labeled liposomes was approximately 40% of the emission intensity of the starting symmetrically labeled vesicles.

Liposomes labeled only in the external layer were prepared by adding an aliquot of a concentrated ethanolic solution of C6-NBD-PC to preformed, unlabeled vesicles, to obtain a 2.5% label molar fraction [Matsuzaki *et al*., 1996]. The final ethanol concentration was always below 1%vol/vol. The same procedure was carried out in the preparation of outer labeled vesicles containing (1,2-dioleoyl-sn-glycero-3-phosphoethanolamine-N-(7-nitro-2-1,3benzoxadiazol-4-yl) (N-NBD-PE).

DOXYL-LABELED LIPOSOMES

The degree of labeling of nitroxide-containing lipids (1-palmitoyl- 2-stearoyl(n-doxyl)-sn-glycero-3-phosphocholine, with n=5, 7, 10, 12, 14,

16, and 1,2-diacyl-sn-glycero-3-phosphotempocholine), employed for depth-dependent quenching studies, was determined by double integration of electron paramagnetic resonance (EPR) spectra [Chattopadhyay and London, 1987]. Nitroxide-labeled liposomes were produced by adding the labeled lipids to the initial chloroform solution (7% molar fraction). Spin label content was controlled directly on the final liposomes by double integration of the EPR spectra of an aliquot of the liposomes dissolved in isopropanol. EPR experiments were performed in the laboratory of professor Jens Z. Pedersen, department of biology at University Tor Vergata in Rome. All liposome preparations contained the same amount of spin labels, within a 10% error.

2.3.3. Preparation of giant unilamellar vesicles

GUVs are characterized by a diameter 1 μm or higher, very similar to those of cells.

Due to their size, they can be directly visualized under an optical microscope. This property gives rise to multiple applications of GUVs. For instance, it is possible to isolate a specific vesicle under the microscope, and/or to perfuse a membrane-active agent in the proximity of that liposome in order to visualize its effects.

GUVs were prepared by the electroformation method. To this end, a cell formed by two glass slides, covered by a thin layer of electrically conducting indium tin oxide (ITO), separated by a 1.5 mm thick silicon spacer, was employed (Figure 2.6B). A lipid film (ePC/ePG/ Rho-PE 66:33:1) was formed by spin coating a solution of the lipids in

chloroform/acentonitrile (95:5 vol/vol) on one of the two ITO slides (600 rpm, 5 minutes; Figure 2.6A).

Complete evaporation of the solvents was ensured by applying a rotary vacuum pump for at least 2 hours. The lipid film was then hydrated by filling the formation chamber with a 0.3 M sucrose, 3 μM CF solution.

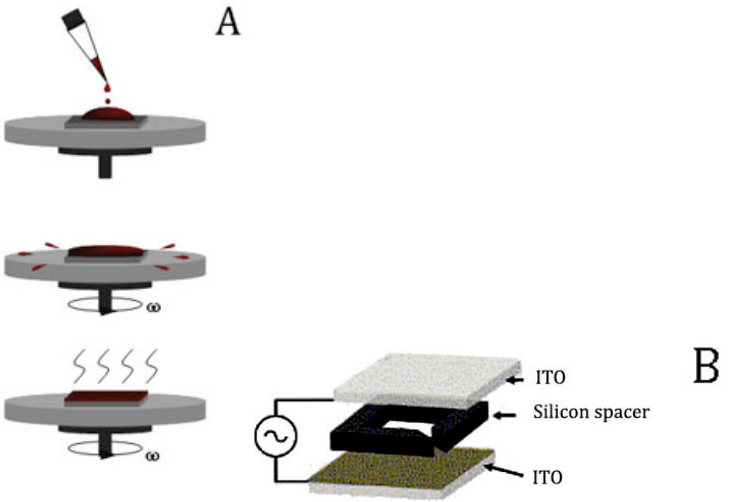

Figure 2.6. Schematic representation of the electroformation chamber (A) and of the spin-coating procedure (B).

A 1.5 V (peak to peak), 10 Hz potential was applied to the electroformation chamber, for 1 h, and then switched to 4 V, 4 Hz for 15 min to favor detachment of GUVs from the electrode. The electrostatic potential causes growth of the GUVs.

Successively the solution contained in the chamber was collected and a small aliquot was diluted 300 times in phosphate buffer solution,

on a silanized glass slide. The GUVs content and the lipid membrane could be observed independently by imaging the green CF fluorescence and the red Rho-PE fluorescence.

Silanized glass slides were employed during fluorescence imaging to allow liposome precipitation on surface without breaking.

The mechanism of GUV electroformation in an alternated field is not well understood. Probably, since the growing vesicles were observed to vibrate at the same frequency as the applied voltage, the electric field may serve to create a gentle mechanical agitation that assists in the formation, fusion and detachment of the vesicles [Estes and Mayer, 2005]. Figure 2.7 shows the fluorescence microscopic images during GUVs formation.

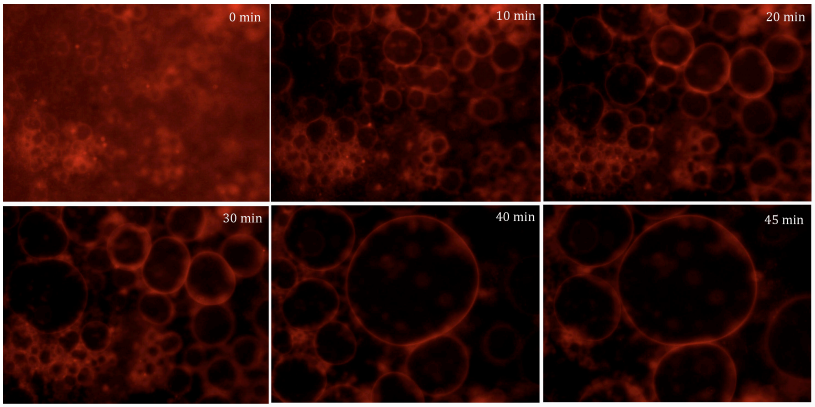

Figure 2.7. Fluorescence microscopic images of GUVs at different times during the electroformation process. Image size 498 x 365 µm (ePC 66%; ePG 33%; Rho-PE 1%).

2.3.4. Phospholipids assay

Stewart's method was employed to determine the phospholipid concentration [Stewart, 1980]. This procedure consists in measuring the absorbance of the association complex between ammonium ferrothiocyanate and the polar headgroups of the phospholipids. Since the ferrothiocyanate complex forms with the polar heads, this assay does not depend acyl chains of the phospholipids to be quantified.

1.5 mL of a 0.1 M ammonium ferrothiocyanate aqueous solution was added to 1.5 mL of chloroform solution, containing the lipid to be determined, and the test tube was vigorously shaken for 60 s to favor the formation of the complex. Complex formation between ferrothiocyanate and phospholipids brings an aliquot of the water-soluble ammonium ferrothiocyanate, proportional to the lipid concentration, in the chloroform phase. After centrifugation (5 minutes at 3800 rpm) to rapidly separate the two solvent phases, and removal of the upper aqueous phase, the chloroform solution was transferred in a quartz cuvette and its absorbance at 488 nm measured. The phospholipid concentration was determined by comparison with a calibration curve, obtained by using solutions of known title. A linear behavior was observed at least up to 0.08 μmol of phospholipid present in the chloroform solution. Calibration curves determined for ePC and for a POPC/POPG 2:1 mixture are reported in Figure 2.8. The slopes of the curves are 4.5 $\mu moles^{-1}$ and 3.4 $\mu moles^{-1}$. All the experiments were performed in triplicate.

The presence of labeled phospholipids like NBD-PE, Rho-PE at a few percent of the total lipid concentration does not affect the accuracy of the phospholipid assay.

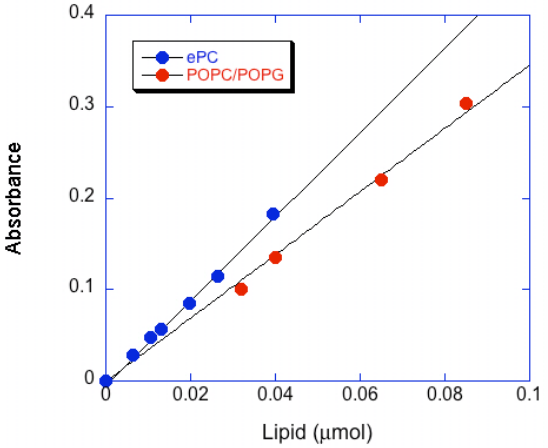

Figure 2.8. Calibration curve obtained using standard solutions of ePC (red circles) and POPC/POPG (2:1 mol/mol, blue circles). Continuous lines represent the best fits to the data.

2.4. Experimental techniques

2.4.1. Fluorescence spectroscopy

Fluorescence spectroscopy is one of the most widely used spectroscopic techniques in the field of biophysical chemistry today. Although fluorescence measurements do not provide atomic resolution structural information, the technique has become quite popular because of its

acute sensitivity to changes in the structural and dynamic of properties of biomolecules and biomolecular complexes. Furthermore, its time-scale (0.1-100 ns) is comparable to that of many biological processes (protein rotations, conformational fluctuations, etc.). Like most biophysical techniques, fluorescence spectroscopic studies can be carried out at many levels, listing from simple measurement of steady-state emission intensity to quite sophisticated time-resolved studies.

The phenomenon of fluorescence consists in the radiative decay of a molecular (or atomic) system, following the absorption of a photon from a luminous source. More in detail, when light of an opportune wavelength is absorbed by a molecule, resulting in a spectroscopic transition to a less stable, higher energy state, the dissipation of this excess energy can follow different competitive pathways: non-radiative (excited state reactions, collisions with the solvent or with other molecules, energy transfer) or radiative (fluorescence or phosphorescence). In the radiative decay, the relaxation to the ground state occurs through the emission of a photon (red-shifted with respect to the excitation wavelength, because of vibrational and solvent relaxation in the excited state) [Lakowicz, 2006a].

A fluorescence spectrum consists in registering the emission intensity of the sample at different wavelengths with a constant excitation radiation of opportune energy. Conversely, the excitation spectrum records the dependence of emission intensity at a single wavelength as a function of the excitation wavelengths.

A quantitative way to characterize the relative importance of the radiative relaxation pathway is the so-called quantum yield, q, which is

defined as the ratio between emitted photons, n_f and absorbed photons, n_a (Equation E2.1):

$$q = \frac{n_f}{n_a} = \frac{k_R}{k_R + k_{NR}} \qquad \text{(E2.1)}$$

where k_R and k_{NR} are the rate constants for the radiative (fluorescence emission) and nonradiative decay, respectively. Therefore, this quantity represents the probability that an excited system returns to the ground state by emitting a photon.

Another important parameter is the fluorescence lifetime of the probe. When a population of identical fluorophores is excited by a short light pulse, the time evolution of the emitted intensity can be represented by a single exponential function (Equation E2.2).

$$F(t) = F_0 e^{-(k_R + k_{NR})t} = F_0 e^{-t/\tau} \qquad \text{(E2.2)}$$

where F_0 and $F(t)$ are the fluorescence intensities measured just after the pulse (at t=0 s) and a given time t, respectively. The fluorescence lifetime τ is the average time that molecules spend in their excited state before returning to ground state; therefore, by definition, it is the reciprocal of the sum of the rate constants of all decay processes (Equation E2.3)

$$\tau = \frac{1}{k_R + k_{NR}} \qquad \text{(E2.3)}$$

In the absence of non radiative decay, the fluorophore lifetime is called intrinsic lifetime and is given by Equation E2.4.

$$\tau_0 = \frac{1}{k_R} = \frac{1}{A_{Em}} \qquad \text{(E2.4)}$$

where A_{Em} is the Einstein's coefficient for spontaneous emission. By combining equations (E2.3) and (E2.4) it can be shown that the quantum yield is related to the lifetime (Equation E2.5).

$$q = \frac{k_R}{k_R + k_{NR}} = \frac{\tau}{\tau_0} \qquad \text{(E2.5)}$$

Fluorescence measurements can be broadly classified into two types of measurements: steady-state and time-resolved. Steady-state measurements are those performed with constant illumination and observation. The sample is illuminated with a continuous beam of light, and the intensity or emission spectrum is recorded. Because of the ns timescale of fluorescence, most measurements are steady-state measurements. When the sample is first exposed to light, steadystate is reached almost immediately.

The second type of measurement is time-resolved, which is used for measuring intensity decays. For these measurements the sample is exposed to a pulse of light, where the pulse width is typically shorter than the decay time of the sample. This intensity decay is recorded with a high-speed detection system that permits the intensity to be measured on the ns timescale.

It is important to understand the relationship between steady-state and time-resolved measurements. A steady-state observation is simply an average of the time-resolved phenomena over the intensity decay of the sample [Lakowicz, 2006a].

SOLVENT AND ENVIRONMENTAL EFFECTS

Fluorescence spectra are usually sensible to the solvent polarity and the local environment of the fluorophore. The effects of solvent polarity are the major origin of the Stokes shift.

In solution, solvent molecules surrounding the ground state fluorophore have dipole moments that can interact with the dipole moment of the fluorophore to yield an ordered distribution of solvent molecules around the fluorophore. Transition between the ground and excited states in the fluorophore produce a change in the molecular dipole moment, which ultimately induces a rearrangement of surrounding solvent molecules. The Franck-Condon principle dictates that, upon excitation of a fluorophore, the molecule is excited to a higher electronic energy level in a far shorter time-frame than it takes for the fluorophore and solvent molecules to re-orient themselves within the solvent-solute interactive environment. As a result, there is a

time delay between the excitation event and the re-ordering of solvent molecules around the solvated fluorophore (Figure 2.9), which generally has a much larger dipole moment in the excited state than in the ground state.

However, solvent relaxation usually takes place before the fluorophore decays to the ground state, and causes a decrease in the energy of the excited state, whose amount depends on the polarity of the solvent. This is the reason of the high sensitivity of the fluorescence spectra to the polarity of the fluorophore's environment.

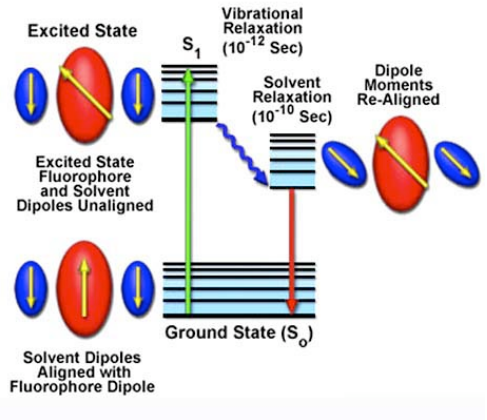

Figure 2.9. Fluorophore-solvent interactions. Ellipsoids represent fluorophore (red), and solvent molecules (blue); yellow arrows indicate dipole orientation and relative magnitude.

FÖRSTER RESONANCE ENERGY TRANSFER

A particular way to study biological systems at a molecular level employs the Förster resonance energy transfer (FRET) phenomenon.

This process consists in the transfer of excitation energy from a fluorophore in the excited state (donor) to a chromophore in its ground state (acceptor) without any emission or absorption of photons: it is caused by a resonance phenomenon due to the dipolar interaction between the donor and acceptor molecules. In order for this resonance to occur, it is necessary that the emission spectrum of the donor overlaps (at least partially) to the absorption spectrum of the acceptor. Being a stochastic process with a probability depending on the distance and mutual orientation between the two chromophores, energy transfer provides a wealth of structural information on the sample under investigation [Lakowicz, 2006a and Lakowicz, 2006g].

The energy transfer efficiency E_{FRET}, defined as the probability that an excited donor relaxes to the ground state by non radiative energy transfer, can be expressed as Equation E2.6:

$$E_{FRET} = \frac{k_{ET}}{k_{ET} + k_D^0} \qquad \text{(E2.6)}$$

where k_{ET} is the rate constant for energy transfer while k_D^0 is the rate constant for all the other decay pathways, which take place also in the absence of acceptor molecules.

According to Förster theory [Förster, 1948], the dependence of the energy transfer efficiency on the structural parameters can be expressed as:

$$E_{FRET} = \left[1 + \frac{2}{3\kappa^2} \left(\frac{r}{R_0} \right)^6 \right]^{-1} \qquad \text{(E2.7)}$$

where r is the distance between the donor and the acceptor and κ^2 a parameter depending on their mutual orientation which, in the case of fast rotation of the probes, averages to 2/3; R_0, called Förster radius, is the characteristic distance corresponding to 50% energy transfer efficiency (for κ^2 =2/3*)*. It is defined as:

$$R_0 = \left(\frac{2}{3} \alpha n^{-4} q_D^0 J \right)^{\frac{1}{6}} \qquad \text{(E2.8)}$$

where α is a constant (8.8 10^{-25} M cm^3), n is the refractive index of the medium, q_D^0 is the quantum yield of the donor when no acceptor is present and J is the superposition integral between the fluorescence spectrum of the donor (F_D) and the absorption spectrum of the acceptor (ε_A=molar extinction coefficient), weighted by λ^4 (λ being the wavelength of the radiation), as displayed in Equation E2.9.

$$J = \frac{\int_0^{\infty} F_D(\lambda)\varepsilon_A\lambda^4\, d\lambda}{\int_0^{\infty} F_D(\lambda) d\lambda} \qquad \text{(E2.9)}$$

Experimentally, energy transfer efficiency can be measured both by steady-state and time-resolved fluorescence, shown in Equation E2.10.

$$E_{FRET} = 1 - \frac{q_D^A}{q_D^0} = 1 - \frac{\tau_D^A}{\tau_D^0} \qquad \text{(E2.10)}$$

In Equation E2.10, $q^A{}_D$ ($\tau^A{}_D$) and $q^0{}_D$ ($\tau^0{}_D$) are the donor quantum yields (lifetimes) measured in the presence and in the absence of the acceptor, respectively. If the energy transfer acceptor is a fluorophore, steady state FRET efficiency can also be experimentally determined, by measuring the increase of its emission signal after interaction with the donor. In particular, when donor molecule are absent, the acceptor fluorescence intensity (at the excitation wavelength used in FRET experiments) is expressed in Equation E2.11:

$$F_A^0 \propto q_A A_A \qquad \text{(E2.11)}$$

where q_A and A_A are the quantum yield and the absorbance of the acceptor respectively, and the superscript refers to the absence of donor.

In the presence of donor molecules, this quantity increases, due to energy transfer according to Equation E2.12:

$$F_A^D \propto q_A A_A + E_{FRET} q_A A_D \qquad \text{(E2.12)}$$

Here, F^D_A is the fluorescence intensity of acceptor in the presence of donor molecules and A_D is the absorbance of the donor at the excitation wavelength.

Combining Equations E2.11 and E2.12, the relative increase in the acceptor fluorescence as a function of transfer efficiency can be easily obtained (Equation E2.13):

$$\frac{F_A^D}{F_A^0} = \frac{q_A A_A + E_{FRET} q_A A_D}{q_A A_A} = 1 + \frac{A_D}{A_A} E_{FRET} \qquad \text{(E2.13)}$$

FLUORESCENCE ANISOTROPY

Anisotropy measurements are commonly used in the applications of fluorescence to biomolecules, and provide information on the size and shape of proteins or the rigidity of their molecular environment. Anisotropy measurements are particularly useful to study association

process or the local viscosity of the fluorophore's environment [Lakowicz, 2006a].

In this technique the sample is excited by linearly polarized light: the probability of excitation of a given molecule is proportional to $cos^2\theta$ (where θ is the angle between the excitation transition dipole of the probe and the polarization direction). Consequently, a "photoselection" is performed, and the excited molecules have their transition dipoles oriented preferentially in the direction of the excitation radiation. The emission photons have a polarization direction that is again distributed with a $cos^2\theta$ law with respect to the emission transition dipole orientation. Therefore, in the absence of diffusional motions, the emitted light is anisotropic: the fluorescence polarized parallel ($I_{//}$) with respect to the excitation polarization direction is more intense than the perpendicular one ($I_{\perp}$) [Lakowicz, 2006a].

To characterize on a quantitative basis this phenomenon, an experimental observable called fluorescence anisotropy, r, is introduced in Equation E2.14:

$$r = \frac{I_{//} - I_{\perp}}{I_{//} + 2I_{\perp}} \qquad \text{(E2.14)}$$

The anisotropy is a dimensionless quantity that is not dependent on the total intensity of the sample.

For a completely polarized fluorescence $I_{\perp}=0$ and therefore $r=1$, while for depolarized fluorescence $I_{//}=I_{\perp}$ and hence $r=0$.

Actually, the maximum observable anisotropy (called fundamental or limiting anisotropy and observable by performing measurements on a diluted sample in glycerol at –20 °C) is <1, and in particular is defined as:

$$r_0 = \frac{3\cos^2\theta - 1}{5} \qquad \text{(E2.15)}$$

where θ is the angle between the absorption and emission transition dipoles of the fluorescent probe: in the case of parallel transition dipoles (θ =0) a limiting value of 0.4 is obtained [Lakowicz, 2006f].

Measurement of r provides information about the relative angular displacement of the fluorophore between the times of absorption and emission. In fluid solution most fluorophores rotate extensively in 50 to 100 ps. Hence, the molecules can rotate many times during the 1–10 ns excited-state lifetime, and the orientation of the polarized emission is randomized. For this reason fluorophores in non-viscous solution typically display anisotropies near zero. The effects of rotational diffusion can be decreased if the fluorophore is bound to a macromolecule. Moreover, measurements of fluorescence anisotropy are sensitive to any factor that affects the rate of rotational diffusion. The rotational rates of fluorophores in cell membranes also occur on the nanoscale timescale. Therefore, measurements of fluorescence polarization are widely used to study the fluidity and mobility of biological membranes.

2.4.2. Experimental details

INSTRUMENTAL APPARATUS

Emission spectra and anisotropy values were obtained by steady-state fluorescence experiments on a thermostated Fluoromax-2 fluorimeter (Horiba Jobin Yvon). Anisotropy experiments were performed by equipping the spectrofluorimeter with Glan-Thomson polarizer prisms.

Time-resolved fluorescence measurements were performed on a Lifespec-ps setup (Edinburgh Instruments) equipped with automatic Glan-Thompson polarizers, a cooled micro-channel plate detector, and a 298 nm pulsed diode laser (1 ns pulse width) and working in the time-correlated single photon counting mode.

WATER-MEMBRANE PARTITION

Tryptophan emission spectra were recorded as follows: λ_{exc}=280 nm and λ_{em}=300-450 nm, slits 1 and 5 nm for excitation and emission respectively, integration time 1 s. Fluorescence spectra were recorded some minutes after the vesicles addition, to allow the equilibration.

LIPOSOMES' RELEASE

PMAP-23 and its analogues were incubated with ePC/ePG vesicles (lipid concentration 0.2 mM), containing 30 mM 5,6-carboxyfluorescein. Trypsin was in a final concentration of 50 μg/mL. The CF fluorescence intensity was measured by setting the following parameters: λ_{exc}=490 nm, λ_{em}=520 nm, integration time 0.2 s. Triton X-100 was added at a final concentration of 1.4 mM.

DEPTH-DEPENDENT QUENCHING

The fluorescent peptide analogues were added to the different nitroxide labeled liposomes (at a lipid concentration of 0.2 mM) and to a reference unlabeled liposome solution, and steady-state fluorescence intensities were determined after a 20 min equilibration period. The reported values are the average of triplicate experiments.

LIPID FLIP-FLOP

Vesicles labeled in the inner layer with C6-NBD-PC (lipid concentration 200 μM) were incubated for 20 min with different concentrations of PMAP-23, to cause peptide-induced lipid flip-flop. Successively, the peptide was digested by incubating with 2 μM of trypsin for 10 min, to remove any peptide-induced membrane pores. NBD fluorescence was excited at 460 nm and monitored at 520 nm.

FRET EXPERIMENTS

Experiments of PMAP-23 exchange between different vesicles were carried out by incubating the peptide (5 μM) with vesicles labeled with the fluorescent lipid N-NBD-PE, which quenches the intrinsic peptide tryptophan fluorescence by acting as an energy-transfer acceptor (lipid 0.2 mM). Peptide exchange between vesicles was monitored by measuring the decrease in energy transfer following addition of unlabeled vesicles (final concentration 0.8 mM). Fluorescence intensity was recorded with an excitation wavelength of 280 nm.

EFFECTS ON MEMBRANE DYNAMICS

Liposomes were formed by DMPC or DMPC/DMPG in a 2 : 1 molar ratio, and contained the fluorescent probe (DPH) 1,6-diphenylhexatriene in a fluorophore/lipid molar ratio of 1:100. The fluorescence anisotropy was determined by recording the fluorescence intensity with excitation and emission wavelengths of 350 nm and 450 nm, respectively, 4 nm band pass, a WG385 cut-off filter in the emission channel, and averaging nine replicate determinations for each measurement. Temperature was controlled by a thermostatted cuvette holder to within 0.1 ˚C. In the case of PMAP-23, 50 μM DMPC/DMPG vesicles were used and a 10 μM peptide concentration, while for Tric-OMe 0.2 mM DMPC vesicles were used and a 24 μM peptide concentration. Background counts were subtracted before anisotropy calculations.

It is important to note that it was necessary to determine an instrumental parameter, the *G* factor, which is the ratio of the sensitivities, *S*, of the detection system for vertically and horizontally polarized light. For vertically polarized excitation the observed polarized intensities are defined in Equations E2.16, where I_{VV} and I_{VH} are the intensities measured with vertically polarized excitation and vertically polarized emission and vertically polarized excitation and horizontally polarized emission, respectively, k is a proportionality factor to account for polarization-independent instrumental factors.

$$I_{VV} = kS_V I_{//} \text{ and } I_{VH} = kS_H I_{\perp} \qquad \text{(E2.16)}$$

The combination of Equation E2.16 gives Equation 2.17.

$$\frac{I_{VV}}{I_{VH}} = \frac{S_V I_{//}}{S_H I_{\perp}} = G\frac{I_{//}}{I_{\perp}} \qquad \text{(E2.17)}$$

The G factor is easily measured using horizontally polarized excitation. With horizontally polarized excitation the excited-state distribution is rotated to lie along the observation axis. When this is done both the horizontally and vertically polarized components are equal and proportional to $I_{\perp}$. These components are equal because the electric field is equally distributed around the observation axis. Both polarizer orientations are perpendicular to the polarization of the excitation. Any measured difference in I_{HV} and I_{HH} must be due to the detection system, as shown in Equations E2.18.

$$I_{HH} = kS_H I_{\perp} \text{ and } I_{HV} = kS_V I_{\perp} \qquad \text{(E2.18)}$$

The *G* factor can be calculated by Equation E2.19.

$$\frac{I_{HV}}{I_{HH}} = \frac{S_V I_{\perp}}{S_H I_{\perp}} = G \qquad \text{(E2.19)}$$

By combining the previous equations with Equation E2.14, the fluorescence anisotropy *r* can easily be calculated as:

$$r = \frac{I_{VV} - GI_{VH}}{I_{VV} + 2GI_{VH}} \qquad \text{(E2.20)}$$

The laurdan experiments were performed by measuring the GP values, defined in paragraph 3.3.7, of DMPG/DMPC and DMPC liposomes containing Laurdan at a concentration that has been reported to not affect the membrane phase transition [Abrams and London, 1993] i.e. 1% and 5% molar ratio, in DMPG/DMPC and DMPC respectively, in the temperature range from 6°C to 80°C. Laurdan emission spectra were recorded under the following experimental conditions: λ_{exc}=360 nm, λ_{em}=400-500 nm and 3 nm band pass. Each spectrum was repeated twice.

STOPPED-FLOW

Stopped-flow experiments were performed on a SX.18 MV apparatus (Applied Photophysics Limited, Leatherhead, U.K.) with a fluorescence detector and a nominal mixing time of 1 ms. Temperature was controlled to 25°C. Mixing of asymmetric volumes (1:10 alcoholic peptide solution/aqueous liposome solution) was employed. Samples were excited at 265 nm, and emission was collected using an emission cut-off filter at 305 nm or 385 nm.

2.4.3. UV-visible absorption

All the absorbance experiments were carried out at room temperature with a Cary 100 Scan spectrophotometer (Varian, Middelburg, Netherlands).

Concentration of PMAP-23 and its analogues was determined from the absorbance values at 280 nm, considering that the molar extinction coefficient of Trp is $\varepsilon_{280\ nm}$= 5690 cm^{-1} M^{-1}.

The concentration of the trichogin GA IV fluorescent peptide analogue F10 was determined by measuring the absorbance of the chromophore linked to the peptide chain (λ=301 nm for Fmc) and comparing it to the corresponding calibration curves that gives a molar extinction coefficient $\varepsilon_{301\ nm}$= 6.3 10^4 M^{-1} cm^{-1}.

2.4.4. Neutron Reflectivity

Neutron reflectometry is a relatively new technique that has widespread applications as a powerful analytical tool to analyze interfacial structure and composition. The specular reflection of neutrons gives information about inhomogeneities (composition or concentration distributions) normal to an interface or surface [Penfold *et al.,* 1997]. For the study of problems in surface chemistry the possibility of modifying the refractive index profile at a surface or interface through hydrogen/deuterium (H/D) isotopic labelling makes neutron reflectivity a particularly powerful and selective technique.

The basis of the specular neutron reflection method is that the variation in specular reflection with wave vector transfer, *Q*, defined in Equation E2.21:

$$Q = \frac{4\pi \sin \vartheta}{\lambda} \qquad \text{(E2.21)}$$

(where λ is the neutron wavelength and ϑ is the glancing angle of incidence) is related to the composition or density profile in the direction normal to the interface.

Neutron reflection experiments were carried out on the SURF reflectometer at the ISIS facility, a pulsed neutron source at the Rutherford Appleton Laboratory (RAL) in Didcot, UK. The measurements were performed at different fixed angles of incidence using a broad range of incident wavelengths (0.5-7.0 Å), the "white beam", time-of-flight method. This offers the advantages of fixed geometry, constant illumination and resolution, and the ability to measure a wide region of the reflectivity profile simultaneously. These features, coupled with the beam inclined at 1.5° to the horizontal, provides convenient and easy access to the liquid surface [Penfold *et al.,* 1997].

Membranes were prepared in situ, by a methodology [Vacklin *et al.,* 2005] which uses a lipid/detergent mixture to deposit a single POPC bilayer on the silicon surface (Figure 2.10). Trichogin GA IV was added to the POPC membrane at increasing concentrations of 2, 6 and 15 μM,

and the reflectivity was measured after each addition. After the highest concentration the membrane was washed with D_2O buffer, and a further measurement was acquired. Finally, the second peptide (PMAP-23) was added, at concentrations of 5 and 20 μM, before washing with D_2O. A reflectivity profile was taken after each step.

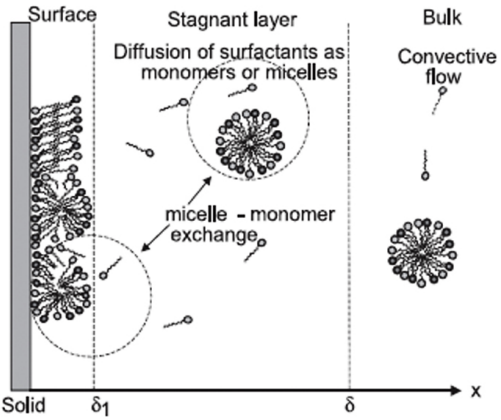

Figure 2.10. Adsorption of mixed micelles of insoluble phospholipids (dark grey) and a nonionic surfactant (pale grey). δ denotes the thickness of the stagnant layer within which the bulk concentration is reduced due to adsorption at the surface, and δ_1 defines the thickness of the surface region. [Vacklin *et al*., 2005]

2.4.5 Langmuir-Blodgett

The Langmuir-Blodgett technique offers the possibility to study the influence of proteins or peptides adsorbing in a lipid monolayer at the water-air-interface.

Phospholipids, solubilized in chloroform are deposed dropwise at the water surface with a microliter syringe (Hamiltion syringe). The solvent evaporates quickly and leaves a spreaded, monomolecular and orientated film on the surface: the hydrophilic headgroups are oriented towards the subphase, the hydrophobic chains towards the air.

The area of the monomolecular film can be compressed by a movable barrier. It slides over the edge driven by a stepper motor (Figure 2.11).

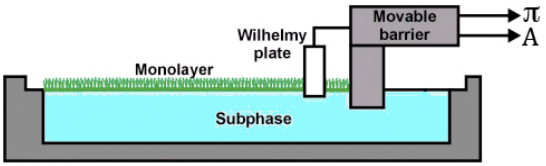

Figure 2.11. The essential components of a Langmuir trough.

A computer-controlled film balance Langmuir trough (KSV Microtrough, KSV Instruments, Helsinki, Finland), equipped with a platinum Wilhelmy plate was used to obtain the surface pressure-area (π–A) isotherms of monolayers at the air/water interface. The temperature was maintained at 20 ˚C by an external water bath circulation. The volume of the trough was 60 ml. The cleanliness of the surface was ensured by closing the barriers, followed by aspiration of the subphase surface, before each experiment, that was started only when the fluctuation of the surface pressure was about 0.2 mN/m during the compression cycle. The lipid mixture POPC/POPG 2:1 was spread from a 1 mM solution on a 10 mM phosphate buffer subphase at

pH 7.4. Several minutes were allowed for solvent evaporation from the interface.

The air/water interface was then compressed with two Delrin barriers at a rate of 2 $Å^2$ $molec^{-1}$ min^{-1}. The accuracy on surface pressure was within 0.1 mN/m.

After a surface-pressure of 20 mN/m was reached, a value close to the physiological pressure of membranes [Schwarz and Taylor, 1999], the system was left to equilibrate before the addition of PMAP-23 in the subphase, through a hole in the trough.

By keeping the surface-pressure constant, the variation of the monolayer area was recorded in order to determine the monolayer perturbation induced by the peptide [Schwarz, and Taylor, 1999].

2.4.6. Molecular Dynamics simulations

Molecular dynamics simulations were performed according to the "minimum bias" method proposed by Esteban-Martín and Salgado [Esteban-Martín and Salgado, 2007]. Briefly, PMAP-23 was initially shaped in a canonical α-helix, with extended side chains, and positioned at the center of a cubic box with a side of 8.5 nm. 32 POPG molecules (16 molecules for each of the two possible chiralities of POPG) and 96 POPC molecules, with different conformations taken from equilibrated simulations of phospholipid bilayers [Tieleman *et al*., 1999], and then 5026 water molecules were added randomly in the box. Finally, 26 Na^+ ions were introduced in substitution of 26 randomly selected water

molecules, to ensure system neutrality. MD simulations were performed with GROMACS 3.3, using *ffgmx* parameters [van der Spoel *et al*., 2005]. The details of the MD procedure are described elsewhere [Orioni *et al.,* 2009]. Molecular graphics were obtained with the program VMD [Humphrey *et al*., 1996].

The MD simulation procedure employed with trichogin GA IV was similar to that of PMAP-23 [Bocchinfuso *et al*., 2009].

Chapter 3

RESULTS AND DISCUSSION: MECHANISM OF ACTION OF PMAP-23

3.1. Antimicrobial activity

The antimicrobial activity of PMAP-23 and its analogues against Gram-negative and Gram-positive bacteria and their lytic activity against hRBCs were evaluated at RCPM (Korea). Listed in Table 3.1 are the antimicrobial activities of the peptides expressed in MICs. PMAP-23, PMAP-W7 and PMAP-W21 showed a similar potency toward all tested microorganisms, with MICs ranging from 2 to 16 μM. Peptides didn't show any hemolytic effect up to 128 μM on hRBCs [Yang *et al*., 2006].

	G (+)		G (-)	
Peptide	*S. aureus*	*B. subtilis*	*E. Coli*	*P. aeruginosa*
PMAP-23	4	2	2-4	4-16
PMAP-W7	4	2-4	4	8-16
PMAP-W21	4	2	2-4	4-16

Table 3.1. Minimal inhibitory concentrations (μM) for PMAP-23 and its analogues.

The similar antimicrobial activities of the peptides allow us to consider the PMAP-23 analogues as a good model for the study of the natural peptide, its interaction with lipid bilayers.

3.2. Peptide behavior in water

3.2.1. Adsorption to cuvette walls

PMAP-23 and its analogues display significant biological activity at very low concentrations, in the μM range. Experiments with amphiphilic peptides in this concentration range are usually complicated by significant adsorption phenomena to the container walls. This is a common drawback to many antimicrobial peptides, dissolved in water, because of their amphiphilic nature. The problem is particularly severe in containers with a high surface to volume ratio (such as reduced volume cuvettes), in the absence of liposomes (which have a much higher affinity for the peptide than the cuvette walls), and at low peptide concentration.

The adsorption phenomenon can be detected by a decrease in the peptide fluorescence signal over time, because the bulk fluorophore concentration is reduced as molecules adsorb to cuvette's walls (Figure 3.1).

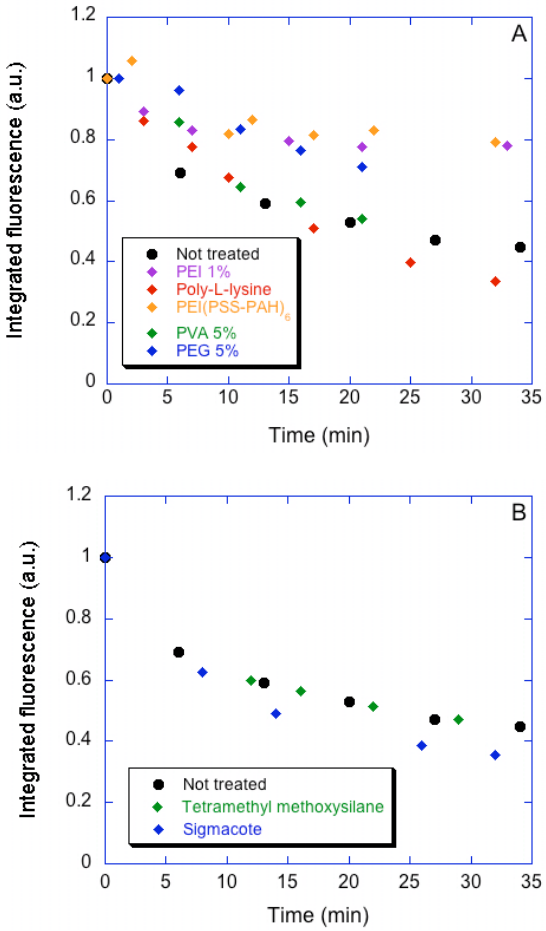

Figure 3.1. Intensity decay of PMAP-W21 (1 μM) in buffer, in 10 x 10 mm quartz cuvette pre-treated with different hydrophilic polymers, A and with apolar coatings, B. λ_{exc} = 280 nm and λ_{em} = 355 nm.

In order to reduce this problem, quartz cells were incubated with solutions of different polymers: positively charged, such as polyethyleneimine (PEI) [Persson *et al.*, 2003] and poly-L-lysine, or hydrophilic, such as poly-vinyl alchol (PVA) [Barret *et al.,* 2001] and

poly-ethylen glycol (PEG). These macromolecules adsorb to the container walls, forming a stable film that can avoid peptide adhesion by modifying the surface. In order to improve the surface coverage, a multilayer system was constituted by successive ("layer by layer") deposition of the polyelectrolytes polystyrenesulfonate (PSS) and polyallylamine hydrochloride (PAH) after a first PEI layer [Kolasińka and Warszyński, 2005]. Finally, cuvette treatment was performed also with apolar coatings such as tetramethyl methoxysilane (TMMS) and Sigmacote® that bind covalently to the surface. After all these treatments, cuvettes were rinsed copiously with deionized water.

The kinetics of peptide adsorption, determined by the decrease of Trp fluorescence intensity, are shown in Figure 3.1. The most efficient reduction in peptide adsorption was obtained with PEI, PEG and the multilayer system. In all the experiments described in the following sections, a PEI cuvette treatment was employed, while PEG was used in experiments where anionic liposomes were present, in order to avoid interactions between the vesicles and the cationic PEI polymer. It is worth noting that, even if these treatments do not abolish completely peptide adsorption under the conditions employed in the experiments reported in Figure 3.1, this phenomenon could be neglected at higher peptide concentrations (~10 μM) or in the presence of liposomes.

3.2.2. Aggregation

Some antimicrobial peptides have a tendency to self-aggregate in water solutions because of their amphiphilic character. This phenomenon is evidenced by the absorption spectrum of 1 mM aqueous solutions of PMAP-23 and its analogues (Figure 3.2). All peptides exhibited the characteristic tryptophan absorption band, with a maximum at 280 nm, but PMAP-W21 showed also a significant background, due to light scattering caused by peptide aggregates.

Aggregation in water represents a fundamental aspect of the biological activity of antimicrobial peptides since it can compete with membrane-binding [Stella *et al.,* 2007]. In order to find out whether a concentration range exists where aggregation is negligible for all PMAP-23 analogues, light scattering was measured as a function of peptide concentration, both from turbidity measurements at 350 nm (a wavelength where Trp absorbance is negligible), and from the intensity of light scattered at 90° (Figure 3.3). Both these experiments demonstrate that below a concentration of 15 μM, aggregation can be neglected for all analogues, including PMAP-W21. For this reason, all the experiments described in the following sections were performed below this concentration threshold.

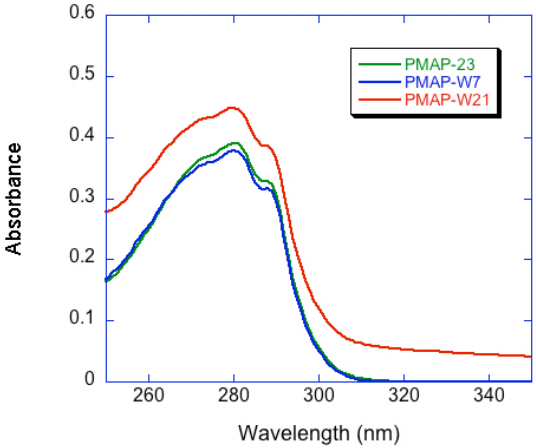

Figure 3.2. UV absorption spectra of peptides in buffer solution, at a nominal 1 mM concentration. PMAP-23 spectrum was reported after division by 2, to consider the presence of 2 tryptophan residues in this peptide. Pathlength 1 mm.

In order to determine if the fluorescence properties of the peptides are affected by aggregation, lifetime measurements were performed as a function of PMAP-W21 concentration. Even in the monomeric form, the fluorescence decay is multiexponential, as commonly observed for Trp emission, due to rotamer equilibria of the side chain [Lakowicz, 2006b].

Figure 3.4 reports the time decay of PMAP-W21 and the average lifetime as a function of peptide concentration. In contrast to what was observed for other peptides (e.g. trichogin GA IV [Stella *et al.*, 2004]), the fluorescence decay of PMAP-W21 was the same both below and above the 15 μM concentration threshold for the aggregation of this peptide. Since this parameter is extremely sensitive to the fluorophore's

environment [Lakowicz, 2006c], this finding suggests that the aggregate structure leaves the indole ring exposed to the aqueous phase.

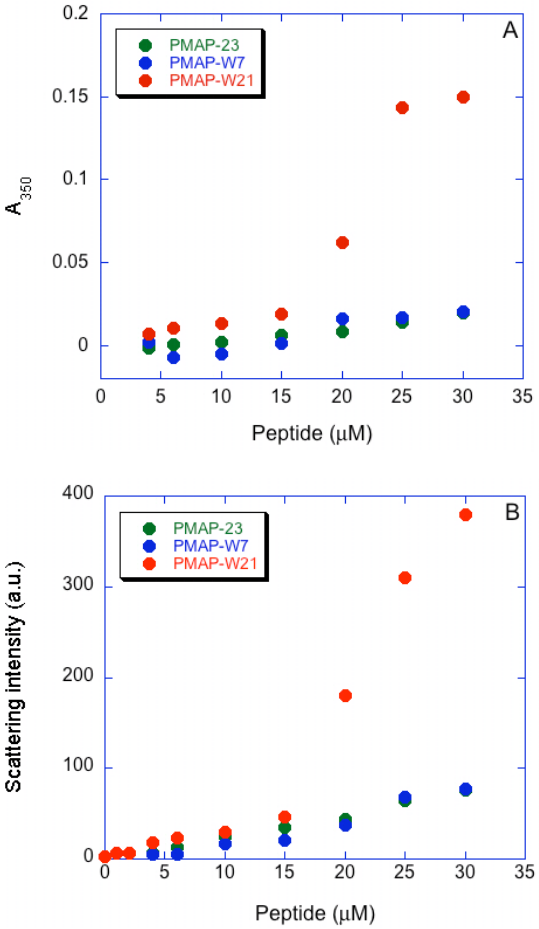

Figure 3.3. Experiments on peptide aggregation in water (10 mM phosphate buffer, pH 7.4 containing 0.1 mM EDTA). Panel A: absorbance at 350 nm (pathlength 1 cm). Panel A: Scattering intensity detected at 90° (λ=400 nm, 10x4 mm cuvette).

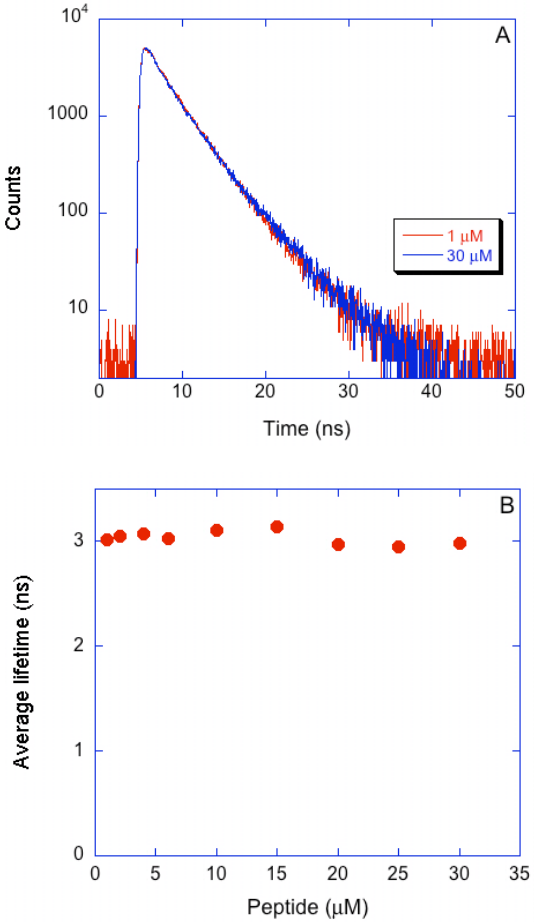

Figure 3.4. Fluorescence experiments on peptide aggregation in water. Panel A: time decay of PMAP-W21. Panel B: average fluorescence lifetime of PMAP-W21. λ_{exc} = 298 nm and λ_{em} = 355 nm, 10x4 mm quartz cuvette.

It is interesting to compare these findings with what was previously observed for the fluorescent analogue F10 of neutral peptaibol trichogin GA IV [Stella *et al.*, 2004]. In this case the fluorescence time-decay of the fluorene emission is monoexponential,

and aggregation causes a significant change in the lifetime (Figure 3.5, taken from [Stella *et al.*, 2004]). Therefore, time-resolved measurements allowed a direct determination of the fraction of aggregated peptide. Trichogin GA IV exhibits a much higher tendency to aggregate than PMAP-23 and its analogues: an almost complete aggregation is attained at 15 μM concentration, and even at 1 μM this phenomenon can not be neglected. This difference is obviously due to the different hydrophobicity and charge of the two peptides, but it influences profoundly their interaction with membranes, since trichogin GA IV aggregation competes with its membrane binding [Stella *et al.*, 2004].

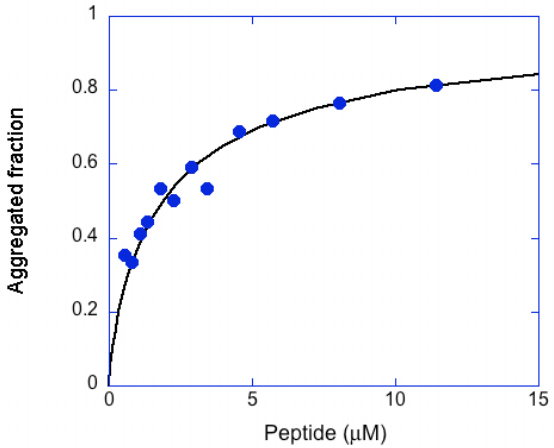

Figure 3.5. Fraction of F10 molecules participating in peptide aggregates, as a function of total peptide concentration [Stella *et al.*, 2004].

3.3. Peptide behavior in membranes

3.3.1. Water-membrane partition

The affinity of antimicrobial peptides for phospholipid membranes is an important determinant of their activity, since it defines the quantity of peptide which associates to the lipid bilayer and can perturb its permeability. For this reason, a quantitative study of peptide association to lipid vesicles was carried out.

Since PMAP-23 and its analogues contain tryptophan residues, their fluorescence emission was used to assess the degree of binding through changes in the local polarity of the environment of the tryptophan.

An aqueous solution of peptide in a quartz cell was titrated with increasing concentrations of ePC/ePG (2:1 mol/mol) liposomes [White *et al.,* 1998]. In the presence of vesicles, a significant and progressive increase in fluorescence intensity was observed and a visible blue shift occurred (Figure 3.6). The emission shift is due to a change in the polarity of the fluorophore's environment, while the increase in quantum yield indicates a decrease in nonradiative processes, due to a less dynamic environment. Therefore, both changes suggest fluorophore association to the lipid bilayer.

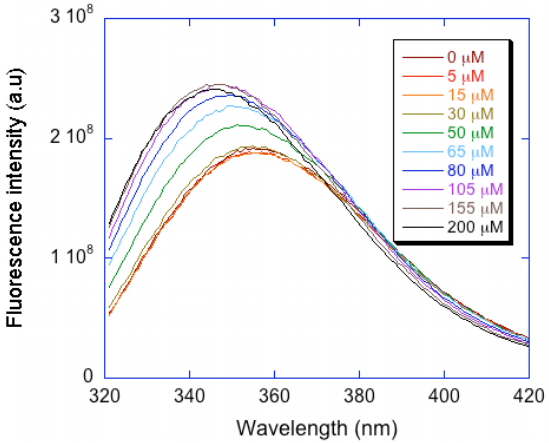

Figure 3.6. Fluorescence emission spectra of PMAP-23 as a function of lipid concentration. λ_{exc} = 280 nm, 10x10 mm quartz cuvette.

The observed fluorescence intensity, at a given lipid concentration is a function of the molar fraction of membrane-bound peptide. Therefore, the peptide fraction associated to the lipid bilayer was determined by the variation of fluorescence intensity, according to Equation E3.1.

$$f_M([L]) = \frac{F([L]) - F_W}{F_M - F_W} \qquad \text{(E3.1)}$$

where F, F_W and F_M are fluorescence intensities at 340 nm, measured at a given lipid concentration, in the absence of vesicles and in a completely membrane-bound state, respectively.

The results of this experiment are shown in Figure 3.7, the three analogues exhibited a comparable affinity for membranes, with a

complete binding at lipid concentrations higher than 150 μM. The fraction of membrane-bound peptide, f_M is reported in Figure 3.7A.

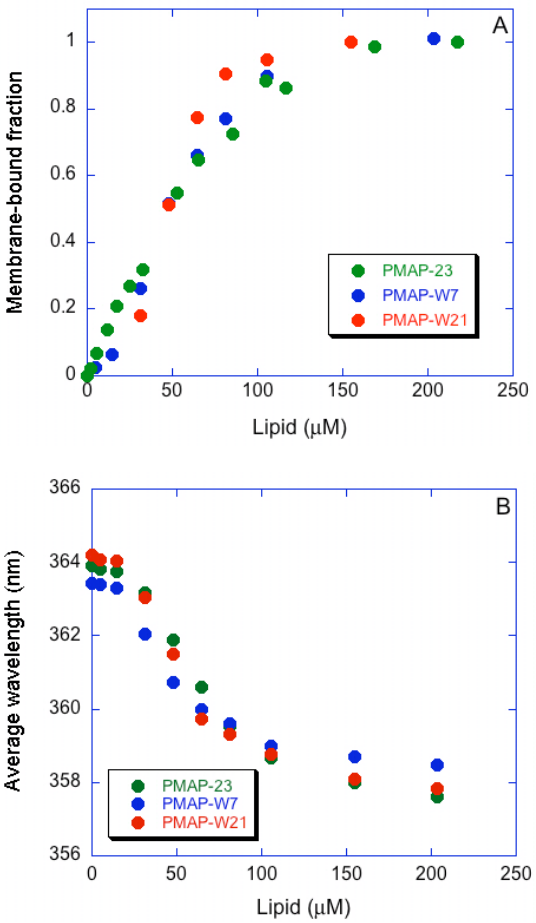

Figure 3.7. Water-membrane partition. Liposome composition ePC/ePG 2:1 (mol/mol). Peptide concentration 10 μM. Panel A: Fraction of membrane-bound peptide as a function of lipid concentration of PMAP-23, W7, and W21. λ_{exc} = 280 nm and λ_{em} = 355 nm. Panel B: Variation in the average wavelength of the emission spectra of the three analogues caused by membrane binding.

The Trp emission spectral shift was quantified by calculating the average wavelength values, as shown in Equation E3.2.

$$<\lambda>=\frac{\int \lambda F(\lambda) d\lambda}{\int F(\lambda) d\lambda} \qquad \text{(E3.2)}$$

where the integral was extended from 320 to 420 nm. As shown in Figure 3.7B, the blue shift caused by membrane association was similar for the two PMAP-23 analogues which contain a single Trp located at two different positions along the primary sequence, as well as for the natural peptide. This indicates that the two Trp residues of PMAP-23 sense a similar environment. Since Trp emission is strongly dependent on its insertion depth inside a membrane [Voges *et al*., 1987 and de Foresta *et al*., 2002], this finding suggests a similar location of the two residues in the bilayer, and therefore a peptide orientation essentially parallel to the membrane plane.

It is interesting to compare the membrane-association curve obtained for PMAP-23 with that previously reported for the fluorescent trichogin GA IV analogue F10, at a comparable peptide concentration (Figure 3.8, taken from [Gatto *et al.*, 2006]). In this case, a much higher lipid concentration was needed to attain complete membrane binding, as a consequence of the lack of any electrostatic driving force, and of the competition with peptide aggregation in water [Stella *et al.*, 2004].

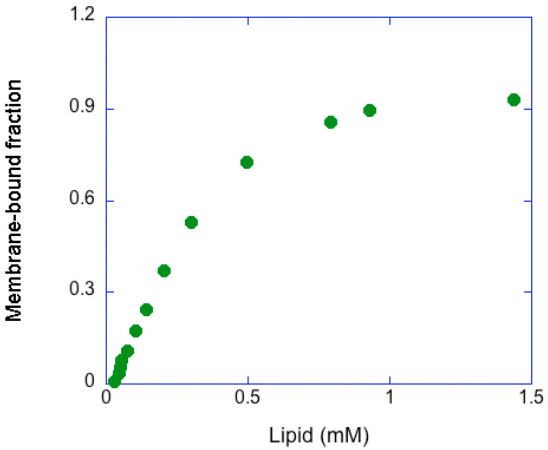

Figure 3.8. Fraction of membrane-bound peptide as a function of lipid concentration. [F10]=11 μM. Liposome composition ePC/Cholesterol 1:1 (mol/mol). λ_{exc}=280 nm and λ_{em}=340 nm [Gatto *et al.*, 2006].

3.3.2. Peptide-induced liposome leakage

To determinate the activity of PMAP-23 and its analogues, peptide-induced membrane leakage was measured, by using liposomes as a model system, and taking advantage of the self-quenching properties of the fluorescent tracer 5,6-carboxyfluorescein (CF).

CARBOXYFLUORESCEIN SELF-QUENCHING

Carboxyfluorescein, when present at high concentrations, forms nonfluorescent dimers which strongly reduce its quantum yield. Further self-quenching is due to nonradiative energy-transfer from fluorescent monomers to nonfluorescent dimers [Weinstein *et al.*, 1981].

In order to characterize this self-quenching behavior inside liposomes, the self-quenching efficiency was determined in vesicles containing the dye at different concentrations (5 to 30 mM), by measuring the fluorescence intensity of the probe before (*F*) and after the addition of detergent Triton X-100 (F_0), which causes the rupture of liposomes, the total leakage of CF, the dye dilution in the outer solution, and elimination of aggregation and self-quenching. The self-quenching efficiency *E* was calculated according to Equation E3.3.

$$E = 1 - \frac{F}{F_0} \qquad \text{(E3.3)}$$

The concentration-dependence of the self-quenching efficiency (Figure 3.9) was satisfactorily described by a phenomenological Hill sigmoidal curve defined by the Equation E3.4.

$$E = \frac{(KC)^n}{1+(KC)^n} = \frac{1}{1+(KC)^{-n}} \qquad \text{(E3.4)}$$

with n=1.5 and K=76.2 M^{-1}, in agreement with previous reports on similar systems [Weinstein *et al*., 1981; Schwarz and Arbuzova, 1995 and Chen and Knutson, 1988]. Incidentally, the measured self-quenching didn't depend on the liposomes' concentration used in this experiment, as shown in Figure 3.9. A quenching efficiency higher than

75% was observed at 30 mM CF. For this reason, the vesicle leakage experiments were performed at this concentration.

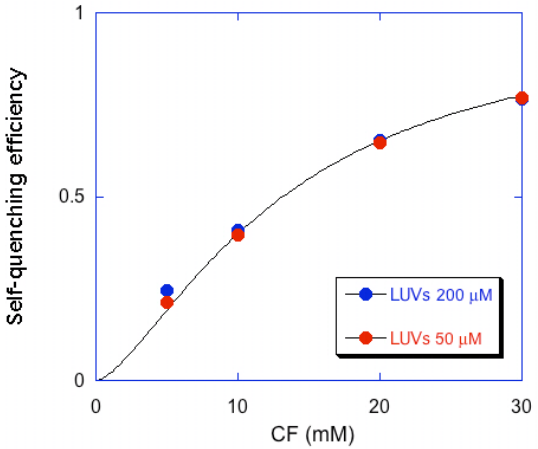

Figure 3.9. Concentration dependence of self-quenching efficiency for CF entrapped inside ePC/ePG vesicles.

PEPTIDE-INDUCED LEAKAGE FROM LIPOSOMES

In order to determine the peptide membrane-perturbing activity, vesicles containing 30 mM CF were employed. When the peptide forms pores in the vesicles, the dye is released and the fluorescence signal increases due to CF dilution in the outer solution and dequenching. The fraction of fluorophore released, *f*, was calculated by determining the fluorescence intensity measured after complete vesicle micellization by a detergent (Triton X-100, 1 mM), as shown in Equation E3.5.

$$f = \frac{F - F_0}{F_\infty - F_0} \qquad \text{(E3.5)}$$

F_0 and F_∞ are the fluorescence intensities before peptide addition and after detergent addition, respectively, while F is the intensity measured at a given time after peptide addition.

Figure 3.10A shows some carboxyfluorescein release curves, measured at different PMAP-23 concentrations. In Figure 3.10B, the fraction of CF contents of liposomes released 20 minutes after peptide addition is shown as a function of peptide concentration for PMAP-23 and its analogues.

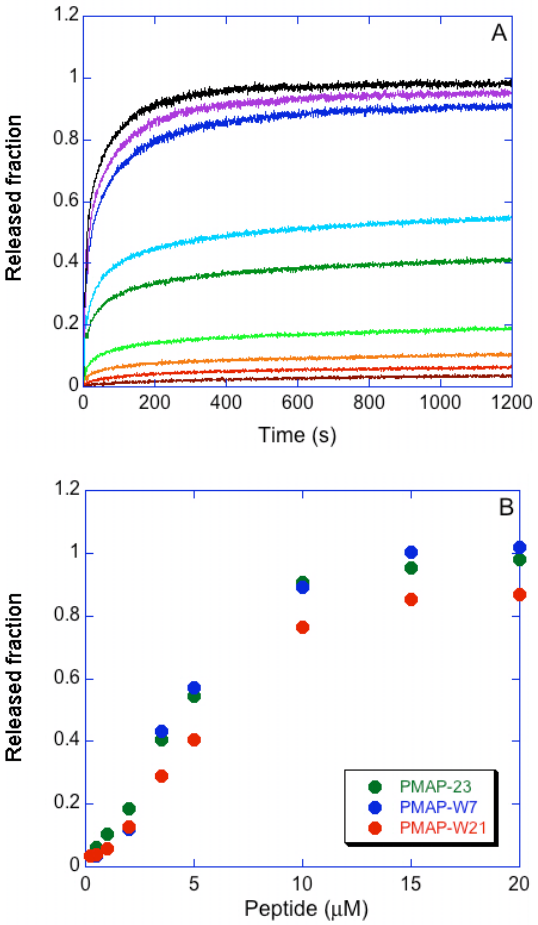

Figure 3.10. Vesicle leakage induced by PMAP-23 and its analogues. Panel A: kinetics of carboxyfluorescein release after addition of PMAP-23. [PMAP-23]=0.2, 0.5, 1, 2, 3.5, 5, 10, 15, 20 μM from bottom to top. Panel B: fractional release of liposome-entrapped carboxyfluorescein, 20 minutes after addition of peptides to vesicles, as a function of peptide concentration. [Lipid]=0.2 mM.

Both single tryptophan PMAP-23 analogues exhibited a membrane-perturbing activity comparable to the natural peptide, in

agreement with the findings showing that their antimicrobial activity on several different bacterial strains is comparable [Yang *et al*., 2006]. Therefore, this experiment indicates that the two analogues PMAP-W7 and PMAP-W21 can be considered as reliable models of the behavior of PMAP-23.

The plot of the released fraction as a function of peptide concentration does not exhibit any cooperativity, suggesting that peptide aggregates are not involved in the pore formation process.

It is interesting to compare these findings with the published reports regarding trichogin GA IV. Figure 3.11A (adapted from [Stella *et al.*, 2004]) shows the release fraction induced by the fluorescent trichogin GA IV analogue F10, as a function of peptide concentration. In this case, a strong sigmoidicity was observed, suggesting that peptide aggregates are involved in membrane permeabilization. Indeed, time-resolved experiments demonstrated the formation of aggregates in the membrane phase [Stella *et al*., 2004], and the leakage rate was strongly correlated with the concentration of these aggregates (Figure 3.11B), confirming that the aggregated peptides are the pore-forming species.

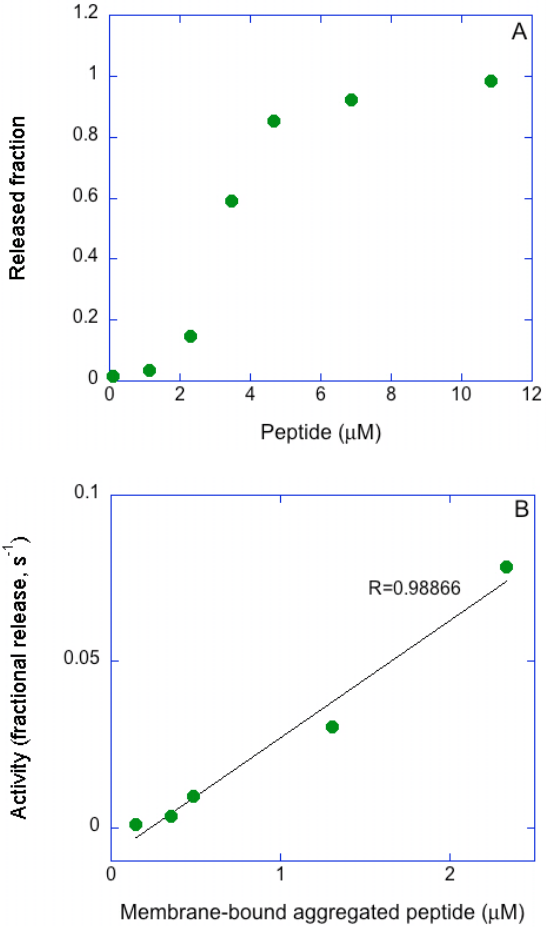

Figure 3.11. Vesicle leakage induced by trichogin GA IV fluorescent analogue F10. Panel A: fractional release of liposome-entrapped carboxyfluorescein 20 minutes after addition of F10 to vesicles. Panel B: initial rate of CF release, as a function of the concentration of membrane-bound peptide aggregates. [Lipid]=0.2 mM. (adapted from [Stella *et al.*, 2004 and Mazzuca *et al.*, 2005])

LEAKAGE MECHANISM

An important question regarding the leakage mechanism is whether it takes place as an “all-or-none” or as a graded process (Figure 3.12). In the first case only completely full and completely empty vesicles are present in the sample at a given time during the leakage kinetics, since the time needed for the leakage of liposome contents is shorter than the lifetime of peptide-induced pores. By contrast, in the case of a graded leakage, partially emptied vesicles are present [Ladokhin *et al*., 1997]. The two possibilities can be discriminated by measuring the carboxyfluorescein quenching efficiency after partial peptide-induced leakage [Weinstein *et al*., 1981 and Schwarz and Arbuzova, 1995]. In the case of an all-or-none mechanism, at any time during the leakage process each vesicle is either completely empty or it contains the same CF concentration originally entrapped inside the liposomes. Therefore, the self-quenching efficiency of entrapped CF is always the same. On the other hand, in a graded process, the CF concentration inside the liposomes decreases during the leakage, causing a decrease in the self-quenching efficiency of entrapped CF [Weinstein *et al.,* 1981].

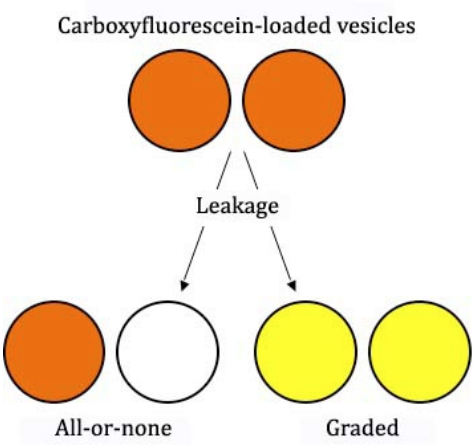

Figure 3.12. Schematic representation of possible release mechanisms. Filled vesicles (orange), partially emptied (yellow) and completely empty (white).

CF-containing liposomes were incubated with PMAP-23 at different concentrations, in order to obtain various levels of partial leakage. The leakage process was stopped by digesting the peptide with trypsin, which was able to immediately stop the leakage process (Figure 3.13). The released CF was separated from the vesicles by gel permeation chromatography, and the self-quenching efficiency of the CF still entrapped inside vesicles was determined. The resulting data are reported in Figure 3.14, and clearly demonstrate that the PMAP-23-induced leakage follows an ”all or none” mechanism. For comparison, the quenching efficiency expected after partial leakage in a graded mechanism is reported in the same Figure. This efficiency was calculated by employing the phenomenological relation describing the concentration dependence of CF self-quenching (Equation E3.4), and by

considering that the concentration inside vesicles after partial leakage of a fraction *x* is *1-x* of the initial concentration C_0 (Equation E3.6).

$$E(x) = \frac{1}{1 + \left[KC_0 (1 - x) \right]^{-n}} \qquad \text{(E3.6)}$$

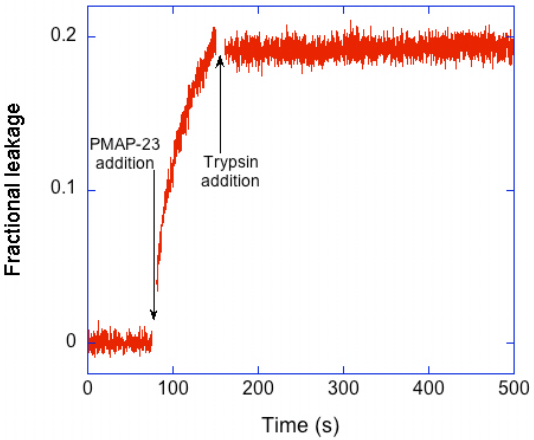

Figure 3.13. Carboxyfluorescein release induced by PMAP-23 addition (first arrow) and stopped by trypsin (second arrow) that digests and deactivates the peptide. [PMAP-23]=20 μM, [Lipid]=0.2 mM, [trypsin]=2 μM.

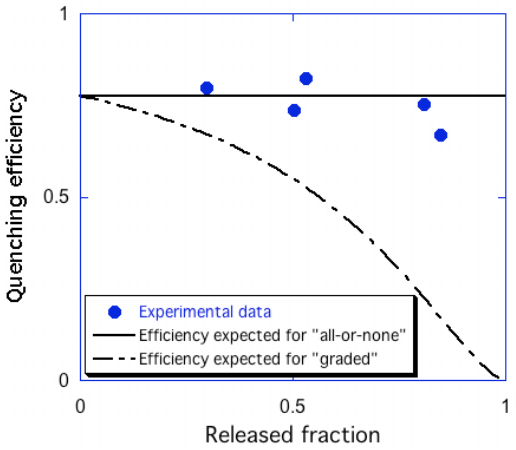

Figure 3.14. CF self-quenching efficiency after partial PMAP-23 induced leakage.

RELEASE FROM GIANT UNILAMELLAR VESICLES

The peptide-induced leakage process could be visualized directly by using giant unilamellar vesicles (GUVs). These liposomes have a diameter in the micrometers range, and therefore can be visualized by optical microscopy.

A fluorescent probe was inserted in the membrane by adding a small quantity of rhodamine-labeled phospholipids to the lipid mixture employed in GUV preparation. The internal aqueous volume was made visible by entrapping a CF solution at a 3 μM concentration, in order to minimize self-quenching. The GUV content and the lipid membrane, before and after peptide addition, could be observed independently by imaging the green CF fluorescence and the red rhodamine emission.

The fluorescence emission of CF was measured at different times after peptide addition, showing that PMAP-23 was able to cause the

leakage of vesicle contents, as indicated by the disappearance of CF emission caused by its diffusion in the extravesicular volume, in a few minutes (Figure 3.15A). However, no observable changes took place in the membrane, that remained intact even after complete release of the GUV contents, indicating that PMAP-23 caused membrane leakage by forming pores rather than by causing membrane micellization (Figure 3.15B).

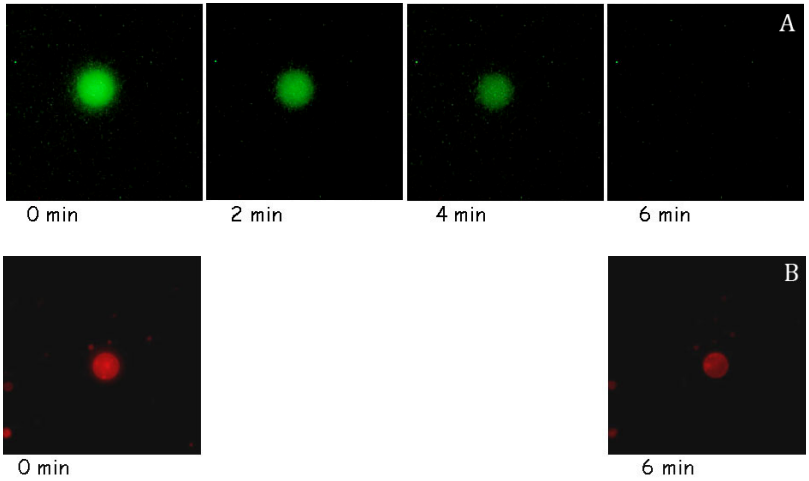

Figure 3.15. Fluorescence microscopy images of leakage from a GUV, induced by PMAP-23 (5 μM). Panel A: fluorescence emission from carboxyfluorescein molecules entrapped inside the GUV, at different times after peptide addition. Panel B: fluorescence emission from rhodamine-labeled phospholipids located in the GUV bilayer. The vesicle diameter is about 20 μm (20x magnifying objective).

The gradual CF release shown in Figure 3.15 might appear in contrast to the "all or none" leakage observed with LUVs. However, the distinction between a graded or "all or none" mechanism is simply

based on the comparison between the lifetime of an open pore (τ_P), and the time needed to completely empty a single vesicle (τ_V). The leakage is "all or none" if $\tau_P >> \tau_V$, otherwise it is graded. Since the time to empty a vesicle through a single pore depends on its volume, τ_V is about 10^7 times longer for GUVs than for LUVs, explaining the apparently contradictory observations.

3.3.3. Depth-dependent quenching

A more precise determination of peptide location in the membrane could be obtained by depth-dependent quenching experiments [Ladokhin, 1999a].

These experiments were performed by measuring the decrease in tryptophan fluorescence caused by association to membranes containing phospholipids labeled with a nitroxide group at different positions along the acyl chain of the lipids.

Nitroxide is a short-range quencher of Trp emission [Lakowicz, 2006d], and therefore quenching is maximal when the depth of the fluorophore and of the quencher inside the membrane coincide. Since the position of the quenchers inside the membrane has been measured independently [Chung *et al.,* 1992], these measurements allow a determination of fluorophore depth in the bilayer. In order to determine both the depth of peptide penetration in the membrane and helix orientation, quenching experiments were performed with the two single-Trp PMAP-23 analogues PMAP-W7 and PMAP-W21.

Figure 3.16, reports fluorescence quenching values as a function of quencher depth. The quenching profile is defined as

$$Q = \ln \frac{F_0}{F} \qquad \text{(E3.7)}$$

where F_0 is the fluorescence intensity of peptides associated to unlabeled liposomes, and F is the emission intensity of the peptide bound to vesicles containing doxyl-labeled lipids.

In the experiment performed at 1 μM peptide concentration (a concentration which induces only minimal vesicle leakage) the quenching curves for both single-fluorophore analogues show a maximum slightly below 1 nm from the bilayer center. This position corresponds approximately to the interface between the polar headgroups region and the hydrophobic core of the bilayer [Orioni *et al*., 2009]. The depth of insertion and orientation observed here for PMAP-23 are similar to those of other AMPs of the same family, such as LL-37 [Henzler Wildman *et al*., 2003 and Henzler Wildman *et al*., 2004]. The similar result obtained for the two single-Trp analogues confirms a peptide orientation parallel to the membrane surface. With increasing peptide concentration (Figure 3.16B) both curves become less dependent on quencher position, but the quenching profile, for PMAP-W21 still shows that the position of Trp21 is unchanged with increasing peptide concentration.

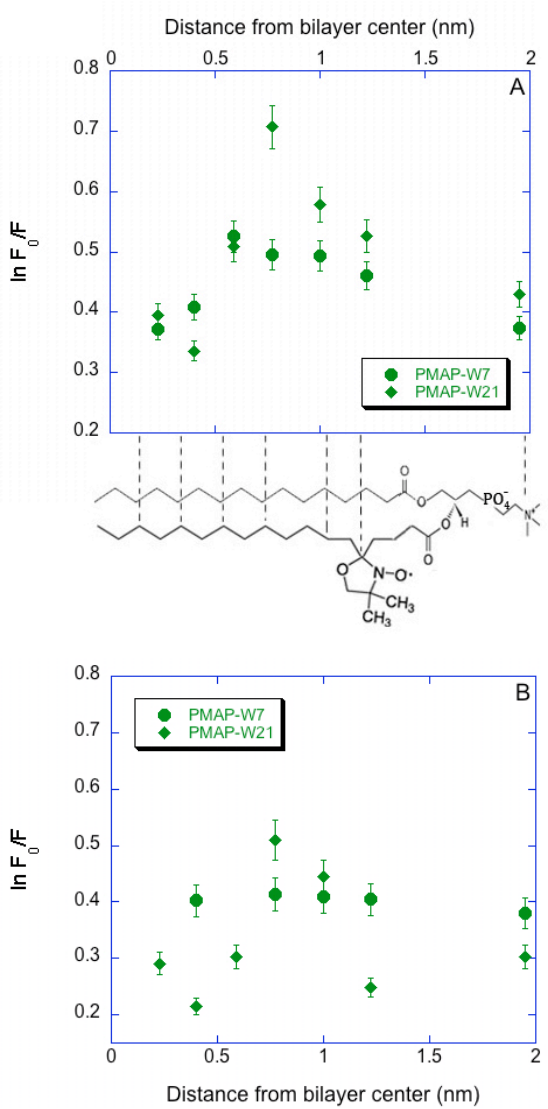

Figure 3.16. Depth-dependent quenching experiments for PMAP-23 analogues. Peptide concentration 1 μM (panel A) and 10 μM (panel B). [lipid]=0.2 mM.

Surprisingly, the quenching profiles for the PMAP-23 analogues were rather wide and ill defined, as compared to similar experiments performed on other peptides [Mazzuca *et al*., 2005; Gatto *et al*., 2006; Ladokhin 1997; Voges *et al.,* 1987; Ladokhin, 1999b and Glukhov *et al.,* 2005], particularly in the case of Trp7, and at high peptide concentrations (10 μM). For comparison, Figure 3.17 shows depth dependent quenching experiments performed on trichogin GA IV analogue F10 at different concentrations [Gatto *et al*., 2006].

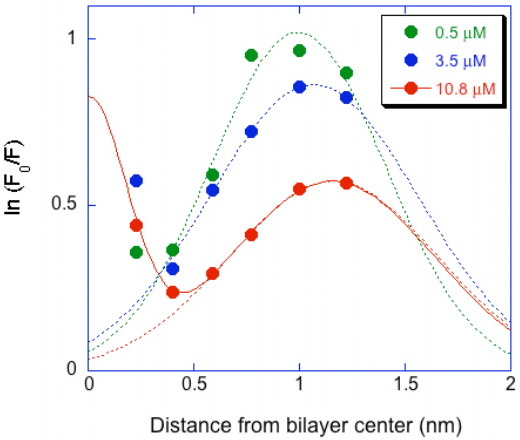

Figure 3.17. Depth-dependent quenching experiments for trichogin GA IV fluorescent analogue F10, at different peptide concentrations. The data were fitted with a single or double Gaussian distribution, the data at higher peptide concentration are fitted also by a double gaussian. [Lipid]=0.2 mM. [Gatto *et al.*, 2006].

Several differences can be observed in comparison to PMAP-23: the quenching profiles are well defined, and a change in position with increasing peptide concentration is observed. At low peptide/lipid ratios (when the peptide does not induce leakage) trichogin is located

close to the polar headgroups region (i.e. at a depth similar to that observed for PMAP-23). However, by increasing peptide concentration to leakage-inducing values, a transition takes place and a significant fraction of the peptide becomes deeply buried into the bilayer. It has been shown that this change in peptide depth is strictly coupled with peptide aggregation [Mazzuca *et al.,* 2005]and that therefore two states only are populated by trichogin in the membrane: i), a monomeric, surface bound, and inactive form and ii), a buried, aggregated state, responsible for membrane leakage.

In order to interpret the ill defined depth-dependent quenching observed for PMAP-23, it is important to consider that the observed quenching profile results from the convolution of the distribution of depths populated both by the fluorophore and by the quencher [Ladokhin, 1997]. Therefore, the broad quenching profile observed for PMAP-23 could be attributed to two possible causes: the peptide might sample a wide distribution of depths inside the bilayer [Stella *et al*., 2007], or, alternatively, peptide binding could induce local disorder in the phospholipids, increasing the width of the depth distribution sampled by the quenching moieties. These two options will be further explored in the sections 3.3.7 and 3.3.9.

3.3.4. Peptide-induced lipid flip-flop

The molecules of a lipid membrane are free to move laterally along the plane of the double layer. In addition to lateral motions, the transition

from one layer to the other is also possible. This movement, called "flip-flop", is strictly limited by the difficulty of transferring the hydrophilic head through the hydrophobic region. Indeed, flip-flop occurs much more slowly than the lateral diffusion [Matsuzaki *et al*., 1996]. In the absence of external perturbations, the rate of spontaneous translocation of lipids across the bilayer (lipid flip-flop) is so low that several days are needed until an initially asymmetric membrane attains a homogeneous lipid distribution in both layers [Matsuzaki *et al*., 1996]. However, many membrane-perturbing agents, including some antimicrobial peptides [Mazzuca *et al*., 2005], cause a huge enhancement of this rate, so that the flip-flop process can be completed even in a few minutes [Matsuzaki *et al*., 1996].

In order to check whether PMAP-23 induced lipid translocation across the two leaflets of the membrane, vesicles labeled with the fluorescent lipid C6-NBD-PC (1-palmitoyl-2-[6-((7-nitrobenz-2-oxa-1,3-diazol-4-yl)amino)caproyl]-L-α-phosphatidylcholine) only in the inner leaflet of the membrane were employed.

Inner-labeled liposomes were prepared from double-labeled vesicles after reduction of NBD groups by sodium dithionite. This reagent is able to reduce the NBD group to ABD (7-amino-2,1,3-benzodiazol-4yl), which is not fluorescent [McIntyre and Sleight, 1991]. The kinetics of reduction after dithionite was added to vesicles symmetrically labeled with NBD is reported in Figure 3.18: the fast phase corresponds to reduction of probe molecules exposed to the external aqueous phase, while the much slower decay in fluorescence intensity is due to slow dithionite diffusion through the membrane, and

reduction of internal NBD. This second phase was stopped by removing dithionite by gel permeation chromatography.

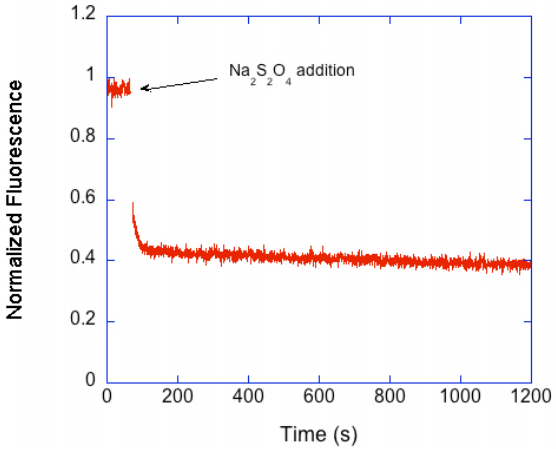

Figure 3.18. Kinetics of reduction of symmetrically NBD-labeled liposomes by dithionite.

The amount of internal and external probes can thus be quantified by a double exponential fit of the kinetics, according to Equation E3.8.

$$y = ae^{-t/b} + (1-a)e^{-t/c} \qquad \text{(E3.8)}$$

where *a* is the fraction associated to the fast decay time *b*, while *c* is the slow decay time. Surprisingly, these data show that in symmetrically labeled vesicles approximately 60% of NBD was in the outer layer (while this fraction should be close to 50%). This was probably due to

the high labeling ratio. Molecular crowding effects likely favored the external layer as compared to the internal layer, due to the opposite curvature of the two leaflets.

The inner labeled liposomes obtained by dithionite reduction were incubated with different concentrations of PMAP-23 to cause lipid flip-flop. The peptide was then digested by trypsin addition, and the fraction of labeled lipids translocated to the external layer was determined by measuring their fluorescence quenching by the reducing agent. The trypsin addition was important because, by digesting the peptide, in addition to stopping peptide-induced flip-flop it also removed peptide-induced membrane pores, so that dithionite couldn't enter into the vesicles and reduce inner NBD.

Figure 3.19 shows the evolution of the reaction after an incubation of 20 minutes with different concentrations of PMAP-23.

The fraction of translocated lipids was calculated by fitting the fluorescence curves with Equation E3.8 [Matsuzaki *et al.,* 1996], to determine the fraction of external labeled lipids. A significant peptide-induced lipid flip-flop was observed (Figure 3.20, blue circles). Interestingly, this phenomenon exhibited a dependence on peptide concentration very similar to that observed in the leakage curves (Figure 3.20), suggesting that the two phenomena are coupled.

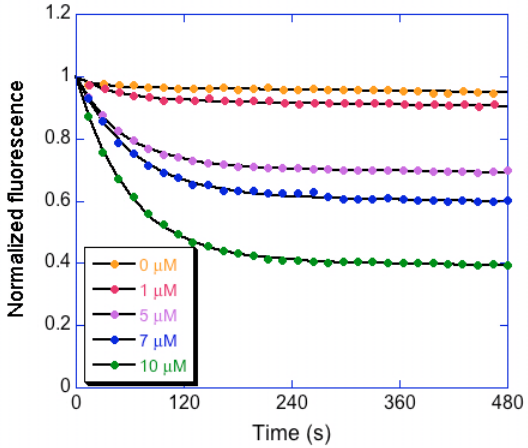

Figure 3.19. Kinetics of reduction by dithionite after peptide-induced lipid translocation (20 minutes incubation). Continuous lines are the best fits to the data according to Equation E3.8. [Lipid]=0.2 mM.

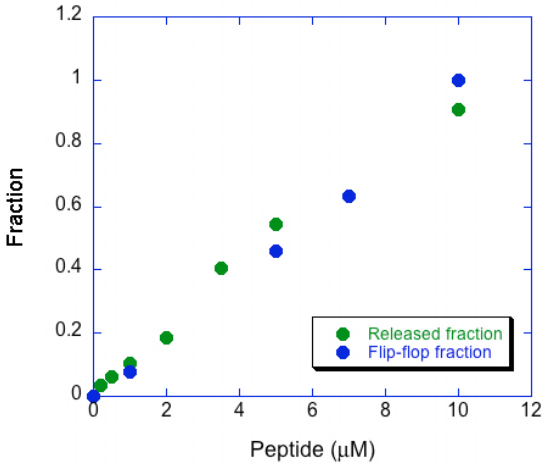

Figure 3.20. Fraction of PMAP-23 induced CF leakage and lipid flip-flop, 20 minutes after peptide addition. [Lipid]=0.2 mM.

Also in the case of trichogin, lipid flip-flop occurs, but it is not strictly correlated to the leakage process (Figure 3.21). It is important

to note that both peptides acting according to the barrel stave model, such as alamethicin [Fattal *et al.,* 1994], and peptides acting with the carpet mechanism, such as magainin [Matsuzaki *et al.,* 1995a and Matsuzaki *et al.,* 1995b], induce significant lipid flip-flop. The only difference is that in the Shai-Matsuzaki-Huang model membrane leakage and lipid translocation are strongly coupled.

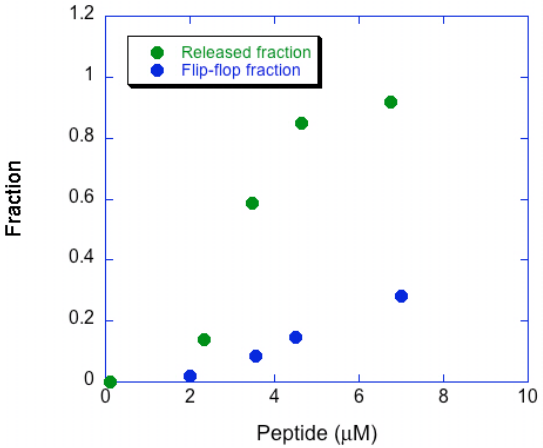

Figure 3.21. Fraction of F10 induced CF leakage and lipid flip-flop, 20 minutes after peptide addition. [Lipid]=0.2 mM.

3.3.5. Peptide exchange between vesicles

Fluorescence Resonance Energy Transfer (FRET) is an important process that occurs in the excited state when emission spectrum of a fluorophore, called donor, overlaps with the absorption spectrum of another molecule, called acceptor. FRET doesn't involve emission of

light by the donor, since energy-transfer occurs nonraditively by a resonant phenomenon caused by dipole-dipole interactions [Lakowicz, 2006e]. The FRET efficiency is dependent on the inverse sixth power of the intermolecular separation, making it useful over distances comparable with the dimensions of biological macromolecules. Thus, FRET is an important technique for investigating a variety of biological phenomena that produce changes in molecular proximity.

FRET was exploited to assess the ability of PMAP-23 to exchange between different vesicles. The peptide was added to vesicles labeled with the fluorescent lipid N-NBD-PE (1,2-Dioleoyl-sn-Glycero-3-phosphoethanolamine-N-(7-nitro-2-1,3benzoxadiazol-4-yl), which can act as a FRET acceptor for the intrinsic tryptophan fluorescence of the peptide.

Peptide and lipid concentrations (5 μM and 200 μM, respectively) were chosen to ensure complete peptide association to the vesicles. After equilibration of the system, an excess of unlabeled vesicles (final concentration 800 μM) was added to the sample. A spectral change was observed, which was completed within the few seconds needed for mixing and acquisition: Trp fluorescence increased and NBD emission decreased (Figure 3.22), indicating a reduced FRET efficiency caused by peptide exchange between acceptor-labeled and unlabeled vesicles. A similar fast peptide exchange among vesicles has been reported also in the case of trichogin [Mazzuca, 2005].

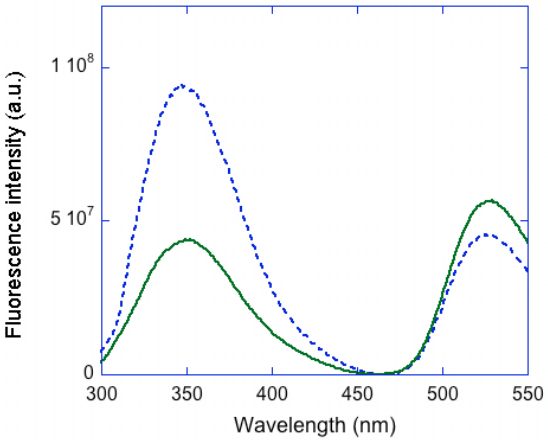

Figure 3.22. PMAP-23 exchange among vesicles, as determined by FRET: the continuous curve represents the emission spectrum (λ_{exc} 280 nm) of a sample in which the peptide (5 μM) was added to ePC/ePG vesicles labeled with C_6-NBD-PC ([lipid]=0.2 mM). The broken line is the spectrum of the same sample immediately after addition of an excess of unlabeled vesicles ([lipid]=0.8 mM).

3.3.6. Peptide translocation across the bilayer

A FRET assay [Mazzuca *et al.,* 2005] was employed to determine whether the peptide, when added to a vesicle suspension, would remain associated to the outer layer of the liposomes or translocate across the membrane to become distributed in the whole bilayer. An energy-transfer acceptor for peptide fluorescence was introduced in the liposomes as a fluorescent lipid (C6-NBD-PC). Two different types of vesicles were prepared: outer layer labeled liposomes (OL), where the fluorescent probe was incorporated only in the outer layer by adding it to a vesicle suspension after liposome formation and inner layer labeled

liposomes (IL), obtained by chemically quenching the label in the outer layer of liposomes homogeneously labeled in both layers (see “Peptide-induced lipid flip-flop” paragraph).

In the case of the Trp-NBD pair, the Förster distance, which defines the range of FRET efficiency, is 26 Å [Loura *et al.,* 2003], whereas the thickness of the bilayer is approximately 40 Å [Lis *et al.,* 1982]. Since the fluorophore of C6-NBD-PC is located in the region of the polar headgroups [Wolf *et al*., 1982; Abrams and London, 1993 and Mazeres *et al.,* 1996], a peptide lying in the outer layer or a peptide distributed in the whole bilayer will be quenched quite differently. Therefore, the FRET efficiency allowed us to determine whether the peptide, added to the solution of liposomes, remains on outer layer or is able to translocate also to the inner leaflet.

The FRET efficiency was determined both by the decrease in Trp emission and by the increase in NBD fluorescence. Both datasets show that In the case of PMAP-23 a significant energy transfer takes place only with OL liposomes (Figure 3.23), indicating that the peptide did not translocate across the membrane, at least at the concentration investigated.

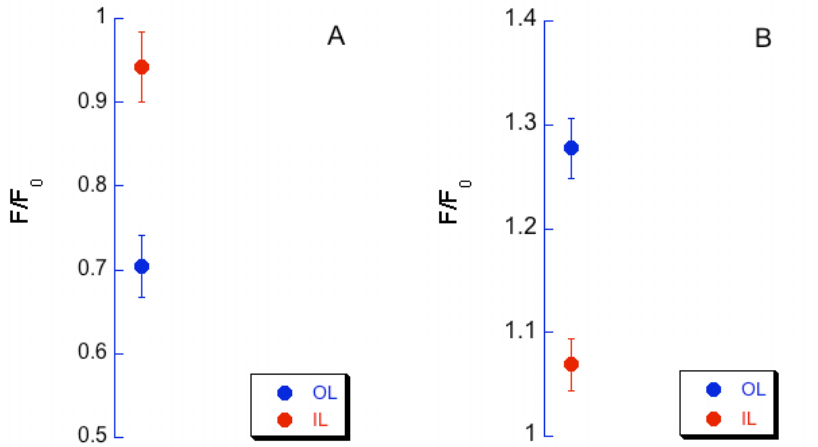

Figure 3.23. PMAP-23 translocation. A: decrease in PMAP-23 fluorescence (*F*) when associated to liposomes containing NBD-labeled lipids in the outer or in the inner leaflet of the membrane, with respect to the fluorescence of PMAP-23 associated to unlabeled vesicles (F_0). B: increase in NBD fluorescence (*F*) when the peptide was added to liposomes containing the fluorescent lipid in the outer or inner leaflet of the membrane, with respect to the fluorescence measured in the absence of PMAP-23 (F_0). Data referring to outer layer labeled liposomes are represented by blue symbols, while those referring to inner layer labeled liposomes are shown as red symbol. [PMAP-23]=1 μM and [Lipid]=0.2 mM.

It is important to note that this assay could only be performed under conditions in which lipid asymmetry was conserved, and lipid flip-flop was negligible during the assay time. For this reason, the experiment could only be performed at 1 μM PMAP-23 concentration, at which the peptide does not cause significant vesicle leakage, as shown in section 3.3.2. At the end of the experiments of peptide translocation, the conservation of the asymmetric membrane labeling was assessed. In fact, if the lipids were able to move from one side of the double layer, the method of energy transfer would not be indicative of the translocation of the peptide. The graph in Figure 3.24 shows the

kinetics of the NBD reduction with sodium dithionite on internal (IL) and external (OL) labeled-liposomes after incubation with PMAP-23. The reaction confirmed the absence of lipid flip-flop.

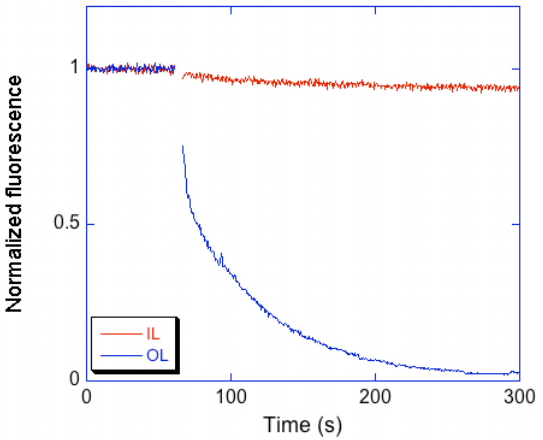

Figure 3.24. Kinetic curves of NBD reduction by sodium dithionite, after incubation with 1μM PMAP-23. Lipid concentration 0.2 mM.

Interestingly a completely different peptide-translocation behavior has been reported for trichogin GA IV (Figure 3.25, [Mazzuca *et al.*, 2005]).

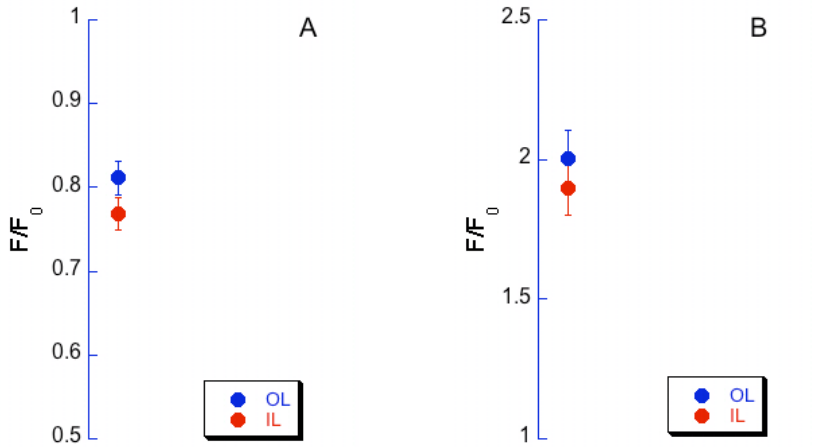

Figure 3.25. F10 translocation (see the legend to Figure 3.24). [F10] = 0.5 μM; [lipid]= 0.2 mM. [Mazzuca *et al.*, 2005].

At concentration below its activity threshold, PMAP-23 remains associated to the outer layer and doesn't translocate to the membrane interior. By contrast, trichogin GA IV analogue F10 distributes in both layers, even at concentrations so low that it is not active. Probably, the higher hydrophobicity of trichogin makes a membrane inserted state less unfavorable, even at low concentrations, when peptide-induced pores do not form.

3.3.7. Peptide effects on membrane dynamics

Phospholipid bilayers exhibit a thermotropic phase transition from a "gel" phase, in which the lipid acyl chain are mostly in an all-trans conformation, and the hydrophobic core of the membrane is very

viscous, to a “liquid crystal” phase, in which the lipid chains are much more disordered, dynamic and fluid. The transition temperature T_m depends on the phospholipids properties, such as chain length and number and position of unsaturated bonds.

In order to study peptide effects on membrane dynamics, experiments were performed on dimyristoyl phospholipids, whose phase transition is at about 25 °C. Therefore, by varying the system temperature from 10 to 40 °C membrane behavior in both phases could be investigated. DMPC/DMPG (2:1 mol/mol) vesicles were employed for PMAP-23, while DMPC was used for trichogin GA IV.

1,6 DIPHENYLHEXATRIENE EXPERIMENTS

To verify whether the peptide, when added to a vesicle solution, would cause a change in membrane dynamics, steady-state anisotropy experiments with a membrane-inserted fluorophore (1,6 diphenylhexatriene, DPH) were performed. Because this probe is known to be located deep in the lipid bilayer and to be oriented parallel to the lipid chains, fluorescence anisotropy measurements reflect the probe mobility in the bilayer, and therefore the fluidity of the membrane. Indeed, DPH fluorescence anisotropy was high in the gel phase and decreased in the fluid phase (Figure 3.26). The addition of PMAP-23 clearly perturbed membrane dynamics in both phases, leading to a broadening of the phase transition. The PMAP-23 effects on lipid order might be the origin of the ill-defined depth-dependent quenching profiles observed for this peptide (Section 3.3.3).

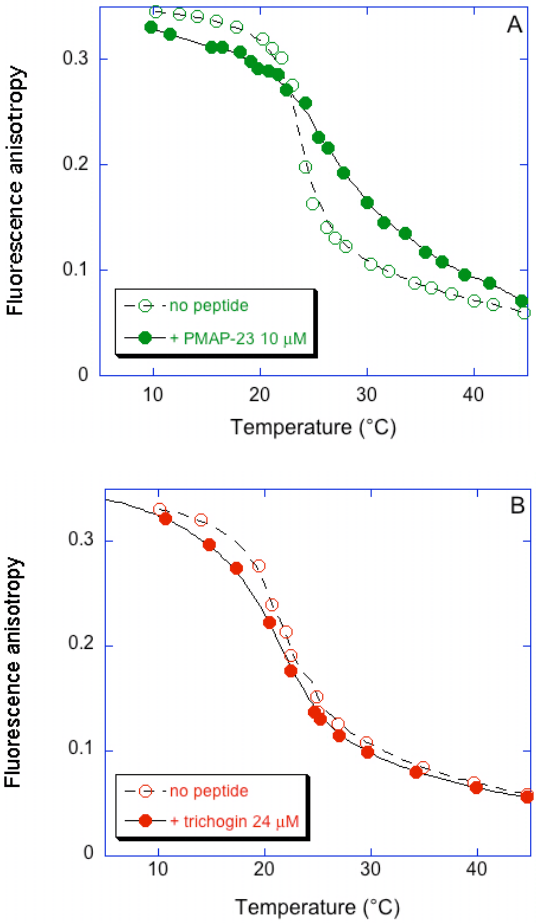

Figure 3.26. Effect of peptide–membrane interactions on the thermotropic phase transition of dimyristoyl phospholipid vesicles, as followed by measuring the fluorescence anisotropy of DPH. Panel A: DMPC/DMPG (2:1) vesicles in the absence (empty circles) and in the presence of PMAP-23 (full circles). Panel B: DMPC vesicles in the absence (empty circles) and in the presence of the equipotent trichogin GA IV analogue Tric-OMe (full circles). Lipid concentration 50 µM and 200 µM in plots A and B, respectively.

This perturbation wasn't observed in the case of trichogin GA IV (Figure 3.26B). This is probably a consequence of its smaller size, and of its ability to ''dissolve'' in the medium formed by the lipid acyl chains, thanks to its hydrophobicity [Bocchinfuso *et al*., 2009].

LAURDAN EXPERIMENTS

Peptide effects on membrane order were studied also by measuring the shifts in the emission spectrum of another membrane probe, Laurdan (6-lauroyl-2-dimethylamino naphthalene).

Laurdan shows a membrane phase-dependent emission spectral shift, useful for discriminating between membrane phases. In fact, laurdan emission spectral shape detects changes in the amount of water penetrating in the bilayer, which changes the polarity of the fluorophore's environment. In the gel phase, water permeation is hindered owing to the tightly packed phospholipid moieties, but when the membrane is in the fluid phase, water molecules can penetrate at the level of the bilayer glycerol backbone, where the probe is located, causing a change in the polarity of the fluorophore's environment, and a red-shift in the emission spectrum [Esquembre *et al.,* 2009 and Parasassi *et al*., 1991]. The emission maximum of laurdan displays a red shift from 438 nm, when the membrane is in the gel phase, to 490 nm, in the liquid crystalline phase., as shown in Figure 3.27.

The spectral shift can be summarized in a single parameter, the so-called "General Polarization" (GP), defined in Equation E3.9.

$$GP = \frac{I_{438} - I_{490}}{I_{438} + I_{490}} \qquad \text{(E3.9)}$$

where I_{438} and I_{490} are the fluorescence intensities measured at 438 and 490 nm, respectively.

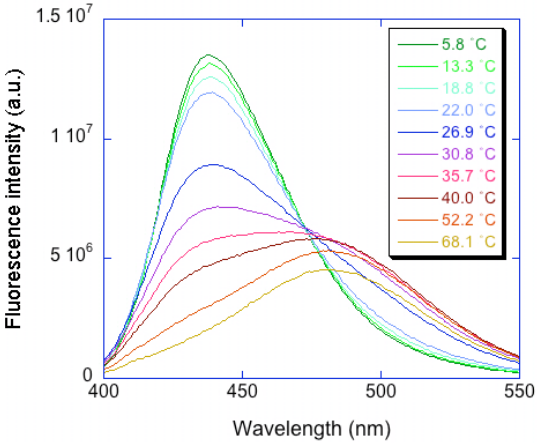

Figure 3.27. Emission spectra of Laurdan 1% mol/mol in DMPC/DMPG 2:1 liposomes ([lipid]=50 μM) at different temperatures (λ_{exc}=360 nm).

The experiment was performed by recording fluorescence spectra of laurdan at different temperatures, in the absence and in the presence of peptide. The results are shown in Figure 3.28. In this case, the sigmoidal curve, corresponding to the phospholipid phase transition, was not affected by PMAP-23, nor by trichogin GA IV. The different effect observed for PMAP-23 with DPH and laurdan could be due to the different depth of the two probes in the membrane, and to

the different properties being measured: PMAP-23 appears to affect the lipid chain order but not the water penetration at the shallow depth at which laurdan is located.

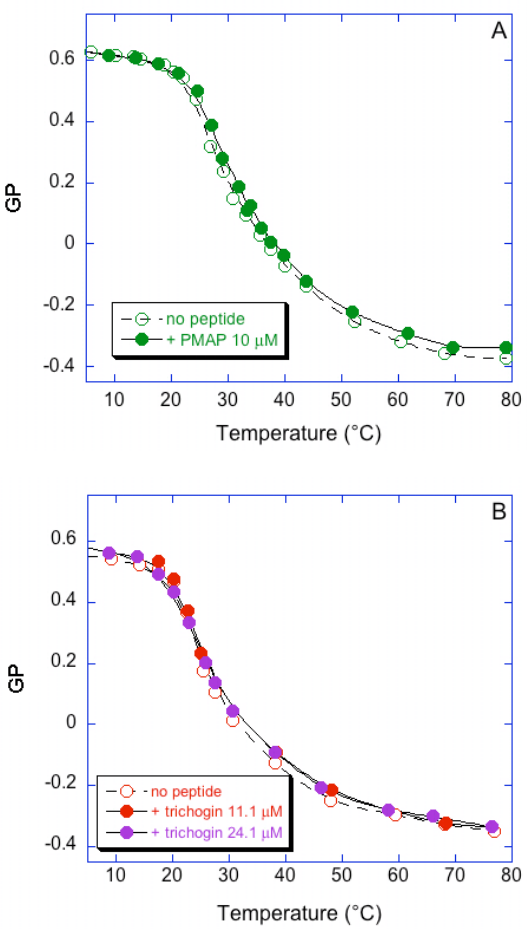

Figure 3.28. Panel A: GP values as a function of temperature for DMPC/DMPG 2:1 liposomes ([lipid]=50 µM) containing 1% molar ratio of Laurdan in the absence (empty circles) and in the presence of PMAP-23 (filled circles). Panel B: GP values as a function of temperature for DMPC liposomes (0.2mM) containing 5% molar ratio of Laurdan, in the absence (empty circles), and in the presence of 11.1 µM (filled red circles) and 24.1 µM (filled purple circles) of Tric-OMe.([lipid]=50 µM) at different temperatures (λ_{exc}=360 nm).

3.3.8. Peptide effects on the membranes: neutron reflectivity experiments

In order to determine the locations of the peptides inside the bilayer and their effect on membrane structure, neutron reflectivity experiments were performed. In the present work, preliminary results obtained at the international ISIS facility (UK) are shown.

The reflectivity of the silicon blocks which were later used to support a lipid bilayer was fully characterized, in the presence of D_2O and cmSi (an H_2O/D_2O mixture matching the refractive index of silicon). The reflectivity profile was acquired again after bilayer deposition, in D_2O buffer and cmSi buffer. A good membrane was obtained with POPC phospholipids.

A small but significant change in the reflectivity profile was observed after addition of trichogin GA IV, and a smaller variation was caused by addition of PMAP-23 (Figure 3.29 and 3.30). However, the reflectivity curves do not allow an unambiguous fitting and the determination of quantitative structural parameters, since different models are compatible with the data.

Further experiments with deuterated lipids and/or peptides are needed to get a clear picture of the systems investigated.

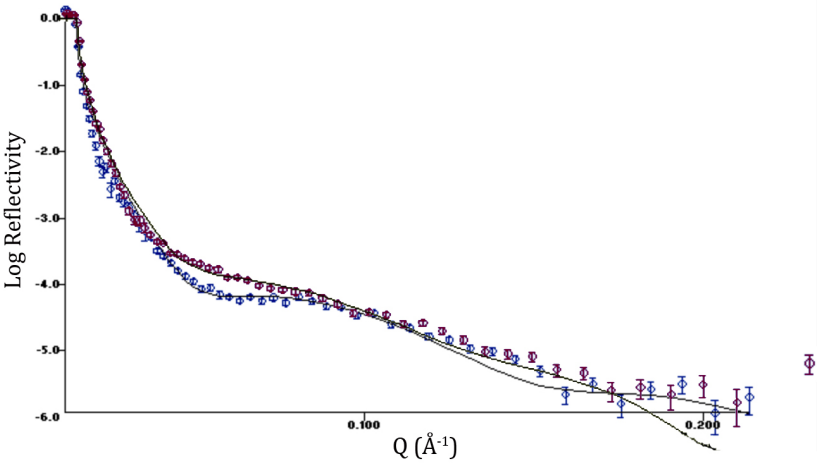

Figure 3.29. Neutron reflectivity profiles in the absence (blue symbols) and in the presence of trichogin GA IV 15 μM (red symbols) in a POPC bilayer in D_2O buffer.

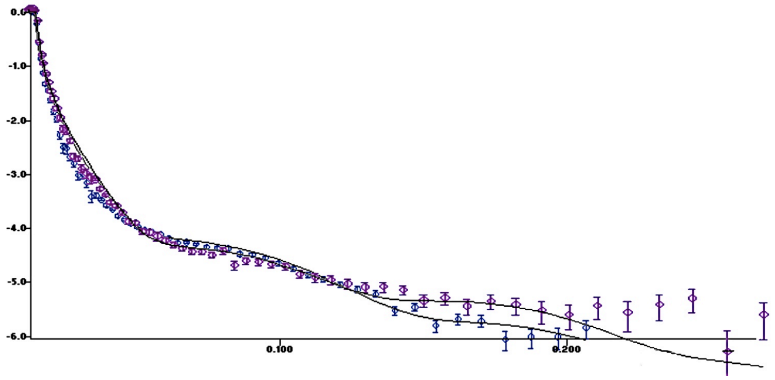

Figure 3.30. Neutron reflectivity profiles in the absence (blue symbols) and in the presence of PMAP-23 5 μM (purple symbols) in a POPC bilayer in D_2O buffer.

3.3.9. Peptide effects on the membranes: Langmuir-Blodgett experiments

Langmuir-Blodgett experiments provide an assessment of the peptide effects on the surface tension of lipid monolayers, i.e. the main mechanism of membrane destabilization according to the carpet model.

A POPC/POPG (2:1, mol/mol) monolayer was spread on a 10 mM phosphate buffer, pH 7.4 subphase, and compressed to a surface pressure of 20 mN/m, to attain a lipid packing comparable to that of lipid bilayers [Schwarz and Taylor, 1999]. This pressure was then maintained stable by a feedback mechanism controlling movable barriers, and the surface area increase caused by peptide association to the monolayer was determined. After each successive addition of PMAP-23 in the subphase, a large increase in the monolayer area was observed(Figure 3.31), confirming that peptide insertion causes a significant lipid perturbation.

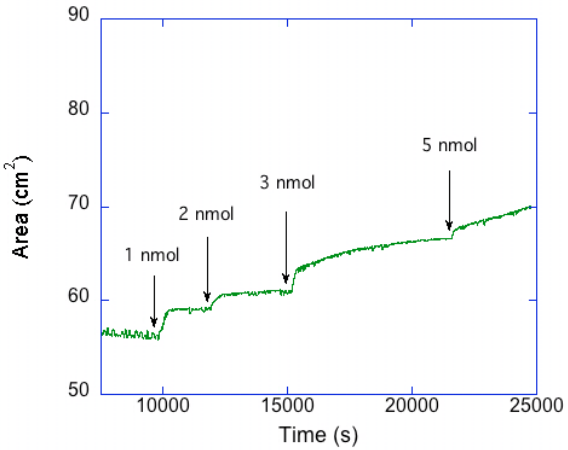

Figure 3.31. Monolayer surface increasing after the addition of different concentrations of PMAP-23 in the subphase. POPC:POPG (2:1) monolayer, 20 mN/m surface pressure.

3.3.10. Influence of membrane curvature

If the peptide acts by causing a difference in surface tension between the two membrane leaflets, its activity must be influenced by the intrinsic curvature of phospholipids forming the membrane [Allende *et al.*, 2005].

The arrangement of phospholipids as symmetrical bilayers results in the formation of a structure that is locally flat. However, the molecular constituents of each monolayer of the bilayer may have an intrinsic curvature that is nonplanar. The shape of the monolayer, when it has attained its most stable curvature, will define the intrinsic curvature. This curvature will be determined by the cross-sectional area occupied at various depths within the relaxed monolayer. For instance,

phosphatidylcholine (PC) phospholipids have an approximately cylindrical shape, because the steric hindrance of their polar head and of their hydrophobic tails is similar. Therefore, these phospholipids do not have any intrinsic curvature and form stable bilayers. Phosphatidylethanolamine (PE) phospholipids, on the other hand, due to their smaller polar head, have a conical shape and a negative intrinsic curvature (Figure 3.32). Finally, peptide insertion in a monolayer, close to the polar heads, causes a positive curvature in the monolayer, and this is the main effect on which the carpet mechanism is based. Therefore, the presence in the membrane of phospholipids with a negative intrinsic curvature is predicted to inhibit peptide activity, if the generation of a positive curvature is the main mechanism of membrane perturbation.

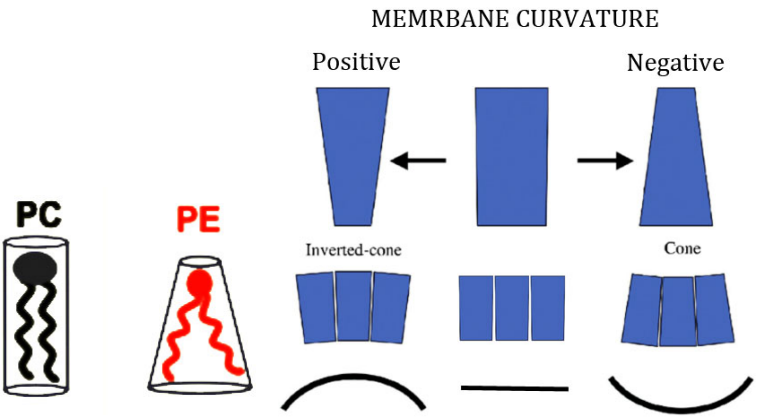

Figure 3.32. Schematic representation of the molecular shape of PC and PE phospholipids, and their effect on the intrinsic curvature of lipid monolayers.

To test if this is the case for PMAP-23, peptide-induced leakage in DOPC/DOPG and in DOPE/DOPG vesicles (2:1 mol/mol) was measured. A significant inhibition of peptide activity in the DOPE containing vesicles was observed (Figure 3.33), confirming the formation of a surface tension strain between the two leaflets of the membrane by PMAP-23.

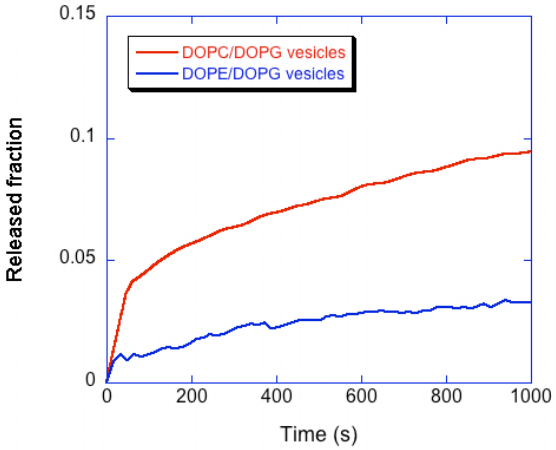

Figure 3.33. Kinetics of CF release after addition of peptide to vesicles of different lipid composition. DOPC/DOPG 2:1 and DOPE/DOPG 2:1. [Lipid]=0.2 mM and [PMAP-23]=0.3 μM.

3.3.11. Molecular dynamics simulations

In order to further characterize peptide position in the bilayer, and its effects on membrane structure and dynamics, molecular dynamics (MD) simulations were recently performed in our group, both for PMAP-23 and trichogin GA IV [Orioni *et al.*, 2009; Bocchinfuso *et al.*,

2009]. It is interesting to compare here the results of these simulations with those of the spectroscopic experiments.

The trajectory lengths, allowed by present day simulation resources, are not sufficient for a complete sampling of all possible peptide arrangements in a membrane bilayer, a relative viscous environment [Matyus *et al*., 2007 and Wee *et al*. 2008]. Therefore, simulations of peptide-membrane systems could be influenced by the starting conditions. Recently, to avoid this problem, a method based on the spontaneous self-assembly of lipid bilayers was proposed [Esteban-Martín and Salgado, 2007 and Carpenter *et al*., 2008]. In this case, as represented in Figure 3.34, simulations starting from a random mixture of lipids, water, and one peptide molecule lead to the spontaneous formation of a bilayer membrane in a computationally accessible time (10-100 ns) and the peptide is able to position in the most favorable local environment.

Two independent simulations were performed for PMAP-23 in order to test the reliability of the results.

In 100 ns of simulation a lipid bilayer formed in both cases, although a rather stable water-filled pore was still present, as previously observed in all simulations of spontaneous bilayer formation [Carpenter *et al*., 2008; Marrink *et al.,* 2001; de Vries *et al*., 2004 and Leontiadou *et al*., 2006]. To facilitate elimination of bilayer defects, the system was cycled repeatedly between 300 K and 375 K (rising the temperature linearly in 2 ns, decreasing it in 50 ps, and keeping it constant at 300 K for 950 ps). This annealing protocol did not cause significant modifications in peptide conformation or position. After the

water channel was eliminated, the trajectory was extended for further 10 ns keeping the temperature at 300 K. Very similar results were obtained in both simulations.

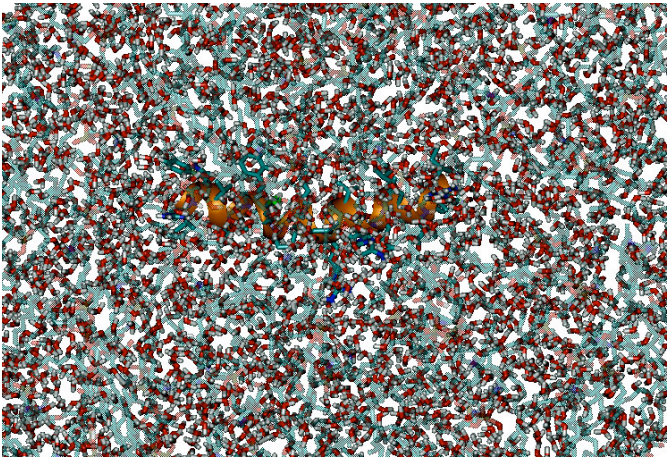

Figure 3.34. The situation at the beginning of the simulation of a PMAP-23–POPC/POPG system. Water oxygen atoms are colored in red and hydrogen atoms in white. Phospholipid acyl chains are colored in cyan. The peptide is shown in orange.

Figure 3.35A illustrates PMAP-23 position inside the bilayer, at the end of one of the two simulations: the peptide lies parallel to the membrane surface, at the interface between the polar and apolar regions. The positional distribution of the indole moieties of both Trp residues was centered at about 1 nm from the bilayer center (Figure 3.35B), in agreement with the depth-dependent fluorescence quenching experiments. The helical conformation of the peptide was substantially maintained, but a significant discontinuity was observed in correspondence of the central segment (where the two Pro residues are

located), in agreement with previous NMR experiments in detergent micelles [Park *et al.*, 2002]. In this conformation, the peptide side chains were arranged in an amphiphilic orientation, but two of the charged side chains (Arg10 and Lys14) were forced in the apolar side.

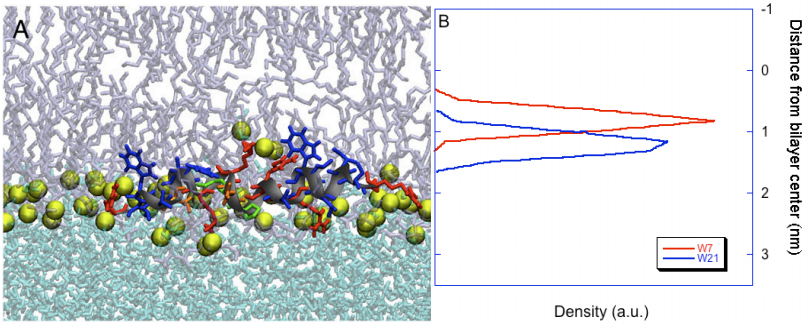

Figure 3.35. A: Representative structure at the end of a MD simulations (100 ns) of PMAP-23 in a membrane. Water is represented in cyan, phospholipids in grey, and phospholipids phosphorus atoms as yellow spheres. The peptide backbone is shown in grey, charged sidechains in red, polar aminoacids in orange, apolar residues in blue, and prolines in green. B: Density distribution of the indole moieties of the two Trp residues of PMAP-23 in the same MD simulation, averaged over the trajectory segment after formation of a defect-free bilayer.

This arrangement appears to be imposed by the peculiar features of PMAP-23: Arg10 takes part in a helical segment comprising also Arg8 and Arg11, and it would be impossible for these three charged side chains to point all towards the same side of the helix. Similarly, Lys14 is strongly constrained, being located between Pro12 and Pro15, which is then followed by another Lys residue. Notwithstanding the forced imperfect amphiphlic arrangement of the charged side chains, peptide association to the phospholipid bilayer is ensured by the high membrane affinity of the two amphiphilic helical segments [White *et al.,*

1998].

The minimum bias approach was applied also to trichogin GA IV. Three independent simulations were performed with different initial random configurations of water and lipids, and with trichogin GA IV initially shaped in the helical conformation determined by X-ray diffraction [Toniolo *et al*., 1994].

In all cases, the helical conformation of trichogin GA IV was essentially maintained during the whole trajectory length, confirming the high helical propensity bestowed on this peptide by the Aib residues. In addition, in all simulations, trichogin GA IV positioned at the water–lipid interface, essentially parallel to it, since the very early stages of the trajectories. In two of the three simulations, this arrangement resulted in a final peptide orientation parallel to the membrane plane, a position just below the polar headgroups region, and a helix rotation such that all hydrophobic side chains were pointing towards the lipid bulk of the bilayer (Figure 3.36A). However, in the third simulation, trichogin GA IV reached a final orientation parallel to the bilayer normal (Figure 3.36B). It's interesting to note how this final configuration was attained: in the first stages of the trajectory the peptide located at the boundary between the water and lipid phases, as in all other cases. However, by contrast to the other two simulations, in this trajectory the bilayer formed perpendicularly to the trichogin GA IV molecule. The peptide was still located at the water–membrane interface, lining the water-filled membrane defect which was transiently present in all simulations. When this bilayer defect healed spontaneously, the peptide remained in a transmembrane orientation,

fully immersed in the membrane hydrophobic core, and this configuration was stably maintained for all the remaining length of the trajectory (Figure 3.38).

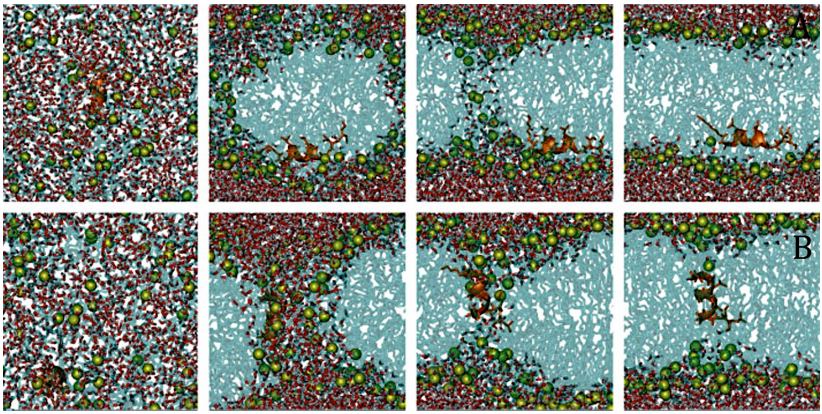

Figure 3.36. Bilayer formation during two different MD simulations of a trichogin GA IV–POPC system. The panels represent, from left to right, the situation at the beginning of the simulation, after 30 ns, after 100 ns (A) or 70 ns (B) and at the end of the trajectory. Water oxygen atoms are colored in red and hydrogen atoms in white. Phospholipid phosphorus atoms are represented as yellow spheres and the acyl chains are colored in cyan. The peptide is shown in orange. [Bocchinfuso *et al*., 2009]

The position determined by these MD simulations for trichogin GA IV differs from the location observed for PMAP-23, under two respects: the latter peptide was always found to lie parallel to the membrane plane, and at a shallower depth than trichogin GA IV. The average position of the trichogin GA IV backbone atoms was found to be at 0.8 nm below the phosphorus atoms of the phospholipids, while that of PMAP-23 was at a depth of just 0.4 nm, as illustrated also in Figures 3.35 and 3.36A.

The transmembrane location observed in one of the MD

simulations (Figure 3.36B) was in perfect agreement with all available experimental data, showing that trichogin GA IV undergoes a two-state transition from an inactive form, which is monomeric and lies close to the membrane surface, parallel to it, to an aggregated state, responsible for membrane leakage, where the peptide is more deeply buried into the phospholipid bilayer.

ORDER PARAMETERS

Other differences in the effects caused by membrane association of the two peptides can be highlighted by calculating the order parameter for the lipid acyl chains with respect to the bilayer normal in the simulated trajectories [Egberts *et al.*, 1994].

This parameter, defined in Equation E3.10, provides a quantitative estimate of the extent of lipid chain orientation along the bilayer normal, i.e. of the structural order of the membrane (θ is the angle between the bilayer normal and the bond considered).

$$S = \frac{3\left\langle \cos^2(\theta) \right\rangle - 1}{2} \qquad \text{(E3.10)}$$

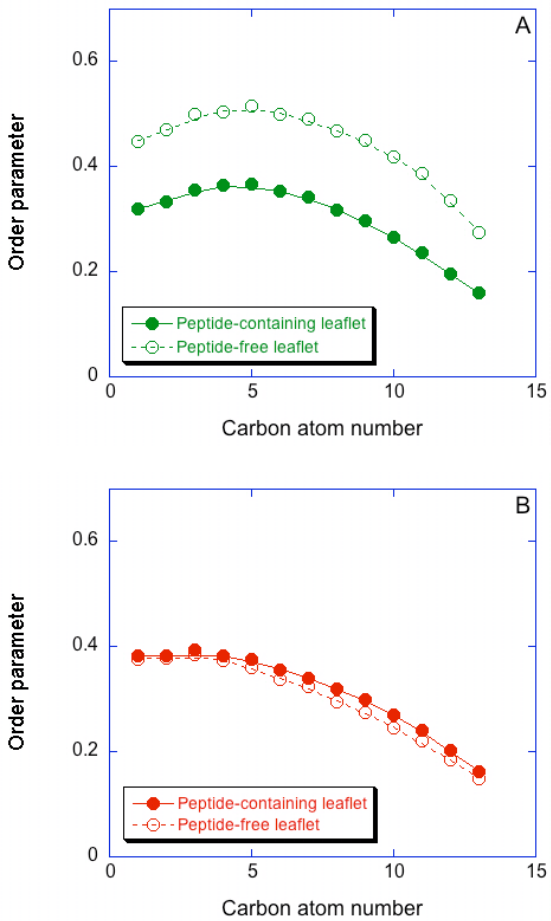

Figure 3.37. Order parameters with respect to the bilayer normal for the C_i-C_{i+1} bonds of the palmitic lipid chains, for the peptide-containing (full circles) and peptide-free (empty circles) leaflets of the membrane in the two simulations of PMAP-23 (A) and in the two simulations with the surface bound trichogin GA IV (B), averaged over the last 10 ns of both trajectories. [Bocchinfuso *et al.*, 2009]

A considerable difference in the lipid order was observed between the peptide-containing and the peptide-free bilayer leaflets in

the case of PMAP-23, while these differences were not significant in the two simulations with a surface-bound trichogin GA IV (Figure 3.37), in agreement with the fluorescence results. These results clearly indicate that the local disorder induced by peptide binding in the phospholipid chains is the dominant cause of the broad quenching profile observed for PMAP-23 in 3.3.3.

TRICHOGIN GA IV AND MEMBRANE THICKNESS

Finally, it is interesting to discuss the effects of trichogin GA IV on the bilayer structure when it is arranged in a transmembrane orientation. Notwithstanding the relatively short length of the peptide helix, which is only about half the normal thickness of the bilayer, trichogin GA IV is able to span the bilayer from one side to the other by causing a local thinning of the membrane (Figure 3.38). This effect might be related to the well-known phenomenon called ''hydrophobic mismatch'' [de Planque *et al.,* 1998, Duque *et al*., 2002 and Kandasamy and Larson, 2006]: when hydrophobic molecules inserted into lipid membranes do not match the normal thickness of the bilayer, then the membrane adapts itself by thickening or thinning to match its size to that of the inserted molecule, thus minimizing the exposure of hydrophobic moieties to the water phase.

Therefore, the present results might provide a solution to the longstanding puzzle regarding the mechanism of action of trichogin GA IV. Notwithstanding the experimental evidence supporting a barrel-stave mechanism of action for this peptide, it was thought that the short length of its chain would require a complex (and unlikely)

supramolecular architecture to form the pore, e.g. with two peptide chains stacked on top of each other to span the bilayer from one side to the other. However, the simulations indicate that this is not necessary and that, thanks to the plasticity of the bilayer membranes, even a single trichogin GA IV chain might able to reach both sides of the bilayer.

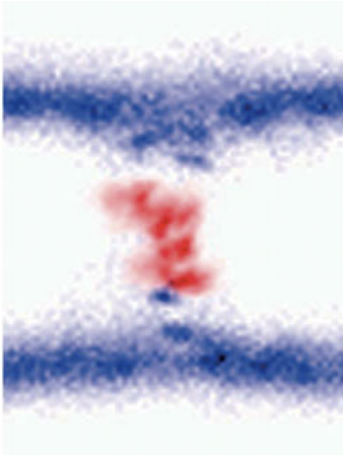

Figure 3.38. Density map of the lipid phosphorus atoms (blue) and of the peptide atoms (red) averaged over the last 10 ns of the trajectory in which trichogin GA IV attained a transmembrane orientation. [Bocchinfuso *et al.*, 2009]

3.4. Role of specific residues in the mechanism of action of PMAP-23

Our data indicate that PMAP-23 destabilizes membranes by causing a difference in surface tension between the two leaflets of the membrane. However, MD simulations, and an analysis of PMAP-23 sequence,

suggest also an additional, and more specific mechanism of bilayer destabilization, involving the insertion of charged residues Arg10 and Lys14 into the hydrophobic core of the membrane, and generation of local disorder in the bilayer. In order to determine if these two residues play a significant role in the membrane-perturbing activity of PMAP-23, analogues of this peptide were synthesized by substituting Arg10 or Lys 14 with Ala. The alanine residue was chosen because it occupies a middle position in the hydropathy scale of Wimley and White [White and Wimley, 1999], with a free energy of water-membrane partition close to zero.

The effect of these substitutions on peptide aggregation in water, affinity for membranes and membrane-perturbing activity were characterized.

3.4.1. Peptide aggregation in water

The absorption spectra of analogues Arg10Ala and Lys14Ala at a concentration of about 0.7 mM exhibit marked apparent absorption due to light scattering caused by a significant degree of aggregation. This is obviously due to the higher hydrophobicity of these analogues as compared to PMAP-23. (Figure 3.39).

In order to find out if a concentration range exists where aggregation of the analogues is negligible, turbidity measurements at 350 nm (a wavelength where these peptides do not absorb) were performed as a function of peptide concentration (Figure 3.40)

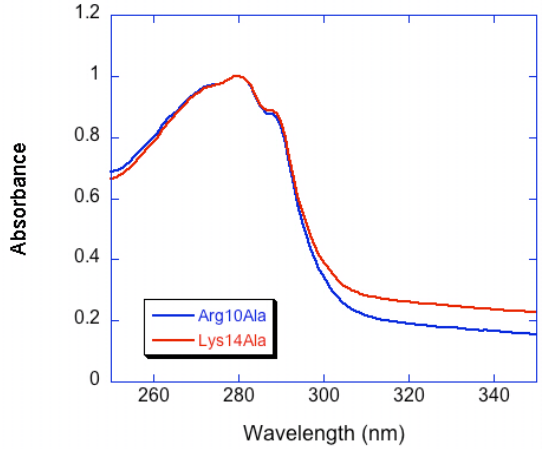

Figure 3.39. Normalized UV absorption spectra of PMAP-23 analogues in buffer. Pathlength 1 mm. [Arg10Ala]=0.71 mM and [Lys14Ala]=0.74 mM.

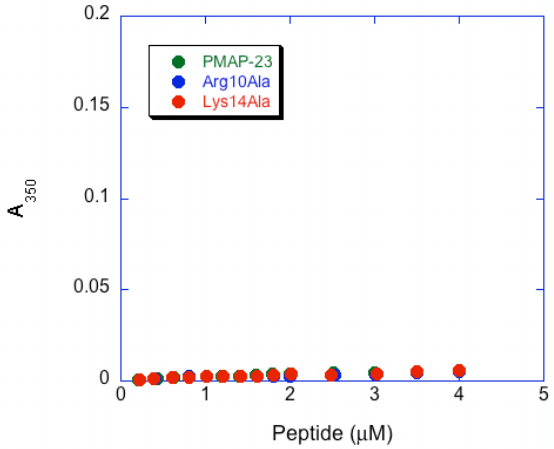

Figure 3.40. Experiments on peptide aggregation in water (10 mM phosphate buffer, pH 7.4 containing 0.1 mM EDTA): absorbance at 350 nm. Pathlength 1 cm.

These data demonstrate that peptide aggregation is negligible, at least up to a 4 μM concentration.

3.4.2. Water-membrane peptide partition

To characterize the membrane affinity of PMAP-23 and its analogues, aqueous solutions of the peptides were titrated with increasing concentrations of liposomes, as described in paragraph 3.3.1, and following the association process by the blue-shif it causes (Figure 3.41).

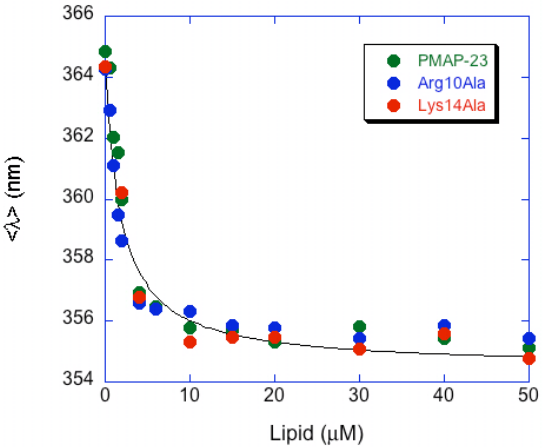

Figure 3.41. Water-membrane partition for PMAP-23 and its analogues. Variation in the average wavelength of the emission spectra caused by membrane binding. Peptide concentration 1 μM.

The modified analogues of PMAP-23 exhibit the same membrane affinity of the parent peptide. These finding are surprising because the

insertion of charged residues Arg10 and Lys14 in the lipid phase is energetically unfavorable, and therefore the affinity for membranes could be higher in the case of two Alanine analogues; nevertheless, the difference might be negligible compared to the high membrane affinity of the peptide[White *et al*., 1998]. In addition, PMAP-23 has a higher net charge than the analogues, and this causes a more pronounced increase in peptide local concentration increasing close to the membrane, thus favoring membrane association. This electrostatic effect apparently balances the free energy cost of insertion of the two charged residues in the bilayer.

3.4.3. Peptide effect on membrane dynamics: DPH experiments

In order to verify whether the charged residues inserted in the membrane have a significant effect of lipid order, membrane dynamics was examined by employing DPH (see 3.3.7). The effects of PMAP-23 and of the Ala analogues are comparable (Figure 3.42), indicating that the two modified residues do not play a significant specific role.

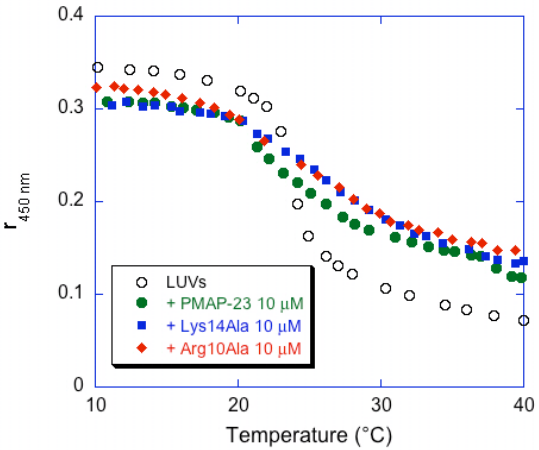

Figure 3.42. Effect of peptide–membrane interactions on the thermotropic phase transition of dimyristoyl phospholipid vesicles, as followed by measuring the fluorescence anisotropy of DPH in the absence (empty circles) and in the presence of peptides (empty symbols). [Lipid]= 50 μM.

3.4.4. Membrane-perturbing activity

The membrane-perturbing activity of PMAP-23 and its analogues was determined by measuring the peptide-induced leakage of carboxyfluorescein (CF) entrapped inside phospholipid vesicles, as a function of peptide concentration (see 3.3.2).

The activity of PMAP-23, Arg10Ala and Lys14Ala (Figure 3.43) is comparable, confirming that the two modified residues do not have any specific role in the membrane activity of PMAP-23.

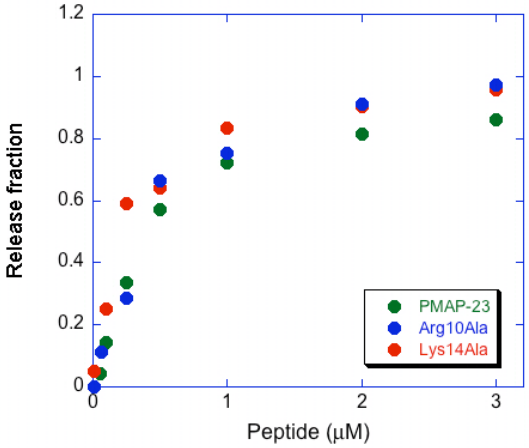

Figure 3.43. Fractional release of liposome-entrapped carboxyfluorescein 20 minutes after addition of PMAP-23 ant its analogues to vesicles. [Lipid]=0.2 mM.

3.5. Conclusions

The spectroscopic data reported in the present work, together with MD simulations, and experiments on Langmuir lipid monolayers provide a clear picture of the mechanism of membrane perturbation by the cathelicidin AMP PMAP-23. In this section, the main findings are summarized, and compared with similar results previously reported for another AMP, i.e. trichogin GA IV, to highlight the potency of our approach in discriminating the different mechanisms of pore formation. Both peptides are short and attain a helical conformation when associated to lipid bilayers, with an amphiphilic distribution of the side-chains, but PMAP-23 is strongly cationic, with a net charge of +6 at a physiological pH, while trichogin GA IV is neutral.

The different physicochemical properties of the two peptides are evident already in water, where trichogin GA IV shows a strong tendency to aggregate, with an almost complete aggregation already at a 15 μM peptide concentration. By contrast, PMAP-23 aggregation is negligible in this concentration range. This phenomenon, while not directly related to peptide-membrane interaction, does influence the membrane activity of trichogin GA IV, since peptide aggregation competes with peptide-membrane association.

In the membrane, PMAP-23 is always located at a depth corresponding approximately to the interface between the polar headgroups region and the hydrophobic core of the bilayer, oriented parallel to the membrane plane. PMAP-23 remains associated to the outer bilayer of the vesicles, without translocating to the inner leaflet, at least at concentrations below the threshold for pore formation. By contrast, trichogin GA IV is evenly distributed between the two leaflets of the bilayer even at concentrations at which it is not active, and it exhibits a cooperative transition, controlled by the concentration of membrane-bound peptide, from a surface-bound monomeric state, essentially similar to that observed for PMAP-23, to a membrane inserted state, in which the peptide is aggregated. In the case of trichogin GA IV, only this second state is responsible for pore formation.

Also the effects of the two peptides on lipid bilayers are significantly different: PMAP-23 insertion in the membrane causes a significant perturbation in the lipid order, while trichogin GA IV has no such effect. Both peptides induce vesicle leakage through the formation of pores, but in the case of PMAP-23 this process is strongly coupled to

peptide-induced lipid flip-flop, while this is not the case for trichogin GA IV.

All these data point to two different mechanisms of action for the two peptides: PMAP-23 perturbs membrane permeability according to the "carpet" mechanism: it accumulates in the outer layer of the membrane, thus causing a difference in surface tension between the two leaflet of the bilayer. When a threshold concentration is reached, this tension is released by forming membrane defects, which allow a redistribution of peptides and phospholipids in the two leaflets of the membrane. Concomitantly, vesicle contents are released. Trichogin GA IV, on the other hand, acts according to the "barrel-stave" mechanism. At low concentrations this neutral, rather hydrophobic peptide binds to the membrane surface, but it is able to distribute in both bilayer leaflets, through a transient inserted state. As the peptide concentration increases, excluded volume effects favor the membrane-inserted state, which becomes significantly populated. When inserted in the bilayer in a transmembrane orientation, trichogin GA IV molecules have a strong tendency to aggregate, forming a "barrel-stave" pore in which the hydrophilic sides of the peptide helices face the water-filled lumen. These pores are responsible for membrane leakage.

The different behavior of the two peptides is easily explained by the differences in their physico-chemical properties: the high net charge of PMAP-23 makes its insertion in the bilayer highly unfavorable. Therefore, no barrel-stave pores can form for this peptide, while the lack of peptide translocation across the bilayer causes the accumulation

of a tension which is eventually released by the formation of membrane defects.

In conclusion, the synergistic application of spectroscopic techniques and computer simulations allows a precise structural characterization of the peptide-membrane interaction process and of the mechanism of pore formation, and an accurate discrimination between different models. Our data indicate the carpet model as the most likely mechanism of pore formation by cationic AMPs, while neutral peptides appear to follow the barrel-stave model.

Chapter 4

RESULTS AND DISCUSSION: THE RATE LIMITING STEP OF PEPTIDE-INDUCED MEMBRANE LEAKAGE

Peptide-induced vesicle leakage is a common experimental test of the membrane-perturbing activity of antimicrobial peptides and was used also in this work to characterize the activity of PMAP-23. Obviously, a quantitative analysis of the peptide-induced leakage kinetics can potentially provide several insights into the pore formation mechanism. For this reason, several studies strived to achieve a mechanistic understanding of the leakage kinetics. Leakage curves have been measured for many different AMPs and toxins, and in most cases they share two peculiar characteristics (an example is shown in Figure 4.1):

1) they are surprisingly slow, requiring minutes to hours for complete leakage, while simple considerations show that the time needed to empty a 100 nm liposome through a single pore is in the ms range [Schwarz and Robert, 1992];

2) they exhibit a strongly nonexponential behavior, with a fast initial leakage that progressively slows down.

Peptides for which these two properties have been observed include melittin [DeGrado *et al.*, 1982; Portlock *et al.*, 1990; Schwarz *et*

al., 1992; Benachir and Lafleur, 1995, Rex and Schwarz, 1998], mastoparan [Arbuzova and Schwarz, 1999; Yandek *et al.*, 2009], cecropin [Gregory *et al.*, 2008], α-toxin [Belmonte *et al.*, 1987], δ-lysin [Pokorny *et al.*, 2002; Pokorny and Almeida, 2004], transportan 10 [Yandek *et al.*, 2007], alamethicin [Schwarz and Robert, 1990; Portlock *et al.*, 1990], gramicidin [Portlock *et al.*, 1990], magainin [Grant *et al.*, 1992; Matsuzaki *et al.*, 1994; Gregory *et al.*, 2009], pardaxin [Saberwal and Nagaraj, 1993; Rapaport *et al.*, 1996], and model amphipathic peptides [Kanellis *et al.*, 1980, Parente *et al.*, 1990; Rathinakumar and White, 2008]. Importantly, De Grado and coworkers have shown that the leakage kinetics induced in cells (e.g. hemolysis), is remarkably similar to liposome release [DeGrado *et al.*, 1982].

The same fact that these studies span almost thirty years, and that many peptides have been studied over and over, shows that a satisfactory explanation of the experimentally observed behavior is elusive. One of the more debated points regards the rate-limiting step responsible for the very slow kinetics. Several different hypotheses have been put forward regarding this question: peptide-membrane binding [Saberwal and Nagaraj, 1993], a conformational transition of the peptide [Rex and Schwarz, 1998], peptide aggregation [DeGrado *et al.*, 1982; Parente *et al.*, 1990; Schwarz *et al.*, 1992; Ostolaza *et al.*, 1993; Matsuzaki *et al.*, 1994; Pokorny *et al.*, 2002; Pokorny and Almeida, 2004], pore formation [Schwarz and Robert, 1990; Gregory *et al.*, 2008; Gregory *et al.*, 2009], pore opening [Andersson *et al.*, 2007] or peptide translocation across the bilayer [Andersson *et al.*, 2007; Yandek *et al.*, 2009].

Similarly, several hypotheses have been proposed in order to explain the progressive slowing down of the kinetics, such as peptide inactivation due to a conformational transition [Grant *et al.*, 1992], aggregation [DeGrado *et al.*, 1982], or translocation across the membrane [Yandek *et al.*, 2007; Rathinakumar and White, 2008; Yandek *et al.*, 2009].

In this work, we systematically evaluate all the possibilities for the rate-limiting step, by taking as an a example the fluorescent trichogin GA IV analogue F10. This choice was due to the fact that, as summarized in the previous chapter, the peculiar time resolved properties of this peptide allowed, in previous studies, a detailed characterization of its behavior, and a quantitative determination of all peptide species present in a vesicle suspension (monomeric and aggregated, both in water and in the membrane phase).

The results reported in the present study show that all of the steps involved in peptide-membrane interaction (binding, aggregation, translocation) are much faster than the release kinetics, and that the origin of the slow leakage observed in a population of vesicles must be found in a largely overlooked, but very basic property of this experimental system, i.e. its discrete nature.

In all the models previously proposed to describe the leakage kinetics, ordinary differential equations were employed, essentially equating the system to a continuum. By contrast, a vesicle (or cell) suspension is obviously a discrete system, and the release of the contents of each vesicle is not influenced by the other liposomes in the sample. A liposome is a relatively small system, and the number of

peptides or the number of pores in each vesicle can be rather small, well below the thermodynamic limit. Recently, a large body of studies demonstrated that the kinetics of such systems can be dramatically different from that predicted by continuous differential equations, due to the significant fluctuations caused by the low number of molecules involved [Shnerb *et al.*, 2000; Goutsias, 2007 and Cao and Samuels, 2009].

4.1. Release kinetics

Figure 4.1 shows the vesicle release kinetics determined at different peptide concentrations. Several aspects are immediately evident from these data: a) release curves do not follow a simple exponential behavior; b) they are extremely slow, extending for many tens of minutes; c) release kinetics is strongly dependent on the peptide/lipid ratio. These curves are characterized by a burst phase, where a significant fraction of the vesicles contents is released, and by a much slower leakage phase. Interestingly, all curves lead to complete leakage, after sufficient time, as shown in Figure 4.2.

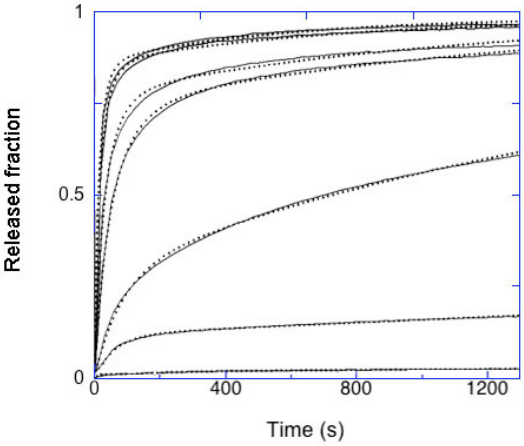

Figure 4.1. Kinetics of carboxyfluorescein release after addition of peptide (at time= 0 s), as a function of F10 concentration. [Lipid]=0.2mM and [F10]= 1.2 μM; 2.3 μM; 3.7 μM; 4.7 μM; 6.9 μM; 10.8 μM; 13.9 μM (from bottom to top). The dotted lines are the best fit to the data with the model described in the present work.

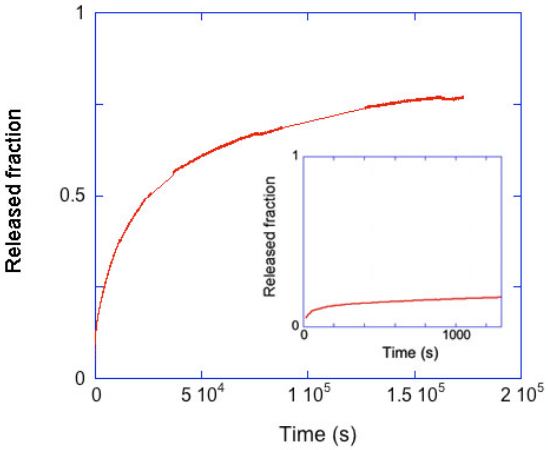

Figure 4.2. Kinetics of the release from loaded vesicles at [F10]= 2.3 μM and [Lipid] = 0.2 mM. Note that after 40 hours the carboxyfluorescein efflux out of liposomes did not stop. 20 minutes after peptide addition, the released fraction was less than 0.20 (inset).

4.2. Binding, aggregation and translocation kinetics

In order to determine the rate-limiting step of the leakage process, kinetic experiments of peptide binding to the membrane and formation of aggregates were performed. In the case of the fluorescent trichogin analogue F10, it was shown that four species are present (monomeric and aggregated peptide, both in the water and in the membrane phase), and that each of them is characterized by a different quantum yield and fluorescent lifetime [Stella, L. *et al*. 2004]. Therefore, water to membrane partition and peptide aggregation do all cause a variation in the fluorescence intensity signal.

Figure 4.3 (green line) shows the results of stopped flow experiments performed by mixing a concentrated solution of the peptide to a solution of lipid vesicles. The fluorescence signal exhibited an initial decrease, due to peptide aggregation, followed by a strong increase, caused by water to membrane partition. Interestingly, all signal variations were completed after approximately 30 s, i.e. on a time-scale much shorter than that of vesicle leakage experiments.

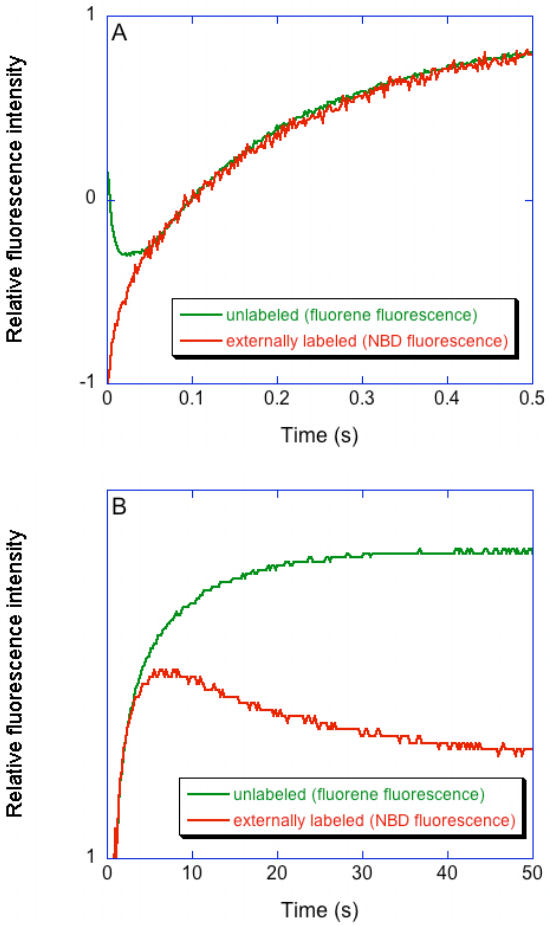

Figure 4.3. Stopped-flow experiments on F10-membrane interaction. Two different timescales are reported in panel A and B. 30 µL of a concentrated F10 methanolic solution were mixed with 300 µL of an aqueous suspension of lipid vesicles. Final concentrations: [F10] = 0.5 µM [Lipid] = 200 µM. Fluorene was excited with 265 nm light (bandpass 2 nm). Continuous lines: F10 was added to ePC/cholesterol (1:1 mol/mol) vesicles, and fluorene emission was collected through a 305 nm cutoff filter. Dotted lines: F10 was added to ePC/cholesterol (1:1 mol/mol) vesicles labeled on the external leaflet of the bilayer with 0.5% C6-NBD- PC. NBD emission was collected through a 385 nm cutoff filter.

Previous studies have shown that F10 is able to rapidly translocate across the bilayer, but the time-scale of this process was not determined [Mazzuca *et al.,* 2005]. To further characterize this process, stopped flow experiments were performed also with lipid vesicles labeled with the fluorescent lipid analogue C6-NBD-PC.

The vesicles were labeled, on the external leaflet of the bilayer only, with C6-NBD-PC, which can act as a (FRET) acceptor for fluorene. In the stopped-flow experiments, the changes in NBD emission caused by peptide association to the membrane were followed. The water to membrane partition of the peptide caused a significant increase in NBD emission, which followed the same kinetics observed for fluorene fluorescence. However, on a slightly longer timescale, a decrease in NBD emission was observed, caused by the translocation of a fraction of the peptide from the C6-NBD-PC labeled leaflet to the unlabeled leaflet. Even the translocation process was completed in approximately 50 s, i.e. on a timescale much faster than that of the vesicle leakage process (Figure 4.3, red line).

These data demonstrate that water to membrane partition, peptide aggregation and peptide translocation are not the rate-limiting step of the slow vesicle leakage process, since they are completed in a time several orders of magnitude shorter than the release of liposome contents.

4.3. Leakage of a single vesicle

Another possibility for the long timescale observed in the leakage experiments is that the rate-limiting step is connected to the time needed by a single vesicle to completely release its contents, after the formation of at least one peptide-induced pore.

An estimate of this timescale can be obtained by applying first Fick's law, which describes the diffusion-mediated flow of fluorescent molecules through open pores as:

$$\frac{d\left(C_{in}-C_{out}\right)}{dt}=-\frac{1}{\Phi}\left(C_{in}-C_{out}\right) \qquad \text{(E4.1)}$$

$$\left[C_{in}(t)-C_{out}\right]=\left[C_{in}(0)-C_{out}\right]e^{-\frac{t}{\Phi}} \qquad \text{(E4.2)}$$

$$\Phi=\frac{4}{3}\pi R^{3}\frac{d}{A_{P}D_{0}} \qquad \text{(E4.3)}$$

where C_{in} and C_{out} stand for the fluorophore concentrations at the internal and external pore bounds, respectively, D_0 is the diffusion coefficient of the fluorophore in the pore, d is thickness of the membrane, A_p is the total pore cross-sectional area, and R is the vesicle radius [Schwarz, G. et al. 1992]. In the leakage experiments described in Figure 4.1, $R \sim 50$ nm (radius of the pores of polycarbonate extrusion

filters), d = 4 nm [Lis *et al*., 1982] and D_0 =2.17·10^8 nm^2/s [Mastuzaki *et al*., 1995b]. By assuming a minimal pore diameter of 1 nm (corresponding to the approximate size of the carboxyfluorescein molecules), A_p for a single pore can be estimated to be higher than 0.8 nm^2. Substitution of these parameters into the above equations, gives values of $\Phi \sim 10$ ms, indicating that the time needed to empty a single vesicle can be excluded as a possible rate-limiting step.

A direct assessment of the timescale of this process can be experimentally obtained by employing GUVs. Such an experiment is displayed in Figure 4.4, and it shows that F10 induced the complete release of the vesicle contents, without destroying the membrane, providing direct evidence for the formation of pores. The leakage of GUV contents was completed in a few minutes, and this time included also the time needed for peptide diffusion from the site of addition to the vesicle under observation (since no stirring was possible in the observation chamber), and for pore formation. Since the diameter of the LUVs employed in the leakage experiments of Figure 4.1 was approximately 500 times smaller than that of the GUV shown in Figure 4.4, this result, and Equation E4.3, confine the time needed for emptying a single LUV after pore formation in a timescale much shorter than that of the leakage experiments reported in Figure 4.1.

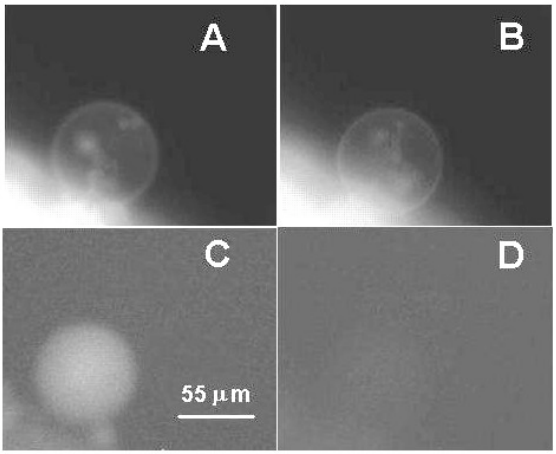

Figure 4.4. Giant unilamellar vesicle before (A, C) and 12 minutes after (B, D) peptide addition ([F10] = 6 μM). A and B panels show the emission of rhodamine-labeled phospholipids, while C and D refer to the fluorescence carboxyfluorescein entrapped inside the vesicle.

4.4. Size dependence of the vesicle leakage

Further information on the leakage process from a population of vesicles was obtained by studying the dependence of the LUVs release kinetics on the liposome size. The vesicle size distribution for three different preparations, obtained by extrusion through membranes with pore size 100, 200 and 400 nm was determined by light scattering experiments performed by Prof. M. De Spirito, at the Physics Institute of Università Cattolica del Sacro Cuore (Rome). The results are reported in Figure 4.5: the actual average radius was 56, 83, and 140 nm, respectively. The leakage curves were determined for these three vesicle preparations at the same peptide and lipid concentrations, in

order to obtain the same membrane-bound peptide surface density in all cases.

These curves are shown in Figure 4.6, and show that the release velocity from a population of vesicles (and the fraction of vesicle contents released) increases with vesicle size. This result is counterintuitive, and it is opposite to the size dependence for the release from a single vesicle, after a pore is formed (Equation E4.3). The explicit size-dependence of Φ in Equation E4.3 is proportional to R^3. However, it should be considered that with increasing radius also the membrane surface of each vesicle increases. Since the membrane-bound peptide surface density was constant in the experiments of Figure 4.6, the average number of pores formed in the membrane of each vesicle increases with R^2. For this reason, A_p (which is the cross-sectional area of a single pore multiplied by the number of pores) increases proportionally to the vesicle surface, and overall Equation E4.3 predicts an increase in Φ proportional to R. By contrast, the opposite trend was observed in the experiments reported in Figure 4.6. This finding confirms that the release of vesicle contents after pore formation in each liposome is not the rate limiting step in the "ensemble" leakage experiments, and suggests that a phenomenon related to the vesicle surface area is involved.

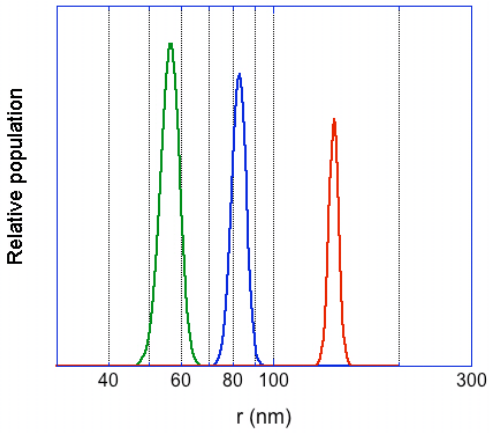

Figure 4.5. Size distribution of LUVs extruded through polycarbonate membranes with nominal pore radii of 50, 100, and 200 nm (green, blue and red line, respectively), as determined by light scattering experiments.

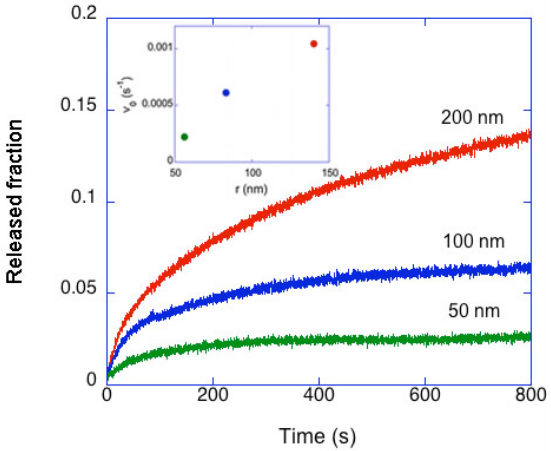

Figure 4.6. Leakage kinetics as a function of vesicle size. The three leakage curves were measured for three ePC/cholesterol (1:1 mol:mol) vesicle preparations, extruded through pores with nominal radius 50, 100 and 200 nm. The inset shows the initial release velocity (calculated in the first 20 s of the leakage process), as a function of the actual average radius of the vesicles, as determined by light scattering experiments (see Figure 4.5).

4.5. Peptide exchange between vesicles

In order to further characterize all processes involved in the vesicle leakage kinetics, the exchange of peptides between vesicles was studied, to verify if F10 is able to rapidly distribute in the whole vesicle population.

Figure 4.7 shows the leakage curve obtained by adding F10 to 0.2 mM carboxyfluorescein-filled vesicles. At the time indicated by the arrow, a large excess (10:1) of carboxyfluorescein-free vesicles was added, resulting in an immediate stop of the release process. Peptide exchange between liposomes took place within the mixing time, causing a high dilution of F10 concentration in the membrane. Peptide concentration dropped below the threshold needed for pore formation and the leakage process stopped.

A further confirmation of the rapid peptide exchange between vesicle came from an additional experiment. F10 was mixed with unlabeled lipid vesicles, at a lipid concentration sufficient to induce an almost complete membrane association of the peptide. After complete equilibration, CF-containing vesicles were added to this sample, and their leakage was followed in time. The leakage kinetics started immediately, and followed a behavior very similar to that observed when the peptide was added directly to a mixture of CF-loaded and unloaded vesicles, confirming that the peptide bound to the unlabeled vesicles in the first curve was able to distribute in the whole vesicle population (Figure 4.8). Furthermore, this experiment indicates that the peptides do not suffer any significant inactivation following their initial

binding to the membrane, a hypothesis often evoked to explain the biphasic behavior of the leakage kinetics.

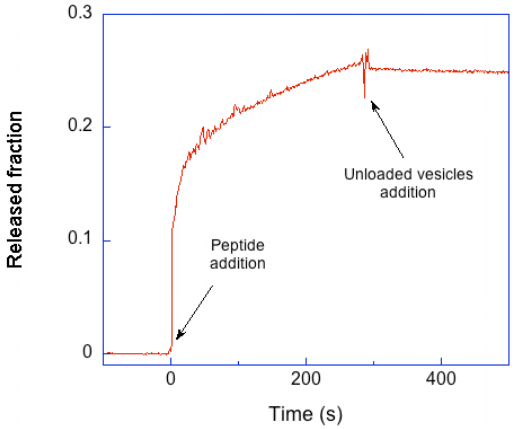

Figure 4.7. F10-induced carboxyfluorescein release ([lipid]=0.2mM) was stopped by the addition of 2mM unloaded vesicles.

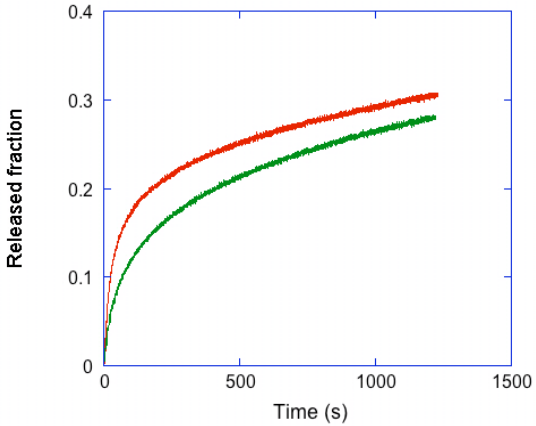

Figure 4.8. F10 induced carboxyfluorescein release Green curve: F10 was incubated with vesicles not containing CF, and at time 0 CF-loaded vesicles were added. Red curve: F10 was added directly to a mixture of loaded and unloaded vesicles.

4.6. Kinetic model

All processes involved in peptide-membrane interaction (peptide-membrane association, peptide aggregation and peptide translocation) take place in a time-scale much shorter than the leakage kinetics. However, peptides are continually exchanging among vesicles, and this necessarily causes fluctuations over time in the number of peptide molecules bound to each vesicle, and in the formation of pores.

A simple stochastic model that takes into account these fluctuations is proposed here.

Under the hypothesis that all process involved in peptide-membrane interaction take place in a time-scale much shorter than the leakage kinetics, equilibrium is rapidly reached and therefore at a given peptide and lipid concentration, also the total number of pores is constant. However, due to local fluctuations, some vesicles do not contain a pore. *P(0)* is the probability that a given vesicle contains no pores and depends on peptide and lipid concentration, and on vesicle size. If it is assumed also that vesicles that contain a pore empty instantaneously in the time-scale of the leakage kinetics, the overall fraction of full vesicles decays "instantaneously" to the value *P(0)*. However, peptide exchange between vesicles ensures that this decay continues, because even the vesicles that never had a pore in their membrane can get one due to fluctuations.

The fraction of full vesicles coincides with the fraction of vesicles that up to time t never had a pore in their membrane, *F(t).* This value decays with a rate proportional to the probability that a pore forms in a

specific vesicle in a definite time interval. This probability is proportional to *1-P(0)*, and therefore we can write:

$$\frac{dF(t)}{dt} = -\frac{1}{\tau}\left[\sum_{m=1}^{\infty} P(m)\right]F(t) = -\frac{1}{\tau}\left[1 - P(0)\right]F(t) \quad \text{(E4.4)}$$

In this equation, τ is a time constant determining the time-scale of the fluctuations of the peptide concentration on any given vesicle.

By integrating this equation, one gets:

$$F(t) = P(0)e^{-\left[1-P(0)\right]\frac{t}{\tau}} \quad \text{(E4.5)}$$

Equation E4.5 predicts an instantaneous decay from 1 to *P(0)*, and then an exponential decay to 0 with rate *[1-P(0)]/τ*. Obviously, the fraction of vesicle contents released *R(t)* (i.e. the quantity measured in the experimental curves in Figure 4.1) corresponds to *1-F(t)*.

Equation E4.5 can be linked directly to the pore formation process, by assuming an explicit form for the probability distribution. A good approximation to *P(0)* can be provided by the Poisson distribution [Schwarz and Robert, 1990 and Barzel and Biham, 2009), i.e.

$$P(0) = e^{-\overline{n}} \quad \text{(E4.6)}$$

where $\overline{n}$ is the average number of pores per vesicle. In this case

Equation E4.5 becomes

$$F(t) = e^{-\bar{n}} e^{-\left[1-e^{-\bar{n}}\right]\frac{t}{\tau}} \qquad \text{(E4.7)}$$

Equation E4.7 captures the essential features of the experimental leakage curves: a burst phase, followed by a slower leakage; an extent of the burst phase which increases with peptide concentration; a faster leakage with increasing $\bar{n}$ (and therefore with increasing vesicle radius, if the surface density of peptide is constant). However, this Equation is not adequate to describe quantitatively the leakage curves, since the burst phase is not instantaneous.

If the initial approximation that all processes (except fluctuations) are instantaneous is released, a less sharp burst phase is predicted. For instance, by considering that the time needed by a pore-containing vesicle to release its contents cannot be neglected (but it still much faster than the peptide-exchange phenomenon), the fluorophore concentration inside vesicles decays as

$$C(t) = C(0)\sum_{m=0}^{\infty} P(m) e^{-m\frac{t}{\Phi}} \qquad \text{(E4.8)}$$

where Φ is characteristic release time for a single pore (Equation E4.3), and *P(m)* is the probability ho having *m* pores in a vesicle.

If we assume a Poisson distribution for *P(m)*, Equation E4.8

becomes

$$C(t) = C(0)\sum_{m=0}^{\infty} \frac{e^{-\bar{n}}\bar{n}^m}{m!} e^{-m\frac{t}{\Phi}} = C(0)e^{-\bar{n}\left(1-e^{-t/\Phi}\right)} \quad \text{(E4.9)}$$

If we combine Equations E4.9 and E4.6, we obtain that overall, the encapsulated fluorophore concentration decays as

$$C(t) = C(0)e^{-\bar{n}\left(1-e^{-t/\Phi}\right)} e^{-\left(1-e^{-\bar{n}}\right)\frac{t}{\tau}} \quad \text{(E4.10)}$$

The fraction of liposome contents released (i.e. the quantity measured in the experimental curves in Figure 4.1) is

$$R(t) = \frac{C(t)-C(0)}{C(0)} = 1 - e^{-\bar{n}\left(1-e^{-t/\Phi}\right)} e^{-\left(1-e^{-\bar{n}}\right)\frac{t}{\tau}} \quad \text{(E4.11)}$$

A fit to the release data with Equation E4.11 is presented in Figure 4.1 (dotted lines), and the parameters obtained from the fit are reported in Table 3.2: with just three variable parameter a satisfactory description of the decay curves is obtained. The data reported in Table 3.2 indicate that, at all peptide concentrations, $\Phi << \tau$, in agreement with the assumption. τ decreases with peptide concentration, as expected from its definition as the time-scale of peptide-concentration

fluctuations on any given vesicle. By contrast, Φ exhibits some variability, but this is probably due to the fact that only the release process was considered in deriving Equations E4.8-E4.11, while the data show that other processes can influence the kinetics in the first seconds after peptide addition. Furthermore, in this simple model, a monodisperse vesicle population is assumed, while some polydispersity is obviously present. It is interesting to note that Equation E4.11 provides an explanation for the observed ensemble leakage behavior as a function of vesicle radius (Figure 4.7): this equation predicts the kinetics to become faster as $\bar{n}$ increases, and all other parameters being equal, $\bar{n}$ increases with increasing *R*.

[F10] (μM)	$\bar{n}$	Φ (s)	τ (s)
0.1	0.003	90	4830
1.2	0.020	133	3460
2.3	0.13	64	2500
3.7	0.35	100	600
4.7	1.37	91	960
6.9	1.53	56	840
10.8	2.06	29	470
13.9	2.05	38	640

Table 3.2. Parameters corresponding to the best fit of the data in Figure 4.1 with Equation E4.11.

The most interesting result obtained from fitting the decay curves with Equation E4.11 is an estimate for $\bar{n}$, which increases from

0.003 to about 2, in the range investigated. These data can be compared to a completely independent determination of $\overline{n}$, obtained by time-resolved fluorescence experiments performed at equilibrium. Fluorene fluorescence is strongly sensitive to its environment, and aggregates have a distinctly different lifetime as compared to monomeric peptides. This allowed the determination of the fraction of membrane-bound peptide molecules participating in aggregates (which constitute the pores) [Stella *et al.,* 2004]. A rough estimate for the number of peptide molecules forming each aggregate was obtained from the concentration-dependence of the aggregation, and resulted to be about 25 [Gatto *et al.,* 2006]. By using this number, the time-resolved fluorescence data can be used to estimate $\overline{n}$.

The two datasets are compared in Figure 4.9, and they exhibit roughly the same trend as a function of total peptide concentration. Since these two estimates of $\overline{n}$ where obtained by completely independent measurements (kinetic versus equilibrium), they provide a strong support to the simple model used to describe the leakage kinetics. A discrepancy is observed between the quantitative values of $\overline{n}$ obtained by the two methods, indicating that not all aggregates constitute a pore: a critical aggregation number might be needed to obtain an open pore, or alternatively peptide aggregates could be present both in a "open" and in a "closed" state. In addition, the estimate for the aggregation number used to calculate $\overline{n}$ from time-resolved fluorescence data represents only an order of magnitude guess, obtained by assuming infinite cooperativity in the aggregation process,

and a single aggregation number.

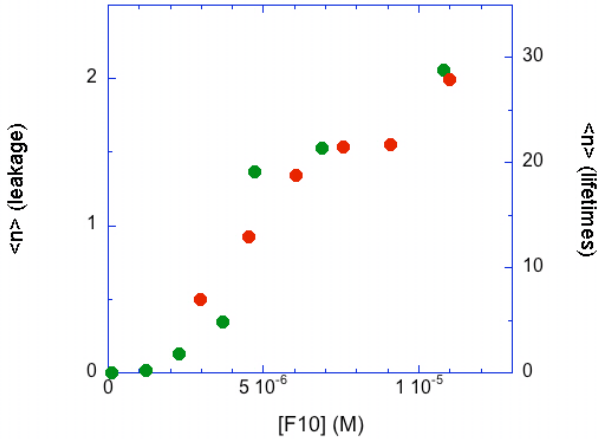

Figure 4.9. Estimate of the average number of pores in a single vesicle, obtained from the leakage kinetics (green circles) and from peptide fluorescence lifetimes (red circles), as a function of total peptide concentration. ePC/ cholesterol liposomes, [lipid]=200 μM, vesicle radius 50 nm.

4.7. Conclusions

According to the model proposed here, fluctuations in the number of peptides bound to each vesicles play a fundamental role in determining the leakage kinetics: a fast initial leakage is caused by those vesicles which, after the initial random distribution of peptides among liposomes, already contain at least one pore, while a slower release is associated to the time needed to occasionally reach, through peptide exchange among vesicles, the critical number of bound peptides necessary for pore formation in an intact vesicle.

This model captures the general features of the release kinetics observed for trichogin GA IV, and provides also a way to estimate the average number of peptide pores per vesicle from kinetic data. Since the same qualitative features have been observed also in the leakage induced by many other peptides (including PMAP-23), the question arises about the general validity of the model. The fact that peptide-membrane association is much faster than the leakage time-scale has been a general observation [Schwarz *et al*., 1987, Schwarz and Beschiashvili, 1989; Parente *et al*., 1990; Rapaport *et al*., 1996, Pokorny *et al.,* 2002; Gregory *et al*., 2008 and Gregory *et al*., 2009], and both theoretical considerations and experimental data led to a general agreement on the fact the once a pore is formed a single vesicle releases its contents very quickly. Regarding peptide aggregation, direct studies of the kinetics of this process are scarce, but it should be considered that membrane fluidity and the 2-D character of a lipid bilayer make the diffusion-limited encounter of two membrane-bound peptide molecules extremely fast [Rex and Schwarz, 1998]. Also the increase in population vesicle leakage with vesicle size has been previously observed [Parente *et al.*, 1990], and peptide exchange among vesicles was demonstrated in several cases [e.g. Grant *et al.*, 1992; Rex and Schwarz, 1998], including PMAP-23. Therefore, fluctuations induced by peptide exchange among vesicles might indeed be the rate-limiting step for vesicle leakage in many cases. More importantly, in all cases in which peptides do exchange among vesicles, the effects of fluctuations and of the discrete nature of the experimental system must be taken into account, even though the actual situation might be more complex than suggested by

the present model. However, fluctuations become insignificant when the number of peptides bound per vesicle is rather high, as suggested by the “carpet” model [Shai, 2002], and for this reason the present model might not be relevant for peptides acting according to this mechanism, such as PMAP-23. Indeed, Equation E4.11 does not provide an adequate fit to the leakage curves observed for this peptide.

Chapter 5

BIBLIOGRAPHY

Abrams, F. S. and E. London (1993).
Extension of the parallax analysis of membrane penetration depth to the polar region of model membranes: use of fluorescence quenching by a spin-label attached to the phospholipid polar headgroup.
Biochemistry 32: 10826–10831.

Allende, D., S. A. Simon and T. McIntosh (2005).
Melittin-induced bilayer leakage depends on lipid material properties: evidence for toroidal pores.
Biophys. J. 88: 1828-1837.

Andersson, A., J. Danielsson, A. Gräslund, L. Mäler (2007).
Kinetic models for peptide-induced leakage from vesicles and cells.
Eur. Biophys. J. 36: 621-635.

Arbuzova, A. and G. Schwarz (1999).
Pore-forming action of mastoparan peptides on liposomes: a quantitative analysis.
Biochim. Biophys. Acta, 1420: 139-152

Auvin-Guette, C., S. Rebufatt, Y. Prigent and B. Bodo (1992).
Trichogin GA IV, an 11-residue lipopeptaibol from Trichoderma longibrachiatum.
J. Am. Chem. Soc. 114: 2170-2174.

Barret, D. A., M. S. Hartshorne, M. A. Hussain, P. N. Shaw and M. C. Davies (2001).
Resistance to non specific protein adsorption by poly(vinyl alcohol) thin films adsorbed to a poly(styrene) support matrix studied using surface plasmon resonance.
Anal. Chem. 73: 5232-5239.

Barzel, B. and O. Biham (2009).
Stochastic analysis of dimerization systems.
Phys. Rev. E 80, 031117.

Belmonte, G., L. Cescatti, B- Ferrari, T. Nicolussi, M. Ropele, G. Menestrina (1987).
Pore formation by Staphylococcus aureus alpha-toxin in lipid bilayers.
Eur. Biophys. J. 14: 349-358.

Benachir, T. nadM. Lafleur (1995).
Study of vesicle leakage induced by melittin.
Biochim. Biophys. Acta 1235: 452-460.

Benedetti, E., A. Bavoso, B. Di Blasio, V. Pavone, C. Pedone, C. Toniolo, G. M. Bonora (1982).
Peptaibol antibiotics: a study on the helical structure of the 2-9 sequence of emerimicins III and IV.
Proc. Natl. Acad. Sci. U.S.A. 79: 7951-7954.

Blondelle S. E., Lohner, K. and M. Aguilar (1999).
Lipid-induced conformation and lipid-binding properties of cytolytic and antimicrobial peptides: determination and biological specificity.
Biochim. Biophys. Acta 1462: 89-108.

Bocchinfuso, G., A. Palleschi, B. Orioni, G. Grande, F. Formaggio, C. Toniolo, Y. Park, K.S. Hahm and L. Stella (2009).
Different mechanisms of action of antimicrobial peptides: insights from fluorescence spectroscopy experiments and molecular dynamics simulations.
J. Pept. Sci. 15: 550-558.

Boheim, G., W. Hanke and H Eibl (1980).
Lipid phase transition in planar bilayer membrane and its effect on carrier- and pore-mediated ion transport.
Proc. Natl. Acad. Sci. USA 77: 3403-3407.

Cao, Y., D. C. Samuels (2009).
Discrete stochastic simulation methods for chemically reacting systems.
Meth. Enzymol. 454: 115-140

Carpenter, T., P.J. Bond, S. Khalid, M.S.P. Sansom (2008).
Self-assembly of a simple membrane protein: coarse grained molecular dynamics simulations of the influenza M2 channel.
Biophys. J. 95: 3790–3801.

Chan, D. I., E. J. Prenner, H. J. Vogel (2006).
Tryptophan- and arginine-rich antimicrobial peptides: Structures and mechanisms of action.
Biochimica et Biophysica Acta 1758: 1184–1202.

Chattopadhyay, A., E. London (1987).
Parallax method for direct measurement of membrane penetration depth utilizing fluorescence quenching by spin-labeled phospholipids.
Biochemistry 26: 39–45.

Chen, R. F., J. R. Knutson (1988).
Mechanism of fluorescence concentration quenching of carboxyfluorescein in liposomes: energy transfer to nonfluorescent dimers.
Anal. Biochem. 172: 61-77.

Chung, L. A., J. D. Lear and W. F. DeGrado (1992).
Fluorescence studies of the secondary structure and orientation of a model ion channel peptide in phospholipid vesicles.
Biochemistry. 31(28): 6608-6616.

Chugh, J. K. and B. A. Wallace (2001).
Peptaibols: models for ion channels.
Biochem. Soc. Trans. 29: 565-571.

DeGrado, W. F., G. F. Musso, M. Lieber, E. T. Kaiser, F. J. Kezdy (1982).
Kinetics and mechanism of hemolysis induced by melittin and by a synthetic melittin analogue.
Biophys. J. 37: 329-338.

de Foresta, B., L. Tortech, M. Vincent, J. Gallay (2002).
Location and dynamics of tryptophan in transmembrane a-helix peptides: a fluorescence and circular dichroism study.
Eur. Biophys. J. 31: 185–197.

de Planque, M.R.R., D.V. Greathouse, Koeppe II R. E., H. Schäfer, D. Marsh, J.A. Killian (1998).
Influence of Lipid/Peptide Hydrophobic Mismatch on the Thickness of Diacylphosphatidylcholine Bilayers. A 2H NMR and ESR Study Using Designed Transmembrane Alpha-Helical Peptides and Gramicidin A.
Biochemistry 37: 9333–9345.

de Vries, A.H., A.E. Mark, S.J. Marrink (2004).
Molecular dynamics simulation of the spontaneous formation of a small dppc vesicle in water in atomistic detail.
J. Am. Chem. Soc. 126: 4488–4489.

Didoné, M. (2001).
Trichogin analogs for photophysical studies in membranes.
Chemistry MSc thesis. University of Padua, Padua, Italy.

Duque, D., X.J. Li, K. Katsov and M.J. Schick (2002).
Molecular theory of hydrophobic mismatch between lipids and peptides.
J. Chem. Phys. 116: 10478-10484.

Egberts, E., S.J. Marrink, H.J. Berendsen (1994).
Molecular dynamics simulation of a phospholipid membrane.
Eur. Biophys. J. 22: 423–436.

Epand, R. F., R. M. Epand, V. Monaco, S. Stoia, F. Formaggio, M. Crisma and C. Toniolo (1999).
The antimicrobial peptide trichogin and its interaction with phospholipid membranes.
Eur. J. Biochem. 266: 1021-1028.

Epand, R. M. and H. J. Vogel (1999).
Diversity of antimicrobial peptides and their mechanisms of action.
Biochim. Biophys. Acta 1462:11-28.

Epand, R. F., R. M. Epand, F. Formaggio, M. Crisma, H. Wu, R. I. Lehrer and C. Toniolo (2001).
Analogs of the antimicrobial peptide trichogin having opposite membrane properties.
Eur. J. Biochem. 268: 703-712.

Esquembre, R., J. A.Poveda and C. R. Mateo (2009).
Biophysical and Functional Characterization of an Ion Channel Peptide Confined in a Sol-Gel Matrix.
J. Phys. Chem. B 113: 7534-7540.

Esteban-Martín, S., J. Salgado (2007).
Self-assembling of peptide/membrane complexes by atomistic molecular dynamics simulations.
Biophys. J. 92: 903–912.

Estes, D. J., M. Mayer (2005).
Electroformation of giant liposomes from spin-coated films of lipids.
Colloids and Surfaces B: Biointerfaces 42: 115–123.

Fattal, E., S. Nir, R. A. Parente and F. Szoka Jr (1994).
Pore-forming peptide induce rapid phospholipid flip-flop in membranes.
Biochemistry 33: 6721-6731.

Förster, T. (1948).
Intermolecular energy migration and fluorescence.
Ann Phys 2: 55–75.

Gatto, E., C. Mazzuca, L. Stella, M. Venanzi, C. Toniolo, B. Pispisa (2006).
Effect of peptide lipidation on membrane perturbing activity: a comparative study on two trichogin analogues.
J. Phys Chem. B. 110: 22813-22818.

Gazit, E., A. Boman, H. G. Boman and Y. Shai (1995).
Interaction of the mammalian antibacterial peptide cecropin P1 with phospholipid vesicles.
Biochemistry 34: 11479-11488.

Gazit, E., I. R. Miller, P. C. Biggin, M. S. Sansom, Y. Shai (1996).
Structure and orientation of the mammalian antibacterial peptide cecropin P1 within phospholipid membranes.
J.Mol. Biol. 258: 860–870.

Glukhov, E., M. Stark, L. L. Burrows, C. M. Deber (2005).
Basis for selectivity of cationic antimicrobial peptides for bacterial versus mammalian membranes.
J. Biol. Chem. 280: 33960–33967.

Goutsias, J. (2007).
Classical versus stochastic kinetics modeling of biochemical reaction systems.
Biophys. J. 92: 2350–2365.

Grant, E., T. J. Beeler, K. M. P. Taylor, K. Gable, M. A. Roseman (1992).
Mechanism of magainin 2a induced permeabilization of phospholipid vesicles.
Biochemistry 31: 9912-9918.

Gregory, S. M., A. Cavenaugh, V. Journigan, A. Pokorny, P. F. F. Almeida (2008).
A quantitative model for the all-or-none permeabilization of phospholipid vesicles by the antimicrobial peptide cecropin A.
Biophys. J. 94: 1667-1680.

Gregory, S. M., A. Pokorny, P. F. F. Almeida (2009).
Magainin 2 revisited: a test for the quantitative model for the all-or-none permeabilization of phospholipid vesicles. Biophys. J. 96: 116-131.

Henzler Wildman, K. A., D.K. Lee, A. Ramamoorthy (2003).
Mechanism of lipid bilayer disruption by the human antimicrobial peptide, LL-37.
Biochemistry 42: 6545–6558.

Henzler Wildman, K. A., G.V. Martinez, M.F. Brown, A. Ramamoorthy (2004).
Perturbation of the hydrophobic core of lipid bilayers by the human antimicrobial peptide LL-37.
Biochemistry 43: 8459–8469.

Huang, H. W. (2000).
Action of antimicrobial peptides: two-state model.
Biochemistry 39: 8347-8352.

Humphrey, W., A. Dalke, K. Shulten (1996).
VMD-visual molecular dynamics.
J. Mol. Graph. 14: 33–38.

Kandasamy, S.K., R.G. Larson (2006).
Molecular dynamics simulations of model trans-membrane peptides in lipid bilayers: A systematic investigation of hydrophobic mismatch.
Biophys. J. 90: 2326–2343.

Kang, J. H., S. Y. Shin, S. Y. Jang, K. L. Kim and K.-S. Hahm (1999).
Effects of Tryptophan Residues of Porcine Myeloid Antibacterial Peptide PMAP-23 on Antibiotic Activity.
Biochem. Biophys. Res. Comm. 264: 281–286.

Kanellis, P., A. Y. Romans, B. J. Johnson, H. Kercret, R. Chiovetti, T. M. Allen, J. P. Segrest (1980).
Studies of synthetic peptide analogs of the amphipathic helix.
J. Biol. Chem. 255: 11464-11472.

Karle, I. and P. Balaram (1990).
Structural characteristics of α-helical peptide molecules containing Aib residues.
Biochemistry 29: 6747-6755.

Kolasińka, M. and P. Warszyński (2005).
The effect of support material and conditioning on wettability of PAH/PSS multilayer films.
Bioelectrochemistry 66: 65-70.

Johnson, A. E. (2005).
Fluorescence approaches for determining protein conformations, interactions and mechanisms at membranes.
Traffic 6: 1078–1092.

Juvvadi, P., S. Vunnam and R.B. Merrifield (1996).
Synthetic mellitin, its enantio, retro, and retroenantio isomers, and selected chimeric analogs: their antibacterial, hemolytic and lipid bilayer action.
J. Am. Chem. Soc. 118: 8989-8997.

Lacapère, J.J., E. Pebay-Peyroula, J.M. Neumann, C. Etchebest (2007).
Determining membrane protein structures: still a challenge!
Trends Biochem. Sci. 32: 259–270.

Ladokhin, A. S., W. C. Wimley, K. Hristova, S. H. White (1997).
Mechanism of leakage contents of membrane vesicles determined by fluorescence requenching.
Meth. Enzymol. 278: 474-486.

Ladokhin, A. S. (1997).
Distribution analysis of depth-dependent fluorescence quenching in membranes: a practical guide.
Meth. Enzymol. 278: 462-473.

Ladokhin, A.S. (1999a).
Analysis of protein and peptide penetration into membranes by depth-dependent fluorescence quenching: theoretical considerations.
Biophys. J. 76: 946–955.

Ladokhin, A. S. (1999b).
Evaluation of lipid exposure of tryptophan residues in membrane peptides and proteins.
Anal. Biochem. 276: 65–71.

Lakowicz, J. R. (2006a).
Principles of fluorescence spectroscopy.
3rd ed. Cap. I, Plenum Press, New York.

Lakowicz, J. R. (2006b).
Principles of fluorescence spectroscopy.
3rd ed. Cap. IV, Plenum Press, New York.

Lakowicz, J. R. (2006c).
Principles of fluorescence spectroscopy.
3rd ed. Cap. VI, Plenum Press, New York.

Lakowicz, J. R. (2006d).
Principles of fluorescence spectroscopy.
3rd ed. Cap. VIII, Plenum Press, New York.

Lakowicz, J. R. (2006e).
Principles of fluorescence spectroscopy.
3rd ed. Cap. X, Plenum Press, New York.

Lakowicz, J. R. (2006f).
Principles of fluorescence spectroscopy.
3rd ed. Cap. XIII, Plenum Press, New York.

Leontiadou, H., A.E. Mark, S.J. Marrink (2006).
Antimicrobial peptides in action.
J. Am. Chem. Soc. 128: 12156–12161.

Lis, L. J., M. McAlister, N. L. Fuller, R. P. Rand, V. A. Parsegian (1982).
Measurement of the lateral compressibility of several phospholipid bilayers.
Biophys. J. 37: 667–672.

Locardi, E., S. Mammi, C. Peggion, V. Monaco, F. Formaggio, M. Crisma, C. Toniolo, B. Bodo, S. Rebuffat, J. Kamphuis and Q. B. Broxterman (1998).
Conformation and membrane activity of an analogue of the peptaibol antibiotic trichogin GA IV with a lipophilic amino acid at the N-terminus.
J. Pep. Sci. 4: 389-399.

Lohner, K. and E. J. Prenner (1999).
Differential scanning calorimetry and X-ray diffraction studies of the specificity of the interaction of antimicrobial peptides with membrane-mimetic systems.
Biochim. Biophys. Acta 1462: 141-156.

Loura, L. M. S., R. F. M. de Almeida, A. Coutinho, M. Prieto (2003).
Interaction of peptides with binary phospholipid membranes: application of fluorescence methodologies.
Chem. Phys. Lipids 122: 77-96.

Ludtke, H. K. and H. W. Huang (1996).
Mechanism of alamethicin insertion into lipid bilayers.
Biophys. J. 71: 2669-2679.

Ludtke, S. J., K. He, W.T. Heller, T.A. Harroun, L. Yang, H.W. Huang (1997).
Membrane pores induced by magainin.
Biochemistry 35: 13723–13728.

Marrink, S.J., E. Lindhal, O. Edholm, A.E. Mark (2001).
Simulation of the spontaneous aggregation of phospholipids into bilayers.
J. Am. Chem. Soc. 123: 8638–8639.

Matsuzaki, K., O. Murase, H. Tokuda, S. Funakoshi, N. Fujii, K. Miyajima (1994).
Orientational and aggregational states of magainin2 in phospholipid bilayers.
Biochemistry. 33: 3342–3349.

Matsuzaki, K., O. Murase, N. Fujii and K. Miyajima (1995a).
Translocation of a Channel-Forming Antimicrobial Peptide, Magainin 2, across Lipid Bilayers by Forming a Pore.
Biochemistry 34: 6521-6526.

Matsuzaki, K., O. Murase, K. Miyajima (1995b).
Kinetics of pore formation by an antimicrobial peptide, magainin 2, in phospholipid bilayers.
Biochemistry 34:12553-12559.

Matsuzaki, K., O. Murase, N. Fujii, K. Miyajima (1996).
An antimicrobial peptide, magainin 2, induced rapid flip-flop of phospholipids coupled with pore formation and peptide translocation.
Biochemistry 35: 11361–11368.

Matsuzaki, K. (1998).
Magainin as paradigm for the mode of action of pore forming polypeptides.
Biochim. Biophys. Acta 1376: 391-400.

Matsuzaki, K. (1999).
Why and how are peptide-lipid interactions utilized for self-defense? Magainins and tachyplesins as archetypes.
Biochim. Biophys. Acta 1462: 1-10.

Matsuzaki, K. (2001).
Molecular mechanisms of membrane perturbation by antimicrobial peptides.
In Development of Novel Antimicrobial Agents: Emerging Strategies. K. Lohner, editor. Horizon Scientific Press, Wymondham. 167-181.

Matyus, E., C. Kandt, D.P. Tieleman (2007).
Computer simulation of antimicrobial peptides.
Curr. Med. Chem. 14: 2789–2798.

Mazeres, S., V. Schram, J. F. Tocanne, A. Lopez (1996).
7-Nitrobenz-2-oxa-1,3-diazole-4-yl-labeled phospholipids in lipid membranes: differences in fluorescence behavior.
Biophys. J. 71: 327–335.

Mazzuca, C. (2005).
Mechanism of membrane perturbation by the antimicrobial peptide trichogin GA IV: a physico-chemical study on fluorescent analogs.
Chemistry Ph.D. thesis. University of Rome "Tor Vergata", Rome, Italy.

Mazzuca, C., L. Stella, M. Venanzi, F. Formaggio, C. Toniolo, B. Pispisa (2005).
Mechanism of membrane activity of the antibiotic trichogin GA IV: a two-state transition controlled by peptide concentration.
Biophys. J. 88: 3411–3421.

McIntyre, J. C., R. G. Sleight (1991).
Fluorescence assay for phospholipid membrane asymmetry.
Biochemistry 30: 11819–11827.

Merrifield, R.B. (1986).
Solid-phase synthesis.
Science 232: 341–347.

Monaco, V., E. Locardi, F. Formaggio, M. Crisma, S. Mammi, E. Peggion, C. Toniolo, S. Rebuffat and B. Bodo (1998).
Solution conformational analysis of amphiphilic helical, synthetic analogs of the lipopeptaibol trichogin GA IV.
J. Pep. Res. 52: 261-272.

New, R. R. C. R. (1990).
Structure of liposomes.
In Liposomes: a Practical Approach. 1-32. R. R.C. New, editor. Oxford University Press, Oxford.

Oren, Z. and Y. Shai (1998).
Mode of action of linear amphipathic alpha-helical antimicrobial peptides. Biopolymers 47: 451-463.

Orioni, B., G. Bocchinfuso, J. Y. Kim, A. Palleschi, G. Grande, S. Bobone, M. Venanzi, Y. Park, J. I. Kim, K. S. Hahm and L. Stella (2009).
Membrane perturbation by the antimicrobial peptide PMAP-23: a fluorescence and molecular dynamics study.
Biochim Biophys Acta. 1788(7):1523-1533.

Ostolaza, H., B. Bartolomé, I. O de Zárate, F. de la Cruz, F. M. Goñi (1993).
Release of lipid vesicle contents by the bacterial protein toxin α-hemolysin.
Biochim. Biophys. Acta, 1147: 81-88.

Parasassi, T., G. De Stasio, G. Ravagnan, R. M. Rusch and E. Gratton (1991).
Quantitation of lipid phases in phospholipid vesicles by the generalized polarization of Laurdan fluorescence.
Biophys. J. 60: 179-189.

Papo, N. and Y. Shai (2003).
Exploring peptide-membrane interaction using surface plasmon resonance: differentiation between pore formation versus membrane disruption by lytic peptide.
Biochemistry 42: 458-466.

Parente, R. A., S. Nir, F. C. Szoka (1990).
Mechanism of leakage of phospholipid vesicle contents induced by the peptide GALA.
Biochemistry 29: 8720-8728.

Park, K., D. Oh, S.Y. Shin, K.S. Hahm, Y. Kim (2002).
Structural studies of porcine myeloid antibacterial peptide PMAP-23 and its analogues in DPC micelles by NMR spectroscopy.
Biochem. Biophys. Res. Comm. 290: 204–212.

Penfold, J. R. M. Richardson, A. Zarbakhsh, J. R. P. Webster, D. G. Bucknall, A. R. Rennie, R. A. L. Jones, T. Cosgrove, R. K. Thomas, J. S. Higgins, P. D. I. Fletcher, E. Dickinson, S. J. Roser, I. A. McLure, A. R. Hillman, R. W. Richards, E. J. Staples, A. N. Burgess, E. A. Simister and J. W. White (1997).
Recent advances in the study of chemical surfaces and interfaces by specular neutron reflection.
J. Chem. Soc., Faraday Trans. 93: 3899-3917.

Persson, D., P. E. G. Thorén, M. Herner, P. Lincoln and B. Nordén (2003).
Application of a Novel Analysis To Measure the Binding of the Membrane-Translocating Peptide Penetratin to Negatively Charged Liposomes.
Biochemistry 42: 421-429.

Pispisa, B., L. Stella, M. Venanzi, A. Palleschi, F. Marchiori, A. Polese and C. Toniolo (2000a).
A spectroscopic and molecular mechanics investigation on a series of Aib-based linear peptides and a peptide template, both containing tryptophan and a nitroxide derivatives as probe.
Biopolymers 53: 169-181.

Pispisa, B., L. Stella, M. Venanzi, A. Palleschi, C. Vippiani, A. Polese, F. Formaggio and C. Toniolo (2000b).
Quenching mechanism in bichromophoric, 3_{10}-helical Aib-based peptides, modulated by chain-length dependent topologies.
Macromolecules 33: 906-915.

Pokorny, A., T. H. Birkbeck, P. F. F. Almeida (2002).
Mechanism and kinetics of δ-lysin interaction with phospholipid vesicles.
Biochemistry 41: 11044–11056.

Pokorny, A., P. F. F. Almeida (2004).
Kinetics of dye efflux and lipid flip-flop induced by δ-lysin in phosphatidylcholine vesicles and the mechanism of graded release by amphipathic, α-helical peptides.
Biochemistry 43: 8846-8857.

Portlock, S. H., M. J. Clague, R. J. Cherry (1990).
Leakage of internal markers from erythrocytes and lipid vesicles induced by melittin, gramicidin S and alamethicin: a comparative study.
Biochim. Biophys. Acta 1030: 1-10.

Pouny, Y. and Y. Shai (1992).
*Interaction of D-amino acid incorporated analogs of pardaxin with membrane*s.
Biochemistry 31: 9482-9490.

Rapaport, D., R. Peled, S. Nir, Y. Shai (1996).
Reversible surface aggregation in pore formation by pardaxin.
Biophys. J. 70: 2502-2512.

Rathinakumar, R. and W. C. White (2008).
Biomolecular engineering by combinatorial design and high throughput screening: small soluble peptides that permeabilize membranes.
J. Am. Chem. Soc. 130: 9849-9858.

Rex, S. and G. Schwarz (1998).
Quantitative studies on the melittin-induced leakage mechanism of lipid vesicles.
Biochemistry, 37: 2336-2345.

Rizzo, V., S. Stankowski and G. Schwarz (1987).
Alamethicin incorporation in lipid bilayers: a thermodynamic study.
Biochemistry 26: 2751-2759.

Roeske, R. W. and S. J. Kennedy (1983).
Chemistry and biochemistry of amino acids, peptide and proteins.
In Weinsten, B. Ed.Dekker, New York. 7: 205-265.

Saberwal, G., R. Nagaraj (1993).
Interaction of hydrophobic peptides with model membranes: slow binding to membranes and not subtle variations in pore structure is responsible for the gradual release of entrapped solutes.
Biochim. Biophys. Acta 1151: 43-50.

Schwarz, G., H. Gerke, V. Rizzo and S. Stankowki (1987).
Incorporation kinetics in a membrane, studied with the pore-forming peptide Alamethicin.
Biophys. J. 52: 685-692.

Schwarz, G. and G. Beschiaschvili (1989).
Thermodynamic and kinetic studies on the association of melittin with a phospholipid bilayer.
Biochim. Biophys. Acta 979: 82-90.

Schwarz, G. and C. H. Robert (1990).
Pore formation kinetics in membranes, determined from the release of marker molecules out of liposomes or cells.
Biophys. J. 58: 577-583.

Schwarz, G., R. Zong and T. Popescu (1992).
Kinetics of melittin induced pore formation in the membrane of lipid vesicles.
Biochim. Biophys. Acta 1110: 97-104.

Schwarz, G. and A. Arbuzova (1995).
Pore kinetics reflected in the dequenching of a lipid vesicle entrapped fluorescent dye.
Biochim. Biophys. Acta 1239: 51-57.

Schwarz, G. and S. E. Taylor (1999).
Polymorphism and interaction of a Viral Fusion Peptide in a compressed lipid monolayer.
Biophys. J. 76: 3167-3175.

Shai, Y. (1999).
Mechanism of the binding, insertion and destabilization of phospholipid bilayer membranes by alpha-helical antimicrobial and cell non-selective membrane-lytic peptides.
Biochim. Biophys. Acta 1462: 55-70.

Shai, Y. (2002).
Mode of action of membrane active antimicrobial peptides.
Biopolymers 66: 236-248.

Shnerb, N. M., Y. Louzoun, E. Bettelheim, S. Solomon (2000).
The importance of being discrete: Life always wins on the surface.
Proc. Natl. Acad. Sci. U.S.A., 97: 10322–10324.

Sitaram, N. and R. Nagaraj (1999).
Interaction of antimicrobial peptides with biological activity and model membranes: structural and charge requirements for activity.
Biochim. Biophys. Acta 1462: 29-54.

Spach, G., H. Duchlohier, G. Molle and G. M. Vallethon (1989).
Structure and supramolecular architecture of membrane channel forming peptide.
Biochemie 71: 11-21.

Stella, L., C. Mazzuca, M. Venanzi, A. Palleschi, M. Didone', F. Formaggio, C. Toniolo and B. Pispisa (2004).
Aggregation and water-membrane partition as major determinants of the activity of the antibiotic peptide Trichogin GA IV.
Biophys. J. 86: 936-945.

Stella, L., M. Burattini, C. Mazzuca, A. Palleschi, M. Venanzi, C. Baldini, F. Formaggio, C. Toniolo, B. Pispisa (2007).
Alamethicin interaction with lipid membranes: a spectroscopic study on synthetic analogues.
Chem. Biodivers. 4: 1299–1312.

Stella, L., M. Venanzi, K.S. Hahm, F. Formaggio, C. Toniolo, B. Pispisa (2008).
Shining a light on peptide-lipid interactions: fluorescence methods in the study of membrane active peptides.
Chem. Today 26: 44–46.

Stewart, J. C. M. (1980).
Colorimetric determination of phospholipids with ammonium ferrothiocyanate.
Anal. Biochem. 104: 10-14.

Tieleman, D. P., M.S.P. Sansom, H.J.C. Berendsen (1999).
Alamethicin helices in a bilayer and in solution: molecular dynamics simulations.
Biophys. J. 76: 40–49.

Toniolo, C., C. Peggion, M. Crisma, F. Formaggio, X. Shui and D. S. Eggleston (1994).
Structure determination of racemic trichogin GA IV using centrosymmetric crystals.
Nature Struct. Biol. 1: 908-914.

Toniolo, C., M. Crisma, F. Formaggio, C. Peggion, V. Monaco, C. Goulard, S. Rebuffat and B. Bodo (1996).
Effect of Nα-acyl chain length on the membrane-modifying properties of synthetic analogs of the lipopeptaibol trichogin GA IV.
J. Am. Chem. Soc. 118: 4952-4958.

Toniolo, C., M. Crisma, F. Formaggio, C. Peggion, R. F. Epand and R. M. Epand (2001).
Lipopeptaibols, a novel family of membrane active, antimicrobial peptides.
Cell. Mol. Life Sci. 58: 1179-1188.

Vacklin, H. P., F. Tiberg, R. K. Thomas (2005).
Formation of supported phospholipid bilayers via co-adsorption with β-D-dodecyl maltoside.
Biochimica et Biophysica Acta 1668: 17–24.

van der Spoel, D., E. Lindahl, B. Hess, G. Groenhof, A. E. Mark, H. J. C. Berendsen (2005).
GROMACS: fast, flexible and free.
J. Comp. Chem. 26: 1701–1718.

Voges, K. P., G. Jung, W. H. Sawyer (1987).
Depth-dependent fluorescent quenching of a tryptophan residue located at defined positions on a rigid 21-peptide helix in liposomes.
Biochim. Biophys. Acta 896: 64-76.

Wee, C.L., D. Gavaghan, M.S.P. Sansom (2008).
Lipid bilayer deformation and the free energy of interaction of a Kv channel gating-modifier toxin.
Biophys. J. 95: 3816–3826.

Weinstein, J. N., R. D. Klausner, T. Innerarity, E. Ralston, R. Blumenthal (1981).
Phase transition release, a new approach to the interaction of proteins with lipid vesicles.
Biochim. Biophys. Acta 647: 270-284.

White, S. H., Wimley, W. C. (1999).
Membrane protein folding and stability: physical principles.
Ann. Rev. Biophys. Biomol. Struct. 28: 319-65.

White, S. H., W. C. Wimley, A. S. Ladokin and K. Hristova (1998).
Protein folding in membranes: determining energetics of peptide-bilayer interactions.
Methods Enzymol. 295: 62-87.

Wolf, D. E., A. P. Winiski, A. E. Ting, K. M. Bocian and R. E. Pagano (1982).
Determination of the transbilayer distribution of fluorescent lipid analogues by nonradiative fluorescence resonance energy transfer.
Biochemistry 31: 2865–2873.

Yandek, L. E., A. Pokorny, P. F. F. Almeida (2009).
Wasp mastoparans follow the same mechanism as the cell-penetrating peptide transportan 10.
Biochemistry 48: 7342-7351.

Yang, L., T. A. Harroun, T. M. Weiss, L. Ding and H. W. Huang (2001).
Barrel stave or toroidal model? A case study on melittin pores.
Biophys. J. 81: 1475-1485.

Yang, S. T., J. H. Jeon, Y. Kim, S. Y. Shin, K. S. Hahm, J. I. Kim (2006).
Possible role of a PXXP central hinge in the antibacterial activity and membrane interaction of PMAP-23, a member of cathelicidin family.
Biochemistry 45: 1775-1784.

Zanetti, M., P. Storici, A. Tossi, M. Scocchi and R. Gennaro (1994).
Molecular cloning and chemical synthesis of a novel antimicrobial peptide derived from pig myeloid cells.
J. Biol. Chem. 269: 7855-7858.

Zasloff, M. (2002).
Antimicrobial peptides of multicellular organisms.
Nature 415: 389-395.

Zhao, H., R. Sood, A. Jutila, S. Bose, G. Fimland, J. Nissen-Meyer, P. K. J. Kinnunen (2006).
Interaction of the antimicrobial peptide pheromone Plantaricin A with model membranes: implications for a novel mechanism of action.
Biochim. Biophys. Acta 1758: 1461–1474.

APPENDIX

PUBLICATIONS AND COMMUNICATIONS

PUBLICATIONS

B. Orioni, G. Bocchinfuso, J. Y. Kim, A. Palleschi, G. Grande, S. Bobone, M. Venanzi, Y. Park, J. I. Kim, K. S. Hahm and L. Stella (2009).
Membrane perturbation by the antimicrobial peptide PMAP-23: a fluorescence and molecular dynamics study.
Biochim Biophys Acta. 1788(7):1523-1533.

G. Bocchinfuso, A. Palleschi, B. Orioni, G. Grande, F. Formaggio, C. Toniolo, Y. Park, K.S. Hahm and L. Stella (2009).
Different mechanisms of action of antimicrobial peptides: insights from fluorescence spectroscopy experiments and molecular dynamics simulations.
J. Pept. Sci. 15: 550-558.

E. Islas-Rodriguez, L. Marcellini, B. Orioni, D. Barra, L. Stella and M. L. Mangoni (2009).
Esculentin 1-21: a linear antimicrobial peptide from frog skin with inhibitory effect on bovine mastitis-causing bacteria.
J. Pept. Sci. 15: 607-614.

C.Baldini, F. Formaggio, C. Toniolo, A. Toffoletti, C. Corvaja, J. P. Mazaleyrat, K. Wright, J. F. Lohier, M. Wakselman, B. Orioni, L. Stella, M. Venanzi (2009).
Incorporation of a novel, fluorescent and helicogenic α-amino acid into peptaibols: trichogin GA IV.
Adv.. Exp. Med. Biol. 611: 287.

R. Fabrini, A. De Luca, L. Stella, G. Mei, B. Orioni, S. Ciccone, G. Federici, M. Lo Bello and G. Ricci (2009).
Monomer/dimer equilibrium in glutathione transferases: a critical re-examination.
Biochemistry 48: 10473-10482.

L. Stella, G. Bocchinfuso, G. Grande, B. Orioni, M. Venanzi, J.Y. Kim, Y. Park, K.S. Hahm, M. De Zotti, F. Formaggio, C. Toniolo, A. Palleschi.
Determining the location of antimicrobial peptides inside lipid bilayers by combined fluorescence spectroscopy and molecular dynamics simulations.
in "Peptides 2008", EPS, in press.

C. Mazzuca, B. Orioni, F. Formaggio, C. Toniolo, M. Coletta, G. Maulucci,, M. De Spirito, B. Pispisa, M. Venanzi and L. Stella.
Fluctuations and the rate limiting step of peptide-induced membrane leakage.
Submitted.

COMMUNICATIONS

Determination of peptide location inside a lipid bilayer by combined fluorescence spectroscopy and molecular dynamics simulations. The case of the antimicrobial peptide PMAP-23.
Oral presentation in Acta Biophysica Romana (Rome, Italy), 10-11/04/2008

Incorporation of a novel, fluorescent and helicogenic a-amino acid into peptaboils: trichogin GA IV. Convegno Nazionale Chimica dei Sistemi Biologici della S.C.I., Montagnana (Padua, Italy), 8-9/11/2007.

Localization of the antimicrobial peptide PMAP-23 in phospholipid membranes. A combined spectroscopic and molecular dynamics study. Nazionale Chimica dei Sistemi Biologici della S.C.I., Montagnana (Padua, Italy), 8-9/11/2007.

Localization of the antimicrobial peptide PMAP-23 in phospholipid membranes. A combined spectroscopic and molecular dynamics study. Convegno Nazionale Chimica Fisica della S.C.I., Camogli (Genoa, Italy), 24-29/02/2008.

Membrane perturbing activity of a new analogue of the cell penetrating peptide Pep-1. Acta Biophysica Romana (Rome, Italy), 10-11/04/2008.

Effect of helix kink on the activity and selectivity of an antimicrobial peptide. 11th Naples Workshop on Bioactive Peptides (Naples, Italy), 24-27/05/2008.

Switching Peptide Bioactivity from Cell-penetrating to Antimicrobial : The Case of Pep-1 and Pep-1-K. 11th Naples Workshop on Bioactive Peptides (Naples, Italy), 24-27/05/2008.

Location of the antimicrobial peptide PMAP-23 inside lipid bilayer. Implications for the mechanism of action. 1st Italy-Korea Symposium on Antimicrobial Peptides. Chosun University (Gwangju, Korea), 24-25/07/2008.

Membrane perturbing activity of a new analogue of the cell penetrating peptide Pep-1. 1st Italy-Korea Symposium on Antimicrobial Peptides. Chosun University (Gwangju, Korea), 24-25/07/2008.

Effect of helix kink on the activity and selectivity of an antimicrobial peptide. 1st Italy-Korea Symposium on Antimicrobial Peptides. Chosun University (Gwangju, Korea), 24-25/07/2008.

A hypothesis on the kinetic behavior of peptide-induced membrane leakage. 1st Italy-Korea Symposium on Antimicrobial Peptides. Chosun University (Gwangju, Korea), 24-25/07/2008..

Determining the Location of Antimicrobial Peptides Inside Lipid Bilayers by Combined Fluorescence Spectroscopy and Molecular Dynamics Simulations. 30th European Peptide Symposium. (Helsinki, Finland), 31/05-05/09 2008.

Mechanism of action of the antimicrobial peptide PMAP-23: a spectroscopic study on synthetic analogues. XXIII Congresso Nazionale della Societa' Chimica Italiana, Sorrento (Naples, Italy), 5-10/07/2009.

Effect of helix kink on the activity and selectivity of an antimicrobial peptide. 7th European Biophysics Congress, organised by the European Biophysical Societies Association, Genova (Italy), 11-15/07/2009.

Different action mechanisms of antimicrobial peptides: fluorescence experiments and MD simulations. 7th European Biophysics Congress, organised by the European Biophysical Societies Association, Genova (Italy), 11-15/07/2009.

TABLE OF CONTENTS